INL/EXT-13-29930 Rev. 3

September 2016

BISON Theory Manual
The Equations Behind Nuclear Fuel Analysis
BISON Release 1.3

J. D. Hales
R. L. Williamson
S. R. Novascone
G. Pastore
B. W. Spencer
D. S. Stafford
K. A. Gamble
D. M. Perez
R. J. Gardner
W. Liu
J. Galloway
C. Matthews
C. Unal
N. Carlson

INL/EXT-13-29930 Rev. 3

BISON Theory Manual
The Equations Behind Nuclear Fuel Analysis

J. D. Hales
R. L. Williamson
S. R. Novascone
G. Pastore
B. W. Spencer
D. S. Stafford
K. A. Gamble
D. M. Perez
R. J. Gardner
W. Liu
J. Galloway
C. Matthews
C. Unal
N. Carlson

September 2016

Idaho National Laboratory
Fuel Modeling and Simulation Department
Idaho Falls, Idaho 83415

Prepared for the
U.S. Department of Energy
Office of Nuclear Energy
Under U.S. Department of Energy-Idaho Operations Office
Contract DE-AC07-99ID13727

Contents

1 Introduction

BISON [1] is a finite element-based nuclear fuel performance code applicable to a variety of fuel forms including light water reactor fuel rods, TRISO particle fuel [2], and metallic rod [3] and plate fuel. It solves the fully-coupled equations of thermomechanics and species diffusion, for either 1D spherical, 2D axisymmetric or 3D geometries. Fuel models are included to describe temperature and burnup dependent thermal properties, fission product swelling, densification, thermal and irradiation creep, fracture, and fission gas production and release. Plasticity, irradiation growth, and thermal and irradiation creep models are implemented for clad materials. Models are also available to simulate gap heat transfer, mechanical contact, and the evolution of the gap/plenum pressure with plenum volume, gas temperature, and fission gas addition. BISON is based on the MOOSE framework [4] and can therefore efficiently solve problems using standard workstations or very large high-performance computers.

This document describes the theoretical and numerical foundations of BISON.

2 Governing Equations

The BISON governing relations consist of fully-coupled partial differential equations for energy, species, and momentum conservation. The energy balance is given in terms of the heat conduction equation

$$\rho C_p \frac{\partial T}{\partial t} + \nabla \cdot \mathbf{q} - e_f \dot{F} = 0, \tag{2.1}$$

where T, ρ and C_p are the temperature, density and specific heat, respectively, e_f is the energy released in a single fission event, and $\dot{F}$ is the volumetric fission rate. $\dot{F}$ can be prescribed as a function of time and space, or input from a separate neutronics calculation. The heat flux is given as

$$\mathbf{q} = -k\nabla T, \tag{2.2}$$

where k denotes the thermal conductivity of the material.

Species conservation is given by

$$\frac{\partial C}{\partial t} + \nabla \cdot \mathbf{J} + \lambda C - S = 0, \tag{2.3}$$

where C, λ, and S are the concentration, radioactive decay constant, and source rate of a given species, respectively. The mass flux $\mathbf{J}$ is specified as

$$\mathbf{J} = -D\nabla C, \tag{2.4}$$

where D is the diffusion coefficient; this definition has been used to simulate fission product transport within the fuel. Also implemented in BISON is a hyperstoichiometric model for oxygen diffusion in UO_2 fuel as described in [5]. In this case $\mathbf{J}$ denotes the oxygen flux in the hyperstoichiometric regime with,

$$\mathbf{J} = -D\left(\nabla C - \frac{CQ^*}{FRT^2}\nabla T\right), \tag{2.5}$$

where D is diffusivity, F is the thermodynamic factor of oxygen, Q^* is the heat of transport of oxygen, and R is the universal gas constant.

Momentum conservation is prescribed assuming static equilibrium at each time increment using Cauchy's equation,

$$\nabla \cdot \boldsymbol{\sigma} + \rho \mathbf{f} = 0, \tag{2.6}$$

where $\boldsymbol{\sigma}$ is the Cauchy stress tensor and $\mathbf{f}$ is the body force per unit mass (e.g. gravity). The displacement field u, which is the primary solution variable, is connected to the stress field via the strain, through a constitutive relation.

3 Element Kinematics

For geometrically linear analysis, the strain ε is defined as $1/2[\nabla \mathbf{u} + \nabla \mathbf{u}^T]$. Furthermore, with a linear elastic constitutive model, the stress is simply $C\,\varepsilon$. We now outline our approach for nonlinear analysis. We follow the approach in [6] and the software package [7].

We begin with a complete set of data for step n and seek the displacements and stresses at step $n+1$. We first compute an incremental deformation gradient,

$$\hat{\mathbf{F}} = \frac{\partial x^{n+1}}{\partial x^n}. \tag{3.1}$$

With $\hat{\mathbf{F}}$, we next compute a strain increment that represents the rotation-free deformation from the configuration at n to the configuration at $n+1$. Following [6], we seek the stretching rate $\mathbf{D}$:

$$\mathbf{D} = \frac{1}{\Delta t}\log(\hat{\mathbf{U}}) \tag{3.2}$$

$$= \frac{1}{\Delta t}\log\left(\text{sqrt}\left(\hat{\mathbf{F}}^T\hat{\mathbf{F}}\right)\right) \tag{3.3}$$

$$= \frac{1}{\Delta t}\log\left(\text{sqrt}\left(\hat{\mathbf{C}}\right)\right). \tag{3.4}$$

Here, $\hat{\mathbf{U}}$ is the incremental stretch tensor, and $\hat{\mathbf{C}}$ is the incremental Green deformation tensor. Through a Taylor series expansion, this can be determined in a straightforward, efficient manner. $\mathbf{D}$ is passed to the constitutive model as an input for computing σ at $n+1$.

The next step is computing the incremental rotation, $\hat{\mathbf{R}}$ where $\hat{\mathbf{F}} = \hat{\mathbf{R}}\hat{\mathbf{U}}$. Like for $\mathbf{D}$, an efficient algorithm exists for computing $\hat{\mathbf{R}}$. It is also possible to compute these quantities using an eigenvalue/eigenvector routine.

With σ and $\hat{\mathbf{R}}$, we rotate the stress to the current configuration.

4 Axisymmetric Equations

For the axisymmetric case (RZ), the nonlinear strains are derived starting from the Green-Lagrange strain:

$$E = \frac{1}{2}\left(F^T F - I\right) = \frac{1}{2}\left(\left(I + \frac{\partial u}{\partial X}\right)^T \left(I + \frac{\partial u}{\partial X}\right) - I\right) = \frac{1}{2}\left(\frac{\partial u}{\partial X} + \frac{\partial u}{\partial X}^T + \frac{\partial u}{\partial X}^T \frac{\partial u}{\partial X}\right) \tag{4.1}$$

This leads to:

$$\varepsilon_{rr} = \frac{\partial u_r}{\partial r} + \frac{1}{2}\left(\frac{\partial u_r}{\partial r}^2 + \frac{\partial u_z}{\partial r}^2\right) \tag{4.2}$$

$$\varepsilon_{zz} = \frac{\partial u_z}{\partial z} + \frac{1}{2}\left(\frac{\partial u_r}{\partial z}^2 + \frac{\partial u_z}{\partial z}^2\right) \tag{4.3}$$

$$\varepsilon_{\theta\theta} = \frac{u_r}{r} + \frac{1}{2}\left(\frac{u_r}{r}\right)^2 \tag{4.4}$$

$$\varepsilon_{rz} = \frac{1}{2}\left(\frac{\partial u_r}{\partial z} + \frac{\partial u_z}{\partial r} + \frac{\partial u_r}{\partial r}\frac{\partial u_r}{\partial z} + \frac{\partial u_z}{\partial r}\frac{\partial u_z}{\partial z}\right) \tag{4.5}$$

We can recover the linear strain by ignoring the higher-order terms.

5 Spherically Symmetric Equations

For the spherically symmetric case, the nonlinear strains are derived starting from the Green-Lagrange strain:

$$E = \frac{1}{2}\left(F^T F - I\right) = \frac{1}{2}\left(\left(I + \frac{\partial u}{\partial X}\right)^T \left(I + \frac{\partial u}{\partial X}\right) - I\right) = \frac{1}{2}\left(\frac{\partial u}{\partial X} + \frac{\partial u}{\partial X}^T + \frac{\partial u}{\partial X}^T \frac{\partial u}{\partial X}\right) \tag{5.1}$$

This leads to:

$$\varepsilon_{rr} = \frac{\partial u_r}{\partial r} + \frac{1}{2}\left(\frac{\partial u_r}{\partial r}^2\right) \tag{5.2}$$

$$\varepsilon_{\theta\theta} = \frac{u_r}{r} + \frac{1}{2}\left(\frac{u_r}{r}\right)^2 \tag{5.3}$$

$$\varepsilon_{\phi\phi} = \frac{u_r}{r} + \frac{1}{2}\left(\frac{u_r}{r}\right)^2 \tag{5.4}$$

We can recover the linear strain by ignoring the higher-order terms.

6 Elasticity

For elastic behavior, a hypoelastic formulation is used, specifically,

$$\sigma_{ij}^{n+1} = \sigma_{ij}^{n} + \Delta t \mathbf{C}_{ijkl} \mathbf{D}_{kl} \tag{6.1}$$

where $\mathbf{C}$ is the elasticity tensor. For isotropic elasticity, this becomes

$$\sigma_{ij}^{n+1} = \sigma_{ij}^{n} + \Delta t \left(\delta_{ij} \lambda \mathbf{D}_{kk} + 2\mu \mathbf{D}_{ij} \right) \tag{6.2}$$

with λ as Lame's first parameter and μ as the shear modulus. This stress update occurs in the configuration at n. Thus as a final step, the stress must be rotated to the configuration at $n+1$.

7 Nonlinear Materials

Fuel materials often exhibit nonlinear mechanical behavior. As a first step to modeling this behavior, von Mises linear isotropic strain hardening via an implicit radial return method was implemented in BISON. A summary of this implementation is described in the following steps.

1. An elastic trial stress is calculated using the previous stress state and a total strain increment

$$\sigma^{trial} = \sigma_{old} + \mathbf{C}\Delta\varepsilon \tag{7.1}$$

where $\mathbf{C}$ is the linear isotropic elasticity tensor, $\Delta\varepsilon$ is the total strain increment tensor, and $\sigma_{\mathbf{old}}$ is the stress from the previous time step.

2. A yield function is evaluated

$$f = \sigma_{eff}^{trial} - r - \sigma_{yield} \tag{7.2}$$

where f is the yield function, σ_{eff}^{trial} is the effective trial stress based on the deviatoric trial stress, r is the hardening variable, and σ_{yield} is the yield stress. If the yield function is greater than zero, then permanent deformation has occurred and a the plastic strain increment must be calculated. Otherwise, the trial stress is the new stress.

3. The hardening variable, r, and the plastic strain increment are solved via Newton iteration.

$$r = r_{old} + h\Delta p \tag{7.3}$$

$$residual = \frac{\sigma_{effective}^{trial} - 3G\Delta p - r - \sigma_{yield}}{3G + h} \tag{7.4}$$

$$\Delta p = \Delta p_{old} + residual \tag{7.5}$$

In step 3. r_{old} is the hardening variable from the previous time step, h is the hardening constant, which defines the slope of the linear strain hardening section of the stress vs. strain plot, Δp and Δp_{old} are the plastic strain increment for the current and previous time steps respectively, and G is the shear modulus. In this Newton iteration, the residual is driven to some predefined small number as the hardening variable r and the plastic strain increment Δp are updated to achieve such a small residual.

4. When the residual is sufficiently small, the new plastic strain increment is used to update a plastic strain increment tensor ($\Delta\varepsilon_p$) that is used to calculate an elastic strain ($\Delta\varepsilon_e$) from the total strain ($\Delta\varepsilon$) and a new stress increment is calculated using this new elastic strain.

$$\Delta\varepsilon^p = \frac{3}{2}\Delta p \frac{\sigma_{dev}^{trial}}{\sigma_{eff}^{trial}}, \tag{7.6}$$

$$\Delta\varepsilon^e = \Delta\varepsilon - \Delta\varepsilon^p, \tag{7.7}$$

$$\Delta\sigma = \mathbf{C}\Delta\varepsilon^e \tag{7.8}$$

5. Now, the stress and the plastic strain are updated

$$\sigma = \sigma_{old} + \Delta\sigma \tag{7.9}$$

$$p = p_{old} + \Delta p \tag{7.10}$$

6. In conventional nonlinear solvers, the material Jacobian is calculated and used to solve the nonlinear problem. Note however, that the material Jacobian is NOT required using the JFNK method. It can be used as a preconditioner and it is therefore presented here.

$$\frac{\partial\delta\sigma}{\partial\delta\varepsilon} = 2GQ\frac{\sigma_{dev}^{trial}}{\sigma_{eff}^{trial}}\frac{\sigma_{dev}^{trial}}{\sigma_{eff}^{trial}} + 2GRI + \left(K - \frac{2}{3}GR\right)II \tag{7.11}$$

where

$$R = \frac{\sigma_{eff}^{trial} - 3G\Delta p}{\sigma_{eff}^{trial}} \tag{7.12}$$

and

$$Q = \frac{3}{2}\left(\frac{h}{h+3G}\right) - R \tag{7.13}$$

The source used for guidance in implementing this plasticity model into BISON was "Introduction to Computational Plasticity" [8].

8 Material and Behavioral Models

8.1 FeCrAl

8.1.1 Thermal Properties `[ThermalFeCrAl]`

There are a variety of Iron-Chromium-Aluminum (FeCrAl) alloys being considered as potential accident tolerant fuel (ATF) cladding concepts. Temperature dependent thermal conductivity and specific heat capacity has been included for four FeCrAl alloys: Kanthal APMT, Special Metals MA956, Plansee PM2000, and Resistalloy International Fecralloy. The thermal conductivity and specific heat capacity are given in tabular form in data sheets for all alloys with the exception of Fecralloy which is given as a constant value for all temperatures on its data sheet. These alloys were chosen based upon discussions with FCRD cladding expert Stu Maloy and investigations of industry efforts. Since no additional information is given about the behavior as a function of temperature, the material properties are linearly interpolated between the values provided in the table. For temperatures outside of the range provided in the table the material property is taken as the closest known value to avoid extrapolation into areas where no data is known. A fifth FeCrAl alloy has been added as an option known as C35M which is an Oak Ridge National Laboratory cladding alloy. No thermal properties have been reported for this material and therefore the thermal conductivity and specific heat for Kanthal APMT is used when C35M is used.

The tabulated data for MA956 [9], PM2000 [10], and Kanthal APMT [11] are reproduced in Tables 8.1, 8.2, and 8.3, respectively. The thermal conductivity and specific heat capacity of Fecralloy are given as constant values of 16.0 W/m-K and 460 J/kg-K respectively [12].

8.1.2 Mechanical Properties `[MechFeCrAl]`

The mechanical properties of the FeCrAl alloys include Young's Modulus, Poisson's ratio, coefficient of thermal expansion, thermal creep and irradiation creep. Similarly to the thermal material properties introduced in the previous section, the Young's Modulus and coefficient of thermal expansion are provided in tabular format. The material property of interest is linearly interpolated between the data points available for the respective material. Note that the coefficient of thermal expansion is provided as an incremental coefficient and is converted into an instantaneous coefficient prior to interpolation inside the code. The tabulated data for MA956 [9], PM2000 [10], Kanthal APMT [11], and Fecralloy [12] are reproduced in Tables 8.4, 8.5, 8.6, and 8.7 respectively. The Poisson's ratio of MA956, PM2000, Kanthal APMT, and Fecralloy are 0.3, 0.33, 0.3 and 0.3 respectively.

Table 8.1: Temperature dependent thermal conductivity and specific heat capacity of MA956 alloy

Temperature [K]	**Thermal Conductivity [W/m-K]**	**Specific Heat Capacity [J/kg-K]**
293.15	10.9	469
373.15	12.2	491
473.15	13.9	519
573.15	15.4	547
673.15	16.9	575
773.15	18.4	608
873.15	19.8	630
973.15	21.2	658
1073.15	22.6	686
1173.15	24.1	714
1273.15	25.5	741
1373.15	27	769

Table 8.2: Temperature dependent thermal conductivity and specific heat capacity of PM2000 alloy

Temperature [K]	**Thermal Conductivity [W/m-K]**	**Specific Heat Capacity [J/kg-K]**
293.15	10.9	
373.15		500
473.15	16	480
773.15	21	610
1073.15	22	680
1273.15	25.5	740
1473.15	28	

Table 8.3: Temperature dependent thermal conductivity and specific heat capacity of Kanthal APMT alloy

Temperature [K]	**Thermal Conductivity [W/m-K]**	**Specific Heat Capacity [J/kg-K]**
293.15		480
323.15	11	
473.15		560
673.15		640
873.15	21	710
1073.15	23	670
1273.15	27	690
1473.15	29	700

A fifth FeCrAl alloy has been added called C35M that has been developed at ORNL [13]. The temperature dependent equations for Young's Modulus and Poisson's Ratio of C35M are given

by:

$$E = -5.46 \times 10^{-5}(T - 273.15)^2 - 3.85 \times 10^{-2}(T - 273.15) + 1.99 \times 10^2 \tag{8.1}$$

and

$$\nu = 3.85^{-5}(T - 273.15) + 2.68 \times 10^{-1} \tag{8.2}$$

respectively, where T is the temperature in K, and E is the Young's Modulus in GPa.

Table 8.4: Temperature dependent Young's Modulus and CTE of MA956 alloy

Temperature [K]	**Young's Modulus [GPa]**	**Temp. Range [°C]**	**CTE [μm/m-K]**
310.45	172	20	-
362.30	170	20 - 100	11.3
424.44	167	20 - 200	11.6
506.42	161	20 - 300	11.9
592.27	153	20 - 400	12.3
657.76	146	20 - 500	12.7
754.04	139	20 - 600	13.0
828.41	131	20 - 700	13.4
900.57	121	20 - 800	13.9
984.39	114	20 - 900	14.4
1066.55	107	20 - 1000	14.9
1146.44	99.4	20 - 1100	15.5
1208.19	89.1		
1269.02	77.0		
1347.65	72.7		

Table 8.5: Temperature dependent Young's Modulus and CTE of PM2000 alloy

Temperature [K]	**Young's Modulus [GPa]**	**Temp. Range [°C]**	**CTE [μm/m-K]**
473.15	160	20	12.4
673.15	145	20 - 100	13.1
873.15	125	20 - 250	13.6
973.15	115	20 - 500	14.7
1073.15	110	20 - 1000	15.4
1223.15	95		

8.1.3 Thermal Creep `[MechFeCrAl]`

Thermal creep data exsists for Incoloy MA956, Kanthal APMT, Fecralloy and C35M. However, the data provided for Kanthal APMT is not in a correlated form that allows for implementation into BISON. Therefore the thermal creep strain for both Kanthal APMT and PM2000 is set

Table 8.6: Temperature dependent Young's Modulus and CTE of Kanthal APMT alloy

Temperature [K]	**Young's Modulus [GPa]**	**Temp. Range [°C]**	**CTE [μm/m-K]**
293.15	220	20 - 250	10.7
373.15	210	20 - 500	12.0
473.15	205	20 - 750	12.2
673.15	190	20 - 1000	12.5
873.15	170	20 - 1200	15.1
1073.15	150		
1273.15	130		

Table 8.7: Temperature dependent Young's Modulus and CTE of Fecralloy

Temperature [K]	**Young's Modulus [GPa]**	**Temp. Range [°C]**	**CTE [μm/m-K]**
293.15	180	20 - 250	11.0
		20 - 500	12.0
		20 - 1000	15.0

to zero in this material model until further data is available. The details of the thermal creep correlations for MA956, Fecralloy and C35M is provided in the following sections.

8.1.3.1 MA956

The thermal creep rate of MA956 is calculated by a Norton creep law as proposed by Seiler et al. [14]:

$$\dot{\varepsilon} = \underbrace{A_0 \cdot \exp(\alpha T) \cdot \exp\left(-\frac{Q}{RT}\right)}_{\mathrm{A}} \cdot \sigma^n \tag{8.3}$$

where Q is the activation energy, n is the creep exponent and α an additional factor. The creep behavior of MA956 is characterized by three regimes with independent sets of creep parameters. The transition from one regime to another takes place at the critical stress σ_{c1} and σ_{c2}. These critical stresses are calculated during the simulation by equating two equations with the different creep parameters in the two regimes. For example the first critical stress is defined as

$$\sigma_{c1} = \left(\frac{A_1}{A_2}\right)^{\frac{1}{n_2 - n_1}} \tag{8.4}$$

where $A_1(A_0, Q, \alpha, R, T)$ and n_1 are parameters in the range $\sigma < \sigma_{c1}$, and $A_2(A_0, Q, \alpha, R, T)$ and n_2 are parameters in the range $\sigma_{c1} < \sigma < \sigma_{c2}$, respectively. Table 8.8 lists the creep parameters of MA956 for the various stress regimes.

Table 8.8: Creep parameters of MA956

	A_0 $[MPa^{-n}s^{-1}]$	n [-]	Q [kJ/mol]	α $[K^{-1}]$
$\sigma < \sigma_{c!}$	78.978	4.9827	453	0.0
$\sigma_{c1} < \sigma < \sigma_{c2}$	3.466×10^{-124}	41.0	453	0.1
$\sigma > \sigma_{c2}$	8.68×10^{16}	5.2911	486	-0.0122

8.1.3.2 Fecralloy

The model for thermal creep of Fecralloy is in the form of a Norton creep law as proposed by Saunders et al. [15]. The coefficient in the Norton law is in the form of an Arrhenius equation.

$$\dot{\varepsilon} = 5.96 \times 10^{-27} \sigma^{5.5} \exp\left(-\frac{47136}{T}\right) \tag{8.5}$$

where σ is the effective stress in Pa and T is the temperature in K.

8.1.3.3 C35M

The model for thermal creep of C35M is in the form of a Norton creep law. As proposed by Terrani et al. [16], below 873 K the following correlation for thermal creep is adopted

$$\dot{\varepsilon} = 2.89 \times 10^{-36} \sigma^{5.5} \exp\left(-\frac{29709}{T}\right) \tag{8.6}$$

while above 873 K, the correlation proposed by Saunders et al. [15] is employed

$$\dot{\varepsilon} = 5.96 \times 10^{-27} \sigma^{5.5} \exp\left(-\frac{47136}{T}\right) \tag{8.7}$$

where $\dot{\varepsilon}$ is the creep rate (s^{-1}), σ the effective stress (Pa) and T (K) is the temperature.

8.1.4 Irradiation Creep `[MechFeCrAl]`

The model incorporated into BISON for irradiation creep of FeCrAl alloys is taken from [16]. The coefficient for irradiation creep recommended is 5×10^{-6} per MPa per dpa. Utilizing the following conversion factor: 1×10^{25} n/m^2 = 0.9 dpa, a correlation for irradiation creep can be derived.

$$\dot{\varepsilon} = 4.5 \times 10^{-31} \sigma \phi \tag{8.8}$$

where σ is the effective stress in MPa and ϕ is the fast neutron flux in n/m^2-s.

8.1.5 Isotropic Swelling `[VSwellingFeCrAl]`

It is expected that FeCrAl alloys will be subjected to irradiation induced swelling due to their cubic crystal structure. As an approximation for the swelling of FeCrAl alloys a simplistic model provided in [16] has been implemented in BISON. The estimated swelling rate is 0.05% per dpa.

Using the same conversion factor as suggested above for irradiation creep (1×10^{25} n/m^2 = 0.9 dpa) the volumetric swelling strain rate is given by:

$$\dot{\varepsilon} = 4.5 \times 10^{-29} \phi \tag{8.9}$$

Integrating over time the volumetric swelling is given by

$$\varepsilon = 4.5 \times 10^{-29} \Phi \tag{8.10}$$

where Φ is the fast neutron fluence given in n/m^2.

8.1.6 Oxidation and Corrosion `[FeCrAlOxideAux]`

The oxidation of FeCrAl cladding is calculated based upon a parabolic rate law to determine the mass gain of oxide. The mass gain is then converted into an oxide thickness. Currently, the oxidation model is not coupled to the CoolantChannel model to affect the heat transfer coefficient as the cladding becomes oxidized. The model presented here was developed for Kanthal APMT which is one of the candidate ATF FeCrAl cladding alloys. The model was also developed for high temperature steam, resulting in low oxidation rates at normal operating temperatures. It is expected that oxidation of FeCrAl alloys will be negligible during normal operation and the model can be applied to the normal operating regime. The parabolic rate constant was determined by Pint et al. [17]:

$$k_p = k_o e^{-Q/T} \tag{8.11}$$

where k_p is the parabolic rate constant in units of g^2/cm^4-s, k_o is a constant equal to 7.84 g^2/cm^4-s, and Q is an activation energy in units of K with a value of 41373.7. The mass gain due to the oxide formation is then calculated by

$$w_g = k_p^{1/2} t^{1/2} \tag{8.12}$$

where w_g is the mass gain due to oxidation in units of mg/cm^2. Then the oxide thickness is determined by multiplying the mass gain by the conversion factor of 5.35 μm-(cm^2/mg) as proposed by Jönsson et al [18].

8.1.7 Isotropic Plasticity `[IsoPlasticityFeCrAl]`

The isotropic plasticity model for the ORNL C35M alloy can be used with the combined creep and plasticity model available within MOOSE. This model calculates the yield stress as a function of temperature based upon experimental data by Yamamoto et al. [19]. The data is obtained from Figure 10 in the reference. Table 8.9 shows the yield stress values as a function of temperature. These tabulated values are treated as a PiecewiseLinear function of temperature. The minimum or maximum value for yield stress is used if the temperature is outside the bounds presented here.

Table 8.9: Yield Stress as a Function of Temperature

Temp. Range [K]	Yield Stress [MPa]
290.735	446.819
546.411	313.964
640.150	295.872
824.832	225.901
1007.24	67.237

8.1.8 Failure `[FailureFeCrAl]`

The failure model for FeCrAl cladding checks whether the hoop stress has exceeded the ultimate tensile strength (UTS). This model calculates the UTS as a function of temperature based upon experimental data by Yamamoto et al. [19]. The data is obtained from Figure 10 in the reference. Table 8.10 shows the UTS values as a function of temperature. These tabulated values are treated as a PiecewiseLinear function of temperature. The minimum or maximum value for UTS is used if the temperature is outside the bounds presented here.

Table 8.10: Ultimate Tensile Strength as a Function of Temperature

Temp. Range [K]	UTS [MPa]
294.738	569.475
551.495	543.205
644.048	527.023
829.85	288.826
1011.95	65.373

8.2 HT9 Martensitic Steel

8.2.1 Thermal Properties `[ThermalHT9]`

Thermal conductivity k (W/m-K) of HT9 is from [20]:

$$k = 17.622 + 2.42 \times 10^{-2} T - 1.696 \times 10^{-5} T^2, \qquad T < 1030 \text{ K} \tag{8.13}$$

$$k = 12.027 + 1.218 \times 10^{-2} T, \qquad T \geq 1030 \text{ K} \tag{8.14}$$

Specific heat C_p (J/kg-K) of HT9 is from [21]:

$$C_p = (T - 500)/6 + 500, \qquad T < 800 \text{ K} \tag{8.15}$$

$$C_p = 3(T - 800)/5 + 550, \qquad T \geq 800 \text{ K} \tag{8.16}$$

8.2.2 Mechanical Properties `[MechHT9]`

Young's modulus (MPa) and Poisson's ratio for HT9 are reported by [22].

$$E = 234468.6944 - 79.65914T - 0.0131706T^2 \tag{8.17}$$

$$v = 0.221956 + 2.643235 \times 10^{-4}T - 2.028888 \times 10^{-7}T^2 \tag{8.18}$$

Linear thermal expansion coefficient (%) [20] is:

$$\Delta L/L = -0.2191 + 5.678 \times 10^{-4}T + 8.111 \times 10^{-7}T^2 - 2.576 \times 10^{-10}T^3 \tag{8.19}$$

T is temperature in K.

8.2.3 Thermal and Irradiation Creep `[ThermalIrradiationCreepHT9]`

Thermal and irradiation creep models and material properties from [23] are used for the HT9 model. The following equation is for secondary creep.

$$\dot{\varepsilon}_{cr} = C_5 \exp(-\frac{Q_4}{RT})\bar{\sigma}^2 + C_6 \exp(-\frac{Q_5}{RT})\bar{\sigma}^5 + [B_o + A\exp(-\frac{Q}{RT})]\phi\bar{\sigma}^{1.3} \tag{8.20}$$

where:

$C_5 = 1.17 \times 10^9$
$C_6 = 8.33 \times 10^9$
$Q_4 = 83142$ (Cal/g-mol)
$Q_5 = 108276$ (Cal/g-mol)
$B_o = 1.83 \times 10^{-4}$
$A = 2.59 \times 10^{14}$
$Q = 73000$ (Cal/g-mol)
$R = 1.987$ (Cal/g-mol)
$T =$ Temperature (K)
$\phi =$ Neutron Flux$(10^{22}$ n/cm^2/s$)$
$\bar{\sigma} =$ Effective stress (MPa)
$\dot{\varepsilon}_{cr} =$ Effective Thermal and Irradiation Creep Strain Rate (%/s)

8.2.4 Creep-fracture Failure `[FailureCladHT9]`

Two creep-fracture failure models are available in BISON similar to the approach used in [24]. Slow transients, such as burnup, are handled by the "steady state" Cumulative Damage Fraction (CDF) model [25]. Fast transients are handled with the Constrained Cavity Growth (CCG) with Diffusion and Creep with Sliding (D&CS) model [26].

8.2.4.1 Cumulative Damage Fraction

The CDF model compares the time-to-rupture value with experimentally obtained results as a function of stress and absolute temperature. When this value (CDF) equals one, the material has failed.

$$CDF = \int_0^t \frac{\mathrm{d}t}{t_r(\sigma, T)}. \tag{8.21}$$

The time of rupture t_r function in hours is found in

$$C_T \theta = t_r e^{\frac{-Q_L}{RT}} \tag{8.22}$$

where Q_L is 154 kcal/mole K for long transients, R is the Boltzmann constant, and T is the absolute temperature in K. C_T is the Dorn parameter coefficient ranging from 3.915×10^{-24} at 650 °C to 1 at 600 °C. The Dorn parameter θ comes from the curve fit of

$$\log_{10}\theta = 2028.9 - 800.13\log_{10}\sigma_\theta + 105.26(\log_{10}\sigma_\theta)^2 - 4.63886(\log_{10}\sigma_\theta)^3 \tag{8.23}$$

where σ_θ is the hoop stress in Pa.

At temperatures outside of the range of the Dorn parameter coefficient C_T, the value is set to the appropriate end value to avoid extrapolation. Interpolation of the value is conducted within the temperature range.

8.2.4.2 Constrained Cavity Growth

The CCG with D&CS model calculates the crack radius a of periodic cavities along grain boundaries. The cavity centers are spaced equally at a distance of $2b$. Failure occurs when $a = b$.

The crack radius growth rate $\dot{a}$ is related to the cavity volume growth rate $\dot{V}$ by

$$\dot{a} = \frac{\dot{V}}{4\pi a^2 h(\psi)} \tag{8.24}$$

with $h(\psi)$ being defined as

$$h(\psi) = \frac{1}{\sin\psi}\left[\frac{1}{1+\cos\psi} - \frac{\cos\psi}{2}\right] \tag{8.25}$$

where $\cos\psi = \gamma_b/2\gamma_s$ being the ratio of the grain boundary free energy to twice the grain surface free energy.

The volume growth rate $\dot{V}$ is the sum of the rigid grain growth rate $\dot{V}_1$ and power law creeping material growth rate $\dot{V}_2$ for $a/L \leq 10$.

$$\dot{V}_1 = 4\pi D \frac{\sigma_n - (1-f)\sigma_s}{\ln(1/f) - (3-f)(1-f)/2} \tag{8.26}$$

$$\dot{V}_2 = \begin{cases} \pm 2\pi\dot{\varepsilon}_e^C a^3 h(\psi)\left[\alpha_n\left|\frac{\sigma_m}{\sigma_e}\right| + \beta_n\right]^n, & \text{for } \pm\frac{\sigma_m}{\sigma_e} > 1 \\ 2\pi\dot{\varepsilon}_e^C a^3 h(\psi)\left[\alpha_n + \beta_n\right]^n \frac{\sigma_m}{\sigma_e}, & \text{for } \left|\frac{\sigma_m}{\sigma_e}\right| \leq 1 \end{cases} \tag{8.27}$$

The average normal stress is σ_n. The sintering stress can be calculated as $\sigma_s = \gamma_s(\sin\psi)/a$. The grain boundary diffusion parameter is $D = D_B\delta_B\Omega/RT$ where $D_B\delta_B$ is the boundary diffusivity, Ω is the atomic volume, R is the Boltzmann constant, and T is the absolute temperature in K. The area fraction of the grain boundary f is determined with

$$f = \max\left\{\left(\frac{a}{b}\right)^2, \left(\frac{a}{a+1.5L}\right)^2\right\}. \tag{8.28}$$

where $L = (D\sigma_e/\dot{\varepsilon}_e^C)^{1/3}$. The Von Mises stress is σ_e. The hydrostatic (mean) stress is σ_m. The effective creep strain-rate is $\dot{\varepsilon}_e^C$. With the assumption that the material follows a power law creep, n is the value of the power, $\alpha_n = 3/2n$, and $\beta_n = (n-1)(n+0.4319)/n^2$.

The crack length is assumed to begin at a minimum value. The crack length is never allowed to fall below this value. The crack may shrink after it has grown. However, after failure has occurred, the crack is assumed to be permanent and can no longer shorten. The crack length is found by taking the calculated growth rate $\dot{a}$ and multiplying by the current time increment.

8.3 Molybdenum

8.3.1 Thermal Properties `[ThermalMo]`

Thermal conductivity k (W/m-K) of pure Mo metal is from [27]:

$$k = 9.128\times10^{-6}T^2 - 4.945\times10^{-2}T + 152.0 \tag{8.29}$$

Specific heat C_p (J/kg-K) of pure Mo metal is from [28]:

$$C_p = 9.74\times10^{-6}T^2 + 5.37\times10^{-2}T + 235 \tag{8.30}$$

8.3.2 Mechanical Properties `[MechMo]`

Young's modulus (Pa) and Poisson's ratio for pure Mo:

$$E = 3.349\times10^{11} - 5.101\times10^{7}T \tag{8.31}$$

$$v = 0.31 \tag{8.32}$$

Linear thermal expansion coefficient ($\frac{m}{m}$) is:

$$\Delta L/L = (-4.985\times10^{-6} + 6.667\times10^{-10}T)(T - 273.15) \tag{8.33}$$

T is temperature in K.

8.4 Nickel-base Alloy PK33

8.4.1 Thermal Properties `[ThermalAlloy33]`

Thermal conductivity k (W/m-K) of Alloy PK33 is from [29]:

$$k = 1.4617 \times 10^{-2} T + 9.1233 \tag{8.34}$$

Specific heat C_p (J/kg-K) of Alloy PK33 is:

$$C_p = 0.177T + 431.0 \tag{8.35}$$

8.4.2 Mechanical Properties `[MechAlloy33]`

Young's modulus (Pa) and Poisson's ratio for Alloy PK33, from [29].

$$E = 2.358 \times 10^{11} - 1.667 \times 10^{8} T + 8.737 \times 10^{4} T^2 \tag{8.36}$$

$$v = 0.31 \tag{8.37}$$

Linear thermal expansion coefficient ($\frac{m}{m}$) is:

$$\Delta L/L = 1.699 \times 10^{-5} T - 5.177 \times 10^{-3} \tag{8.38}$$

T is temperature in K.

8.5 Pyrolitic Carbon

8.5.1 Irradiation-induced Strain `[PyCIrradiationStrain]`

Pyrolitic carbon experiences irradiation-induced strain which is a function of fluence. For low-density pyrolitic carbon, such as that used in the buffer layer of a TRISO fuel particle, the irradiation strain is given by [30] as

$$\dot{\varepsilon}_r = \dot{\varepsilon}_\theta = -0.176\, e^{(-1.75\Phi)} \tag{8.39}$$

where $\dot{\varepsilon}$ is in units of $1/(10^{25}\mathrm{n/m}^2)$ and Φ, the fluence, is in units of $10^{25}\mathrm{n/m}^2$.

For dense pyrolitic carbon, the irradiation strain differs in the radial and tangential directions [30] of a TRISO particle:

$$\dot{\varepsilon}_r = -0.077\, e^{(-\Phi)} + 0.031 \tag{8.40}$$

$$\dot{\varepsilon}_\theta = -0.036\, e^{(-2.1\Phi)} - 0.01. \tag{8.41}$$

8.5.2 Irradiation Creep `[CreepPyC]`

The irradiation creep correlation is taken from [30] and [31]. With K as the creep constant, σ_i as one component of the principal stress, ν_c as the Poisson ratio for creep, and $\dot{\Phi}$ as the fast neutron flux, the creep rate is given as

$$\dot{\varepsilon}_1 = K[\sigma_1 + \nu_c(\sigma_2 + \sigma_3)]\dot{\Phi}. \tag{8.42}$$

The value of ν_c is 0.5. K is

$$K = K_0[1 + 2.38(1.9 - \rho)]M_{\text{Irr,Creep}} \tag{8.43}$$

where

$$K_0 = 1.996 \times 10^{-29} - 4.415 \times 10^{-32}T + 3.6544 \times 10^{-35}T^2 \tag{8.44}$$

and with $M_{\text{Irr,Creep}} = 2$, ρ in g/cm^3 and T in C. At the expense of inverting a 3×3 matrix, it is possible to determine the creep strain increment in an implicit fashion, allowing arbitrarily large time steps without unstable creep response.

8.6 Silicon Carbide

8.6.1 Irradiation Creep `[CreepSiC]`

The model for irradiation creep of silicon carbide (SiC) is taken as (see [32]):

$$\dot{\varepsilon}_{cr} = K\sigma\phi \tag{8.45}$$

where $\dot{\varepsilon}_{cr}$ is the irradiation creep rate, K is a temperature-dependent conversion factor (Pa-n/m^2)$^{-1}$, σ is the stress, and ϕ is the flux.

The reference mentioned above gives K as 2×10^{-37} (Pa-n/m^2)$^{-1}$ at 640° C and 4×10^{-37} (Pa-n/m^2)$^{-1}$ at 900° C. However, a figure in that reference seems to indicate that typical values for K are about one-tenth those mentioned in the text. Little creep data for SiC is available at lower temperatures.

8.7 Stainless Steel 316

8.7.1 Thermal Properties `[Thermal316]`

Thermal conductivity k (W/m-K) of SS 316 is fitted from [33]:

$$k = -7.301 \times 10^{-6}T^2 + 2.716 \times 10^{-2}T + 6.308 \tag{8.46}$$

Specific heat C_p (J/kg-K) of SS 316 is from [33]:

$$C_p = 428.46 + 0.1816T \tag{8.47}$$

8.7.2 Mechanical Properties `[MechSS316]`

Young's modulus (Pa) and Poisson's ratio for SS 316.

$$E = 2.15946 \times 10^{11} - 7.07727 \times 10^{7} T \tag{8.48}$$

$$v = 0.31 \tag{8.49}$$

Linear thermal expansion coefficient ($\frac{m}{m}$) is:

$$\Delta L/L = -4.34 \times 10^{-3} + 1.45 \times 10^{-5} T + 3.766 \times 10^{-9} T^2 \tag{8.50}$$

T is temperature in K.

8.8 UO_2 and MOX

8.8.1 Thermal Properties - UO_2 `[ThermalFuel]`

Five empirical models are available in BISON to compute UO_2 thermal conductivity and its dependence on temperature, porosity, burnup, and, for four of the models, Gadolinia content. Choices for UO_2 fuel include models referred to as Fink-Lucuta [34][35], Halden [36], NFIR [37][38], MATPRO [39], and modified NFI [40] (modifications described in [36]). The Halden, MATPRO, NFIR and modified NFI models can account for Gadolinia content.

Empirical fits for the temperature dependent specific heat of UO_2 accompany both the Fink-Lucuta and MATPRO conductivity models.

For the most part, the thermal conductivity of urania is represented as the sum of a lattice vibration (phonon) and an electronic (electron hole pair effect) term or for unirradiated material at 95% theoretical density (TD)

$$\mathrm{k_{95}} = \mathrm{k_{phonon}} + \mathrm{k_{electronic}} \tag{8.51}$$

The first term in Equation 8.51 is typically inversely proportional to the sum of temperature and burnup dependent functions, while the second term, usually an exponential function of inverse temperature, is inversely proportional to temperature or temperature squared. For example,

$$\mathrm{k_{phonon}} = 1.0/(\mathrm{A} + \mathrm{B} * \mathrm{T} + \mathrm{f(Bu)} + \mathrm{g(Bu)} * \mathrm{h(T)}) \tag{8.52}$$

$$\mathrm{k_{electronic}} = \mathrm{i(T)} * \exp(-\mathrm{F/T}) \tag{8.53}$$

where A, B, and F are constants, Bu is burnup, T is temperature, and f, g, h, and i are functions of burnup or temperature. While each of the thermal conductivity models has the basic form given by Equations 8.52 and 8.53, each has their own specific set of constants and perhaps additional corrections that account for effects of dissolved fission products, precipitated fission products, porosity, deviation from stoichiometry, and radiation damage. In general, the final conductivity corrected for these effects is given as

$$\mathrm{k} = \mathrm{k_{95}} * \mathrm{f_d} * \mathrm{f_p} * \mathrm{f_{por}} * \mathrm{f_x} * \mathrm{f_r} \tag{8.54}$$

where:

f_d – dissolved fission products correction

f_p – preipitated fission products correction

f_{por} – porosity correction

f_x – deviation from stoichiometry (1.0 for urania fuel but $\neq 1$ if Gadolinia present)

f_r – radiation damage correction

8.8.1.1 Fink-Lucuta

In the Fink-Lucuta model, the temperature-dependence of unirradiated material is defined using the equation suggested by Fink [34]. This relationship is then modified to account for the effects of irradiation, porosity and burnup using a series of multipliers, as outlined in detail by Lucuta et al. [35]. The Fink equation is

$$k_{95} = \left(\frac{100}{7.5408 + 17.692 \cdot T_n + 3.6142 \cdot T_n^2} + \frac{6400}{T_n^{5/2}} \exp\left(-\frac{16.35}{T_n} \right) \right) \tag{8.55}$$

where T_n is the temperature in K divided by 1000. Equation 8.55 is multiplied by the following factor to obtain 100% TD thermal conductivity

$$k = k_{95} \cdot \left(\frac{1}{1 - (2.6 - 0.5 \cdot T_n) \cdot 0.05} \right) \tag{8.56}$$

Equation 8.56 is then corrected per Equation 8.54 as perscribed by Lucuta where

$$f_d = \left(\frac{1.09}{bu^{3.265}} + 0.0643 \cdot \sqrt{\frac{T}{bu}} \right) \cdot \arctan\left(\frac{1.0}{\frac{1.09}{bu^{3.265}} + 0.0643 \cdot \sqrt{\frac{T}{bu}}} \right) \tag{8.57}$$

$$f_p = 1.0 + \left(\frac{0.019 \cdot bu}{3.0 - 0.019 \cdot bu} \right) \cdot \left(\frac{1.0}{1.0 + \exp\left(\frac{-(T-1200)}{100} \right)} \right) \tag{8.58}$$

$$f_{por} = \left(\frac{1.0 - p}{1.0 + 0.5 \cdot p} \right) \tag{8.59}$$

$$f_r = 1.0 - \frac{0.2}{1.0 + \exp\left(\frac{(T-900)}{80} \right)} \tag{8.60}$$

where T is the temperature in K, p is the porosity, and bu is the burnup in at.%.

The Fink-Lucuta model is valid from 298 to 3120 K [41].

8.8.1.2 MATPRO

The MATPRO model [39] is based on an equation proposed by Ohira and Itagakia [40]. The thermal conductivity for 95% theroetical density is given as

$$k_{95} = 1/(\text{term0} + \text{term1} + \text{term2} + \text{term3} + \text{term4} \cdot \text{term5}) + \text{term6} \tag{8.61}$$

where the recriprocal expression and term6 correspond to k_{phonon} and $k_{electronic}$, respectively. The terms are defined as

$$\begin{aligned}
&\text{term0} = 0.0452 \\
&\text{term1} = 0.000246 \cdot \text{T} \\
&\text{term2} = 0.00187 \cdot \text{Bu} \\
&\text{term3} = 1.1599 \cdot \text{Gdcon} \\
&\text{term4} = (1 - 0.9 \cdot \exp(-0.04 \cdot \text{Bu})) \cdot 0.038 \cdot \text{Bu}^{0.28} \\
&\text{term5} = 1/(1 + 396 \cdot \exp(\text{-}6380/\text{T})) \\
&\text{term6} = 3.5\text{e}9/\text{T}^2 \cdot \exp(\text{-}16360/\text{T})
\end{aligned}$$

and T is temperature in K, Bu is burnup in MWd/kgU, and Gdcon is the Gadolinia concentration in wt.%. Equation 8.61 is multiplied by the appropriate factor to return the thermal conductivity to 100% TD and then multiplied by a density correction factor (similar to Equation 8.59 but written in terms of %TD) to provide a thermal conductivity representative of the material of interest

$$k = k_{95} \cdot 1.0789 \cdot \frac{D}{(1 + 0.5 \cdot (1 - D))} \tag{8.62}$$

where D is the fractional TD. The multiplier 1.0789 is the inverse of the density correction factor evaluated at 0.95 TD.

The MATPRO correlation is valid over the following ranges [36]

$$\begin{aligned}
&300 \leq \text{T (K)} \leq 3000 \\
&0 \leq \text{Bu} \leq 62 \text{ MWd/kgU} \\
&0.92 \leq \text{D} \leq 0.97 \\
&0 \leq \text{Gdcon} \leq 10 \text{ wt.\%}
\end{aligned}$$

Figure 8.1 compares the two models as a function of temperature and burnup for fully dense UO_2.

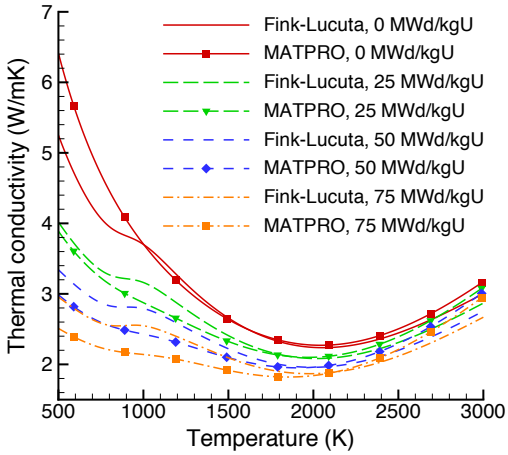

Figure 8.1: A comparison of the Fink-Lucuta and MATPRO empirical models for the thermal conductivity of full density UO_2, as a function of temperature and burnup.

8.8.1.3 Halden

The Halden model has the same form as Equation 8.61. However, the terms are different, and different temperature and burnup units are used. For 95% TD fuel, the terms are

$$\text{term0} = 0.1148$$
$$\text{term1} = 1.1599 \cdot \text{Gdcon}$$
$$\text{term2} = 1.1599 \cdot f_x$$
$$\text{term3} = 4\text{e-}3 \cdot \text{BuUO2}$$
$$\text{term4} = 2.475\text{e-}4 \cdot (1 - 3.33\text{e-}3 \cdot \text{BuUO2}) \cdot \min(1650,\text{Tc})$$
$$\text{term5} = 1$$
$$\text{term6} = 1.32\text{e-}2 \cdot \exp(0.00188 \cdot \text{Tc})$$

where Gdcon is the Gadolinia concentration in wt.%, f_x is the deviation from stoichiometry, i.e. (2 - oxygen/metal ratio), BuUO2 is the burnup in MWd/kgUO2, and Tc is the temperature in C. Equation 8.62 is used to compute the thermal conductivity at the TD of interest.

The Halden UO_2 correlation is valid over the following ranges [36]

$$300 \leq \text{T (K)} \leq 3000$$
$$0 \leq \text{Bu} \leq 62 \text{ MWd/kgU}$$
$$0.92 \leq \text{D} \leq 0.97$$
$$0 \leq \text{Gadolinia content} \leq 10 \text{ wt.\%}$$

Figure 8.2 compares the the Fink-Lucuta and Halden models as a function of temperature and burnup for 95% theoretical density UO_2.

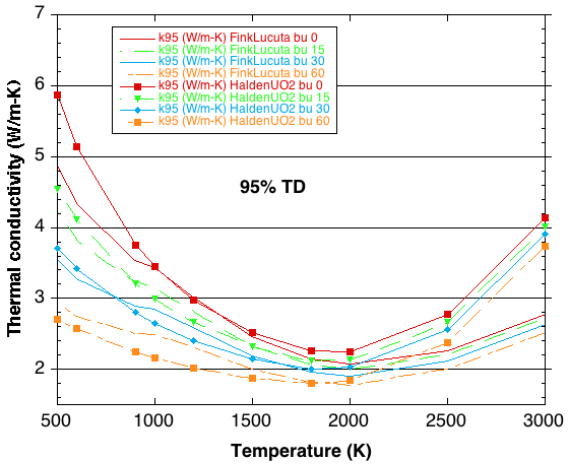

Figure 8.2: A comparison of the Fink-Lucuta and Halden empirical models for the thermal conductivity of 95% theoretical density UO_2, as a function of temperature and burnup.

8.8.1.4 NFIR

The NFIR correlation also has the general form of Equation 8.51. However, the NFIR model contains a temperature dependent thermal recovery function that accounts for self-annealing of defects in the fuel as it heats up. The ultimate effect of the self-annealing is a slight increase of the thermal conductivity over a range of temperatures up to ~1200 K. As a result of this formulation, two components of k_{phonon} are used, one at the start of thermal recovery and one at the end of thermal recovery. The thermal recovery function is used to interpolate between these two values to compute k_{phonon}. Thus

$$k_{95} = (1 - \text{RF(Tc)}) \cdot k_{phonon,start} + \text{RF(Tc)} \cdot k_{phonon,end} + k_{electronic} \tag{8.63}$$

where RF(Tc) is the thermal recovery function, Tc is temperature in C, $k_{phonon,start}$ is the phonon contribution at the start of thermal recovery, and $k_{phonon,end}$ is the phonon contribution at the end

of thermal recovery. This model has a gadolinium correction asscociated with it. Gadolinium is reported as wt. % with the default set to zero. The individual terms are

$$k_{phonon,start} = 1/(term0 + 6.14e\text{-}3 \cdot Bu - 1.4e\text{-}5 \cdot Bu^2 + (2.5e\text{-}4 - 1.81e\text{-}6 \cdot Bu) \cdot Tc) \quad (8.64)$$

$$k_{phonon,end} = 1/(term0 + 2.6e\text{-}3 \cdot Bu + (2.5e\text{-}4 - 2.7e\text{-}7 \cdot Bu) \cdot Tc) \quad (8.65)$$

$$term0_{withoutGd} = 9.592e\text{-}2 \quad (8.66)$$

$$term0_{withGd} = Gdir*Gdfac \quad (8.67)$$

$$Gdir = 0.1197 \cdot Gd + (\tanh(Gd))^{0.1} + 1.214167e\text{-}2 \cdot Gd + 5.40625e\text{-}4 \cdot Gd^2 - 5.182292e\text{-}5 \cdot Gd^3 \quad (8.68)$$

$$Gdfac = (0.027273 \cdot Gd + 0.65227273) - (2.25e\text{-}2 \cdot Gd \cdot \tanh(0.00001*Bu)) \quad (8.69)$$

$$RF(Tc) = 0.5 \cdot (1+\tanh((Tc\text{-}900)/150)) \quad (8.70)$$

$$k_{electronic} = 1.32e\text{-}2 \cdot \exp(1.88e\text{-}3 \cdot Tc) \quad (8.71)$$

where Bu is burnup in MWd/kgU. Equation 8.63 is then multiplied by a temperature dependent density correction factor to get

$$k = k_{95} \frac{[1 - (2.58 - 5.8e\text{-}4 \cdot Tc) \cdot (1 - D)]}{[1 - 0.05 \cdot (2.58 - 5.8e\text{-}4 \cdot Tc)]} \quad (8.72)$$

where D is the fractional density. Figure 8.3 compares the the Fink-Lucuta and NFIR models as a function of temperature and burnup for 95% theoretical density UO_2.

8.8.1.5 Modified NFI

The modified NFI model is also of the form of Equation 8.61. Terms are defined as

$$term0 = 0.0452$$
$$term1 = 1.1599 \cdot Gdcon$$
$$term2 = 2.46e-4 \cdot T$$
$$term3 = 1.87e\text{-}3 \cdot Bu$$
$$term4 = (1 - 0.9 \cdot \exp(-0.04 \cdot Bu)) \cdot 0.038 \cdot Bu^{0.28}$$
$$term5 = 1/(1 + 396 \cdot \exp(-6380/T))$$
$$term6 = 3.5e9/T^2 \cdot \exp(-16360/T)$$

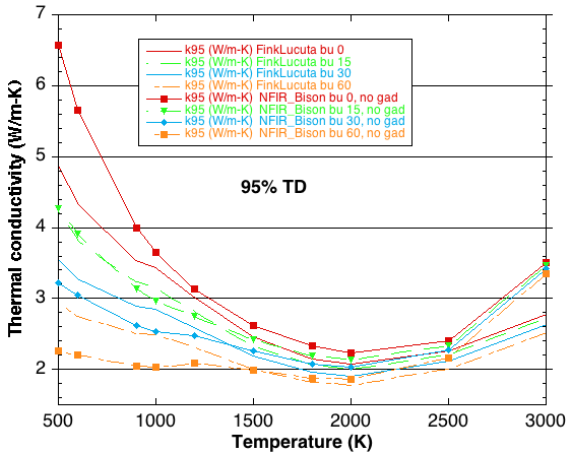

Figure 8.3: A comparison of the Fink-Lucuta and NFIR empirical models for the thermal conductivity of 95% theoretical density UO_2, as a function of temperature and burnup.

where Gdcon is the Gd concentration in wt.%, T is the temperature in K, Bu is the burnup in MWd/kgU. Again, Equation 8.62 is used to convert to the TD of interest.

The modified NFI model is valid over the following ranges [36]

$$300 \leq \text{T (K)} \leq 3000$$
$$0 \leq \text{Bu} \leq 62 \text{ MWd/kgU}$$
$$0.92 \leq \text{D} \leq 0.97$$
$$0 \leq \text{Gdcon} \leq 10 \text{ wt.\%}$$

Figure 8.4 compares the Fink-Lucuta and NFI modified models as a function of temperature and burnup for 95% theoretical density UO_2.

8.8.2 Thermal Properties - MOX `[ThermalFuel]`

Three models are available to compute MOX thermal properties. For these models, thermal conductivity of unirradiated material is first defined. In general, these relationships are then multiplied by correction factors, which account for effects of irradiation, burnup, MOX content, and porosity. The corrections factors used in BISON have been developed by Lucuta et al. [35] and are recommended by Carbajo et al. [41].

8.8.2.1 Duriez-Ronchi

The first model is recommended by Carbajo et al. in [41] and is a combination of Duriez [42] and Ronchi [43] models. In this first model, thermal conductivity of unirradiated MOX is given

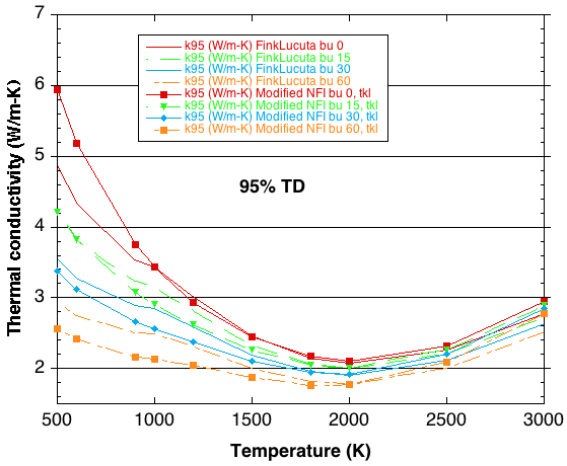

Figure 8.4: A comparison of the Fink-Lucuta and modified NFI empirical models for the thermal conductivity of 95% theoretical density UO_2, as a function of temperature and burnup.

by:

$$\lambda_0(T,x) = 1.158 \cdot \left(\frac{1}{A + CT_n} + \frac{6400}{T_n^{5/2}} \exp\left(-\frac{16.35}{T_n} \right) \right) \tag{8.73}$$

where:

$$\begin{aligned}
\lambda_0 &= \text{ thermal conductivity in } \mathrm{W \cdot m^{-1} \cdot K^{-1}} \\
T_n &= T \text{ (K)}/1000 \text{ reduced temperature} \\
x &= \text{ deviation from stoichiometry (unitless)} \\
A(x) &= 2.85x + 0.035 \\
C(x) &= -0.715x + 0.286
\end{aligned}$$

This model provides temperature and deviation from stoechiometry. It is valid from 700 to 3100 K, x less than 0.05, and plutonium concentration between 3 wt.% and 15 wt. %. According to [41], thermal conductivity does not depend on Pu concentration in this range. Thus this model is valid essentially for thermal reactor MOX.

8.8.2.2 Amaya

The second model available in BISON has been proposed by Amaya et al. [44]. Unlike the previous model, Amaya provides a plutonium concentration dependence. It starts from pure

UO_2 thermal conductivity and applies corrections to account for Pu content. Unirradiated MOX thermal conducitivity is given by:

$$\lambda_{MOX,0} = \sqrt{\frac{\lambda_0}{D_{0,Pu}\exp(D_{1,Pu}\cdot T)\cdot y}}\cdot \arctan(\sqrt{D_{0,Pu}\exp(D_{1,Pu}\cdot T)\cdot y\cdot\lambda_0}) \tag{8.74}$$

where:

$\lambda_{MOX,0} =$ MOX unirradiated thermal conductivity in $\mathrm{W}\cdot\mathrm{m}^{-1}\cdot\mathrm{K}^{-1}$

$\lambda_0 =$ UO_2 unirradiated thermal conductivity in $\mathrm{W}\cdot\mathrm{m}^{-1}\cdot\mathrm{K}^{-1}$

$T =$ temperature (K)

$y =$ plutonium concentration (wt.%)

$D_{0,Pu} = 0.209\ \mathrm{m}\cdot\mathrm{W}\cdot\mathrm{K}^{-1}$

$D_{1,Pu} = 1.09\cdot 10^{-3}\ \mathrm{K}^{-1}$

BISON uses Fink model to compute unirradiated UO_2 thermal conductivity. Amaya model's coefficients have been fitted in the temperature range from 400 K to 1500 K and the plutonium concentration up to 30 wt.% ([44]). Figure 8.5 shows a comparison of the computed thermal conductivities for the Fink-Lucuta (for reference), Fink-Amaya, and Duriez-Ronchi models for unirradiated MOX at 95% theoretical density.

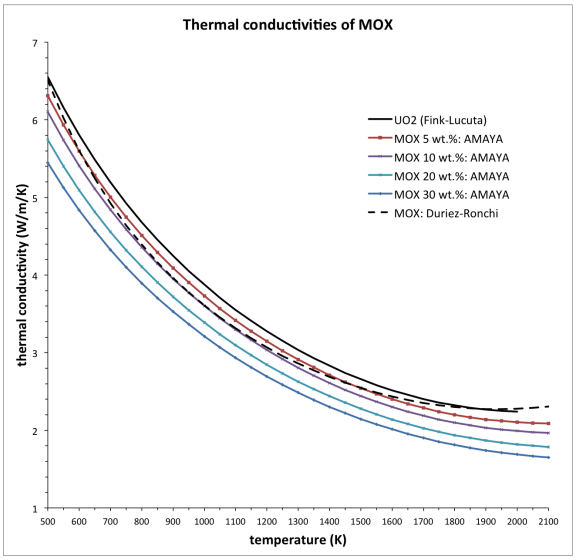

Figure 8.5: Unirradiated thermal conductivities for UO_2 and MOX from different models implemented in BISON.

8.8.2.3 Halden

The Halden correlation discussed in the previous section for urania fuel is also applicable, with one change, to MOX fuel. Reduction in thermal conductivity due to the presence of mixed oxides is accounted for by multiplying the k_{phonon} term in Equation 8.51 by 0.92. This is consistent with the statement above regarding the lack of dependence of MOX thermal conductivity on Pu concentration. The $k_{electronic}$ part of the equation is unchanged and Equation 8.62 is used to account for the TD of interest.

The Halden MOX correlation is valid over the following ranges [36]

$$300 \leq \text{T (K)} \leq 3000$$
$$0 \leq \text{Bu} \leq 62 \text{ MWd/kgU}$$
$$0.92 \leq \text{D} \leq 0.97$$
$$0 \leq \text{plutonia content} \leq 7 \text{ wt.\%}$$
$$\text{plutonia particle size} < 20\text{e-}6 \text{ m}$$

Figure 8.6 is a comparison of the Fink-Lucuta (for reference) urania correlation and the Fink-Amaya, Duriez-Ronchi, and Halden correlations for MOX for unirradiated 95% theoretical density MOX fuel with 0.07% Pu concentration.

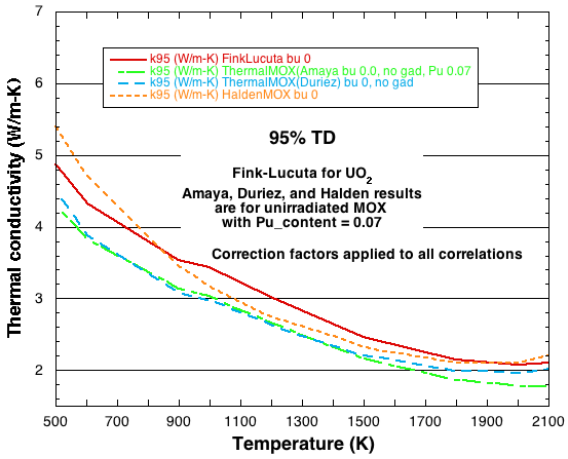

Figure 8.6: Unirradiated thermal conductivities for UO_2 (for reference) and MOX from different models implemented in BISON. Results are for 95% theoretical density and Pu concentraton of 7 wt.%. Correction factors appropriate for each correlation have been applied.

8.8.3 Thermal Properties - Fast MOX `[ThermalFastMOX]`

Mixed oxide fuels for fast reactors contain higher concentrations of plutonium oxide than their LWR counterparts. The thermal model developed by Inoue et al. [45] and used by Karahan [46] is valid for for 25% PuO_2. The thermal conductivity model for fast MOX is similar in form to the model proposed by Lucuta et al. [35] for UO_2. The model consists of an unirradiated thermal conductivity that is multiplied by corrective factors for dissolved solid fission products (F_1), precipitated solid fission products (F_2), radiation damage (F_3), and porosity (F_4) as given by:

$$k = F_1 F_2 F_3 F_4 k_0 \tag{8.75}$$

where k is the effective fuel thermal conductivity in W/m-K and k_0 is the fully dense fuel thermal conductivity in W/m-K. F_1, F_2, and F_3 are the same correlations as formulated by Lucuta et al. given by equations 8.57, 8.58, 8.60, respectively. The equation for F_4 is the modified Loeb correlation given by:

$$F_4 = 1 - \alpha P \tag{8.76}$$

where P is the volume fraction of porosity and α is a coefficient. Karahan suggests a value of 2.5 for α for conservatism.

8.8.4 Thermal Properties - Fast minor actinide MOX `[ThermalMAMOX]`

ThermalMAMOX computes the thermal conductivity of minor actinide doped (MA) mixed oxide fuel (MOX). The thermal model that was developed by M. Kato et al. [47] was used for this model. This model was based on irradiation results of experiments from the JOYO fast reactor. The experiments consisted of MOX and MA-MOX stacks of fuel with oxygen to metal ratios of 1.98 and 1.96. The correlation below was conceived from these experiments. It is important to note that the additions of 0% - 3% Am and 0% - 12% Np have been shown to have only small effects on the physical properties of the MOX fuel [47].

$$k = \left(\frac{(1-p)}{(1+0.5p)}\right)[(2.713x + 3.583E-1Am + 6.317E-2Np + 1.595E-2) \\ +(-2.625x + 2.493)\times 10^{-4}T]^{-1} + \left(\frac{1.541E11}{T^{2.5}}\right)e^{\left(\frac{-1.522e4}{T}\right)} \tag{8.77}$$

Where k is the effective fuel thermal conductivity in W/m-K, p is the fuel porosity, x is the stoichiometric deviation (2.00-x), Am is the americium content and Np is the neptunium content. Porosity can be coupled or brought in as a porosity_aux.

8.8.5 Densification `[VSwellingUO2]`

Fuel densification is computed using the ESCORE empirical model [48] given by:

$$\varepsilon_D = \Delta\rho_0 \left(e^{\left(\frac{Bu\, ln(0.01)}{C_D Bu_D}\right)} - 1\right) \tag{8.78}$$

where ε_D is the densification strain, $\Delta\rho_0$ is the total densification that can occur (given as a fraction of theoretical density), Bu is the burnup, and Bu_D is the burnup at which densification is complete. For temperatures below 750 °C the parameter C_D is given by $7.2 - 0.0086(T - 25)$; above 750 °C it is 1.0 (T in °C). To eliminate the discontinuity in C_D, BISON uses $7.235 - 0.0086(T - 25)$ below 750 °C.

In MATPRO ([39]), the same model is provided for UO_2 and MOX. As this correlation relies on a wide database, this model is also used in BISON for MOX densification.

8.8.6 Fission Product Swelling `[VSwellingUO2]`

Empirical relations from MATPRO [39] are available in BISON for calculating the swelling due to both solid and gaseous fission products. The same model is provided for both UO_2 and MOX. Solid fission product swelling is expressed as a simple linear function of burnup:

$$\Delta\varepsilon_{sw-s} = 5.577 \times 10^{-5} \rho \Delta Bu \tag{8.79}$$

where $\Delta\varepsilon_{sw-s}$ is the volumetric solid swelling increment, ΔBu the burnup increment (fissions/atoms-U), and ρ is the density (kg/m^3). Swelling due to gaseous fission products is approximated by a semi-empirical model:

$$\begin{aligned}\Delta\varepsilon_{sw-g} = 1.96 \times 10^{-31} \rho \Delta Bu (2800 - T)^{11.73} \\ * e^{-0.0162(2800-T)} e^{-0.0178 \rho Bu}\end{aligned} \tag{8.80}$$

where $\Delta\varepsilon_{sw-g}$ is the volumetric gas swelling increment, Bu and ΔBu are the burnup and burnup increment (fissions/atoms-U), respectively, ρ is the density (kg/m^3) and T is the temperature (K). Figure 8.7 shows a plot of the gaseous and total fission product swelling as a function of temperature and burnup. The MATPRO [39] correlations indicate that gaseous swelling does not become significant until above 1500 K and is saturated at a burnup of 20 MWd/kgU.

Alternatively, the gaseous fission product swelling can be calculated using a physics-based model that takes into account the coupling with the fission gas release (see Subsection 10.1).

8.8.7 Relocation `[RelocationUO2]`

One way to model the effect of UO_2 cracking on gap width is fuel relocation. Thermal gradients in a LWR fuel pellet result in corresponding stress gradients that exceed the fuel fracture stress, causing radial cracks. The free surfaces of the crack result in a overall increase of fuel pellet diameter. This effect can be modeled by applying a radial strain to the fuel pellet. This strain is similar to a volumetric strain, but only in the radial direction. A method for calculating this strain is the ESCORE relocation model [49] which is given as

$$\left(\frac{\Delta D}{D_o}\right)_{REL} = 0.80 Q \left(\frac{G_o}{D_o}\right) \left(0.005 Bu^{0.3} - 0.20 D_o + 0.3\right) \tag{8.81}$$

This relocation model is a function of power, as-fabricated pellet diameter, as-fabricated gap thickness, and burnup. The model is applicable between 8 and 22 kW/ft and to burnup levels between 0 and 11,500 MWd/MTU, and mean-diameter measurements were used in the correlation

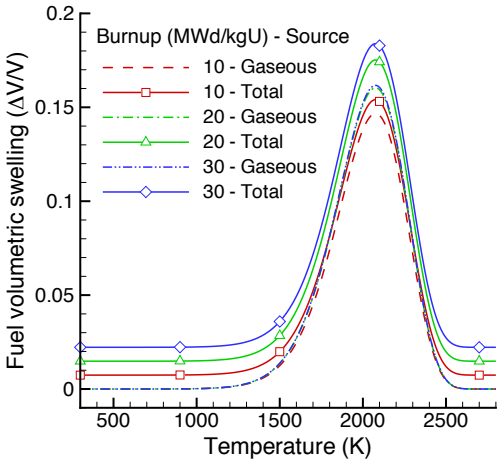

Figure 8.7: UO_2 gaseous and total swelling, as a function of temperature and burnup, based on the MATPRO [39] correlations.

development. The following is a list of variables definitions.

$\left(\frac{\Delta D}{D_o}\right)_{REL}$: Diametral strain due to relocation,

D_o : As-fabricated cold diameter of the pellet (in),

q' : Pellet average linear heating rate (kW/ft),

Bu : Pellet average fuel burnup (MWd/MTU), and

G_o : As-fabricated cold diametral gap (in)

$$Q : \begin{cases} 0 & \text{for } q' \leq q_1 \\ (q'-6)^{1/3} & \text{for } q_1 < q' \leq q_2 \\ (q'-10)/2 & \text{for } q' > q_2 \end{cases}$$

q_1 : 6 kW/ft

q_2 : 14 kW/ft

The fuel relocation strain is applied incrementally by calculating the relocation strain at the burnup for the current step and subtracting the relocation strain at the previous burnup. In other applications of this model, the addition of relocation strain is stopped when the gap is closed. In BISON, the relocation strain is stopped at a specified burnup.

Note that the pellet average linear heating rate q' has units of kW/ft in the empirical model. However, this quantity is passed into the model as a function with units of W/m. The conversion is handled inside the model.

It has been observed that the 6 kW/ft threshold for the initiation of relocation is well beyond

the level expected to cause cracking in the fuel. For this reason, a modified ESCORE model is available. For this model,

$$\left(\frac{\Delta D}{D_o}\right)_{REL} = q(0.8)(2)\left(\frac{G_o}{D_o}\right)\left(0.005Bu^{0.3} - 0.20D_o + 0.3\right)/q_2 \tag{8.82}$$

when q_1 is less than $q^{'}$ and q_1 is less than 6 kW/ft.

It is also possible to use the GAPCON model for relocation [50]. This model is given as

$$u^{rel} = (42b/(1+b) + 0.274q^{'} + 3)G_o/100 \tag{8.83}$$

where u^{rel} is the displacement due to relocation, $b = e^{(-4+Bu^{0.25})}$, $q^{'}$ is the linear heating rate (kW/m), Bu is burnup (MWd/MTU), and G_o is the as-fabricated cold gap.

8.8.8 Thermal and Irradiation Creep - UO_2 [creepUO2]

A model for combined secondary thermal creep and irradiation creep of UO_2 fuel is available, with the creep rate modeled as a function of time, temperature, effective stress, density, grain size, fission rate, and oxygen to metal ratio (O/M). The constitutive relation is taken from the MATPRO FCREEP material model [39] and given as

$$\dot{\varepsilon} = \frac{A_1 + A_2\dot{F}}{(A_3+D)G^2}\sigma e^{\left(\frac{-Q_1}{RT}\right)} + \frac{A_4}{(A_6+D)}\sigma^{4.5}e^{\left(\frac{-Q_2}{RT}\right)} + A_7\dot{F}\sigma e^{\left(\frac{-Q_3}{RT}\right)} \tag{8.84}$$

where $\dot{\varepsilon}$ is the creep rate (1/s), σ is the effective (Mises) stress (Pa), T is the temperature (K), D is the fuel density (percent of theoretical), G is the grain size (μm), $\dot{F}$ is the volumetric fission rate (fissions/m^3-s), Q_i are the activation energies (J/mol), R is the universal gas constant (8.3143 J/mol-K) and A_{1-7} are material constants given as $A_1 = 0.3919$, $A_2 = 1.3100x10^{-19}$, $A_3 = -87.7$, $A_4 = 2.0391x10^{-25}$, $A_6 = -90.5$, and $A_7 = 3.7226x10^{-35}$. The first term represents diffusional thermal creep and is applicable to low stress and low temperature conditions. The second term represents thermal dislocation or power-law creep and is applicable to high stress and high temperature conditions. Note that irradiation effects are included in both the first and third terms.

The activation energies for the thermal creep terms (Q_1 and Q_2) are strongly dependent upon the fuel oxygen to metal ratio x and, in MATPRO, are defined using the Arrhenius type relations

$$Q_1 = 74,829f(x) + 301,762 \tag{8.85}$$

$$Q_2 = 83,143f(x) + 469,191 \tag{8.86}$$

where the energies are given in J/mole and

$$f(x) = \frac{1}{e^{\left(\frac{-20}{log(x-2)} - 8\right)} + 1} \tag{8.87}$$

This function is plotted in Figure 8.8. The activation energy for the irradiation term (Q_3) is given in MATPRO as 21,759 J/mole.

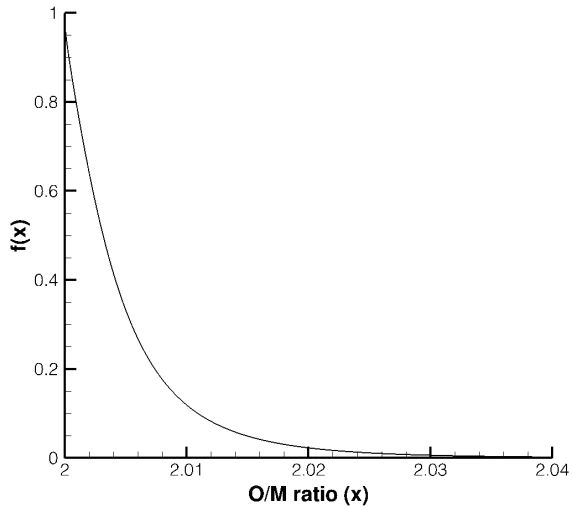

Figure 8.8: The function defining the dependence of the activation energies for thermal creep on the UO_2 oxygen to metal ratio.

In MATPRO, a transition stress is defined to govern the transition between the first (low stress) and second (high stress) regions. When the applied stress is larger than the transition stress, the applied stress is used in the power-law relation and the transition stress is used in the linear creep relation. When the applied stress is lower than the transition stress, the applied stress is used in the linear relation and the power-law contribution is zero. Mai et al. [51] investigated the MATPRO transition approach in comparison to experimental data and concluded that a better fit to the data could be achieved by simply ignoring the transition stress and applying both the low and high stress terms in all cases. This approach, termed here the Modified MATPRO model, has been adopted in BISON. The procedure outlined above for time-independent plasticity was used here to implement time-dependent plasticity (creep).

Young's modulus, Poisson's ratio and the coefficient of thermal expansion can each be specified in two ways. The values can be given directly, or the values can be computed using MATPRO correlations.

8.8.9 Stress-induced Densification - UO_2 `[HotPressingUO2]`

Creep or instantaneous plastic flow surrounding pores in ceramic UO2 fuel pellet under pressure can reduce pore volume, and as a consequence, reduce fuel porosity and increase fuel density. This is a densification mechanism of UO_2 fuel under compressive stresses, which contributes to fuel densification in addition to the irradiation induced densification. Such mechanical densification process is more pronounced at high temperatures with high creep rate or plastic deforma-

tions, and it is also referred to as hot-pressing.

The mathematical model of hot-pressing of ceramic UO_2 was described in a classical paper by Rashid [52]. By using an analogy of close-packed spherical shells in infinite media under hydrostatic compression, model on the stress-induced densification based on the mechanism of instantaneous plasticity and creep was derivied. This section describes the implementation of the hot-pressing model based on the mechanisms of creep and plasticity as follows. The new material class `[HotPressingUO2]` in the BISON code is inheritated from `[CreepUO2]` described in previous section.

- Creep
  For creep that follows power-law

$$\dot{\varepsilon} = A\sigma^n \tag{8.88}$$

  The tangential creep rate of porous media, with density ρ, at the pore surface is given as in Ref. [52].

$$\dot{\varepsilon}_t = \frac{A}{2}\left(\frac{3}{2n}\right)^n \left(\frac{1}{(0.74(1-\rho))^{1/n}-1}\right)^n P^n \tag{8.89}$$

  And, the volumetric creep rate is

$$\dot{\varepsilon}_V = 6\nu_0 A P^n \tag{8.90}$$

  Hot-pressing parameter ν_0 is defined as

$$\nu_0 = \frac{1}{4}\left(\frac{3}{2n}\right)^n \left(\frac{1}{(0.74(1-\rho))^{1/n}-1}\right)^n P^n \tag{8.91}$$

  Where
  P the hydrostatic pressure (Pa)
  n is the exponent in the power law creep equation
  A is the leading coefficient in the power law creep equation
  ρ is the fractional density (dimensionless)
  $\dot{\varepsilon}$ is the creep rate
  Subscript t and V represent tangential and volumetric components respectively.

  This material parameter ν_0 is used in the hot-pressing model for the volumetric creep of UO_2. The creep of UO_2 involves several mechanisms, and in their mathematical descriptions, different exponent n could be used for the different mechanisms. The volumetric creep strain implemented in BISON code is assumed to be the combination of all the creep strains together. From Eq. 8.91, the hot-pressing parameter depends on the fuel density. With the increase of fuel density, the parameter ν_0 would be reduced; when fractional density approaches 1.0, the parameter ν_0 approaches zero, and the densification would essentially be terminated, i.e., the volumetric creep strain rate in Eq. 8.90 becomes zero. A plot of the hot-pressing parameter versus initial density at different n is shown in Figure 8.9.

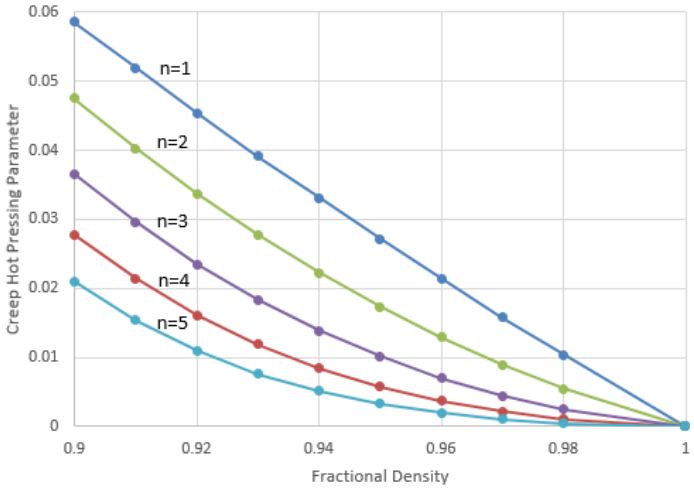

Figure 8.9: Hot-pressing parameter ν_0 versus fractional density

- Instantaneous Plasticity
  In Ref. [52], yield criterion of UO_2 is described in a modified Mohr-coulomb criterion. Eq. 8.92 through Eq. 8.95 summarize what have been described in Ref. [52].

$$f = J_2 + \alpha J_1^2 - K = 0 \tag{8.92}$$

The incremental plastic strain is given as:

$$\Delta\varepsilon_{ij}^P = \lambda(S_{ij} + 2\alpha J_1 \delta_{ij}) \tag{8.93}$$

where
$J_1 = \sigma_{ii}$
$J_2 = \frac{1}{2} S_{ij} S_{ij}$
$S_{ij} = \sigma_{ij} - \frac{1}{3} J_1 \delta_{ij}, i \neq j$
δ_{ij} is the Kcronecker delta, zero for $i \neq j$ and unity for $i = j$

The volumetric strain increment is

$$\Delta\varepsilon_{ii}^P = 6\lambda\alpha J_1 \tag{8.94}$$

α defines a material parameter that relates to the yield stress of 100% UO_2 density.

$$\alpha = \left(\frac{Y(\rho_0)/Y_s}{2/\sqrt{3}\ln(0.74/(1-\rho))} \right)^2 \tag{8.95}$$

Where $Y(\rho_0)$ is the yield stress of UO_2 at initial density ρ_0, and Y_s is the yield stress at 100% UO_2 density. The determination of α needs experimental data on the yield stress of UO_2 with different porosities, which is scarce in the literatures. Instead, an approximation is made in the code by using a constant ratio of $Y(\rho_0)/Y_s$=0.95. The resultant equation of α in the BISON code is

$$\alpha = \frac{0.0752}{(\ln(0.74/(1-\rho))^2} \tag{8.96}$$

λ however is not defined in Ref. [52]. To implement the model in BISON, a new flow rule is used. The yield criterion is formulated as:

$$f = \sqrt{J_2 + \alpha J_1^2} = K \tag{8.97}$$

The effective stress is derived as:

$$\sigma_{eff} = \sqrt{3(J_2 + \alpha J_1^2)} \tag{8.98}$$

The new flow rule used in BISON is provided in following equations.

$$\Delta\varepsilon_{ij}^P = \frac{3}{2}\frac{S_{ij}}{\sigma_{eff}}\Delta\varepsilon^P, i \neq j \tag{8.99}$$

$$\Delta\varepsilon_V^P = 3\sqrt{\frac{3\alpha}{2}}\frac{J_1}{\sigma_{eff}}\Delta\varepsilon^P \tag{8.100}$$

- Yield Stress Model
  The hot-pressing or mechanical densification under instantaneous plastic flow depends on the yield strength of UO_2, which is currently not available in BISON code. A linear hardening material model is used for modeling the yield stress of UO_2. The yield stress for the linear hardening material is

$$\sigma_{eff} = \sigma_y + H\Delta\varepsilon^P \tag{8.101}$$

  Where
  σ_y is the initial yield stress
  σ_{eff} is the new yield stress (effective stress)
  $\Delta\varepsilon^P$ is the effective incremental plastic strain
  H is the hardening modulus
  The incremental effective plastic strain and new yield stress are computed in BISON using radial return method.

8.8.10 Thermal and Irradiation Creep - MOX `[CreepMOX]`

The creep model for MOX is a combined model from MATPRO [39] and Guerin [53]. Experimental data used by MATPRO for MOX cover indeed a range of temperature above 1500 K, so that the proposed model accounts essentially for thermal creep. In [53], Guerin provides an

semi-empirical law for MOX irradiation creep, hired from Milet's experiments, whose results have been published in [54]. MATPRO provides a time-dependant multiplier which allows to account for primary and secondary creep. Thus the creep model for MOX implemented in BISON is given by:

$$\dot{\varepsilon}_{cr} = (1 + a\exp(-b \cdot t)) \cdot \dot{\varepsilon}_s \tag{8.102}$$

with

$$\dot{\varepsilon}_s = \frac{B_1 + B_2\dot{F}}{G^2}\sigma\exp\left(-\frac{Q_3}{T} + B_7(1-D) + B_4C\right) \tag{8.103}$$

$$+ B_5\sigma^{4.5}\exp\left(-\frac{-Q_4}{T} + B_7(1-D) + B_4C\right) \tag{8.104}$$

$$+ A\sigma\dot{F} \tag{8.105}$$

where

$$\begin{aligned}
T &= \text{ Temperature (K)} \\
\sigma &= \text{ Effective stress (Pa)} \\
\dot{F} &= \text{ Fission rate } \mathrm{m}^{-3} \cdot \mathrm{s}^{-1} \\
G &= \text{ grain size } (\mu\mathrm{m}) \\
C &= \mathrm{PuO_2} \text{ concentration (wt.\%)}
\end{aligned}$$

and in SI

$$\begin{aligned}
a &= 2.5 \\
b &= 1.40 \cdot 10^{-6} \\
A &= 4.8\dot{1}0^{-36} \\
B_1 &= 0.1007 \\
B_2 &= 7.57 \cdot 10^{-20} \\
B_3 &= 33.3 \\
B_4 &= 0.014 \\
B_5 &= 6.4691 \cdot 10^{-25} \\
B_7 &= 10.3 \\
Q_3 &= 55354.0 \\
Q_4 &= 70451.0
\end{aligned}$$

Figure 8.10 shows a comparison between creep models implemented in BISON for UO_2 and MOX.

The time origin for primary creep is updated in BISON when the stress rate is greater than a value specified by the user. Two successive time origins cannot be closer than 5 times the characteristic time of transient creep.

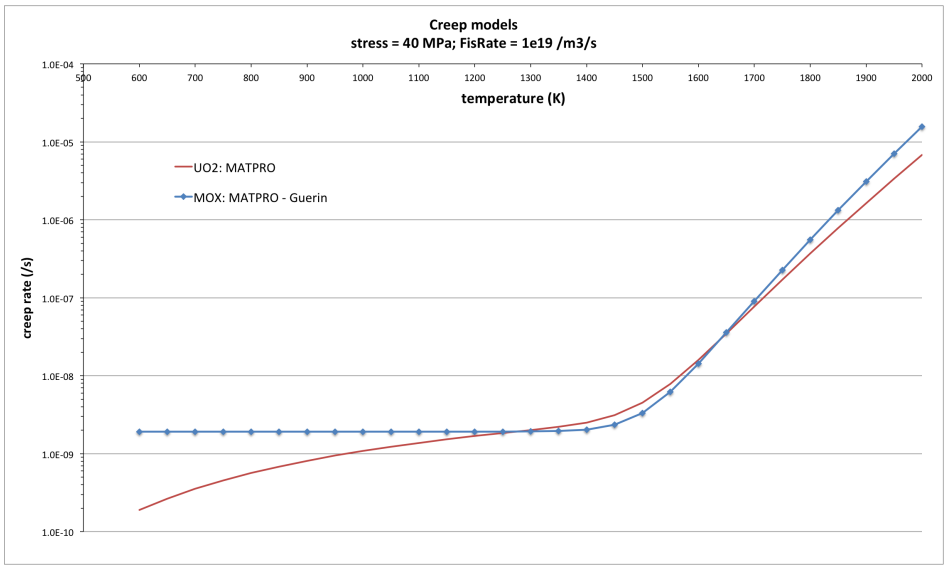

Figure 8.10: Comparison of creep rates for MOX and UO_2. The creep rate for MOX is higher than that of UO_2.

8.8.11 Steady State Thermal and Irradiation Creep - Fast MOX `[CreepFastMOXModel]`

A steady-state thermal and irradiation creep model for fast MOX comes from an article by J. L. Routbort [55], described by the following equation.

$$\dot{\varepsilon}_{thermal+irradiation} = \frac{A}{G^2}\sigma \exp\left(-\frac{Q_1}{RT}\right) + B\sigma^{4.4}\exp\left(-\frac{Q_2}{RT}\right) \tag{8.106}$$

$$+ C\sigma\dot{F} \tag{8.107}$$

where

$R =$ Universal gas constant 1.987 (cal/mol-K)
$T =$ Temperature (K)
$\sigma =$ Effective stress (Pa)
$\dot{F} =$ Fission rate $\mathrm{m}^{-3} \cdot \mathrm{s}^{-1}$
$G =$ grain size (μm)

where the following are creep coefficients and activation energies

$$A = 3.23 \cdot 10^{9}$$
$$B = 3.24 \cdot 10^{6}$$
$$C = 1.78 \cdot 10^{-26}$$
$$Q_1 = 92500 \text{ (cal/mol)}$$
$$Q_2 = 136800 \text{ (cal/mol)}$$

8.8.12 Mechanical Properties - Fast minor actinide MOX `[MechMAMOX]`

MechMAMOX calculates the oxygen to metal ratio and temperature dependent thermal expansion of minor actinide (MA) doped mixed oxide fuel (MOX). The MA-MOX correlations used in this material model were developed by M. Kato et al. [56], with 300 K as the reference temperature. It is important to note that the correlation as it is currently coded in BISON is for $Pu_{0.3}$. The equations can be seen below.

$$CTE = \left(\frac{\Delta L}{L_o(T - 300)} \right) [K^{-1}] \tag{8.108}$$

$$\left(\frac{\Delta L}{L_o} \right) = a_o + a_1 T + a_2 T^2 + a_3 T^3 \tag{8.109}$$

Where T is temperature and the variables: a_o, a_1, a_2 and a_3 are coefficients based on the oxygen to metal ratio.

8.8.13 Smeared Cracking

In ceramic fuel such as UO_2, a significant temperature gradient develops from the fuel center to the radial edge. This gradient appears early and is strong enough to induce cracking in the fuel due to the accompanying stress. The cracks reduce the stress in the fuel and increase the effective fuel volume (decrease the gap size).

A smeared cracking model in BISON may be invoked to account for this cracking. A smeared cracking model adjusts the elastic constants at material points as opposed to introducing topographic changes to the mesh, as would be the case with a discrete cracking model.

When the smeared cracking model is active, principal stresses are compared to a critical stress. If the material stress exceeds the critical stress, the material point is considered cracked in that direction, and the stress is reduced to zero. From that point on, the material point will have no strength unless the strain becomes compressive.

The orientation of the principal coordinate system is determined from the eigenvectors of the elastic strain tensor. However, once a crack direction is determined, that direction remains fixed and further cracks are considered in directions perpendicular to the original crack direction. Note that for axisymmetric problems, one crack direction is known *a priori*. The theta or out-of-plane direction is not coupled to the r and z directions (i.e., no $r\theta$ or $z\theta$ shear strain/stress exists) and is therefore a known or principal direction.

If we store a scalar value, c_i, for each of the three possible crack directions at a material point, these in combination with the principal directions (eigenvectors or rotation tensor) provide a convenient way to eliminate stress in cracked directions. A value of 1 for c_i indicates that the material point has not cracked in that direction. A value very close to zero (not zero for numerical reasons) indicates that cracking has occurred.

We define a cracking tensor in the cracked orientation as $\mathbf{c}$:

$$\mathbf{c} = \begin{bmatrix} c_1 & & \\ & c_2 & \\ & & c_3 \end{bmatrix}. \tag{8.110}$$

The rotation tensor $\mathbf{R}$ is defined in terms of the eigenvectors e_i:

$$\mathbf{R} = \begin{bmatrix} e_1 & e_2 & e_3 \end{bmatrix}. \tag{8.111}$$

This leads to a transformation operator $\mathbf{T}$:

$$\mathbf{T} = \mathbf{R}\mathbf{c}\mathbf{R}^T. \tag{8.112}$$

$\mathbf{T}$ is useful for transforming uncracked tensors in the global frame to cracked tensors in the same frame. For example, the cracked stress σ_{cg} in terms of the stress σ_g is (subscript c indicates cracked, l local frame, and g global frame):

$$\sigma_{cg} = \mathbf{T}\sigma_g\mathbf{T}^T \tag{8.113}$$

$$= \mathbf{R}\mathbf{c}\mathbf{R}^T\sigma_g\mathbf{R}\mathbf{c}\mathbf{R}^T \tag{8.114}$$

$$= \mathbf{R}\mathbf{c}\sigma_l\mathbf{c}\mathbf{R}^T \tag{8.115}$$

$$= \mathbf{R}\sigma_{cl}\mathbf{R}^T. \tag{8.116}$$

When many material points have multiple cracks, the solution becomes difficult to obtain numerically. For this reason, controls are available to limit the number and direction of cracks that are allowed.

8.8.14 Isotropic Cracking

The idea behind the BISON isotropic cracking model is to provide a description of cracked fuel in an isotropic mechanical framework. In particular, it is assumed that

- The cracking of the fuel occurs in the elastic regime.
- The crack length spans the full fuel dimension in the considered direction.
- The description of the cracked material is not dependent on the particular crack-pattern but only on the number of cracks.
- The principal strains are conserved.

Under these assumptions, the elastic constants (i.e., Young modulus E and Poisson ratio ν) are scaled depending on the number of cracks n. The calculated stresses are scaled accordingly and isotropically. The model allows for multiple fuel cracking, and an empirical correlation for the number of cracks as function of the rod average linear heat rate is developed.

The basis of the herein described model are the constitutive equations describing the elastic behavior in terms of stresses σ and strains ε of a non-cracked material (expressed in terms of principal directions of cylindric coordinates r, θ, z), namely

$$\begin{aligned} E\varepsilon_r &= \sigma_r - \nu(\sigma_\theta + \sigma_z) \\ E\varepsilon_\theta &= \sigma_\theta - \nu(\sigma_r + \sigma_z) \\ E\varepsilon_z &= \sigma_z - \nu(\sigma_r + \sigma_\theta) \end{aligned} \tag{8.117}$$

When any of the principal stresses reaches the ultimate stress, the fuel cracks along the direction perpendicular to that stress principal direction. For instance, when a crack occurs perpendicular to the circumferential direction, the corresponding stress component σ_θ vanishes. Thus, the elastic behaviour of the cracked fuel is described by

$$\begin{aligned} \sigma_\theta &= 0 \\ E\varepsilon_r &= \sigma_r - \nu\sigma_z \\ E\varepsilon_\theta &= -\nu(\sigma_r + \sigma_z) \\ E\varepsilon_z &= \sigma_z - \nu\sigma_r \end{aligned} \tag{8.118}$$

The comparison of Eqs. 8.118 with Eqs. 8.117 points out the anisotropy introduced by the presence of the crack. In order to represent the cracked material as isotropic, it is assumed that the elastic constitutive model for an isotropic material holds for the cracked material

$$\begin{aligned} E_i\varepsilon_r &= \sigma_{r,i} - \nu_i(\sigma_{\theta,i} + \sigma_{z,i}) \\ E_i\varepsilon_\theta &= \sigma_{\theta,i} - \nu_i(\sigma_{r,i} + \sigma_{z,i}) \\ E_i\varepsilon_z &= \sigma_{z,i} - \nu_i(\sigma_{r,i} + \sigma_{\theta,i}) \end{aligned} \tag{8.119}$$

Compared to Eqs. 8.118, the representation of Eqs. 8.119 conserves the principal strains and scales the elastic constants to the values E_i and ν_i to allow for an isotropic description of the stresses σ_r, σ_θ, σ_z.

In order to determine the scaled elastic constants E_i and ν_i the square deviation of the scaled stresses is defined (Eqs. 8.119) with respect to the stresses in the cracked material (Eqs. 8.118), namely

$$D = (\sigma_{r,i} - \sigma_r)^2 + (\sigma_{\theta,i} - \sigma_\theta)^2 + (\sigma_{z,i} - \sigma_z)^2 \tag{8.120}$$

which is a function of the principal strains ε_r, ε_θ, ε_z. It can be demonstrated that averaging over any strain range symmetric with respect to 0 and minimizing D yields

$$E_i = \frac{2}{3}\frac{2-\nu}{2+\nu}\frac{1}{1-\nu}E = f(\nu)E \tag{8.121}$$

$$\nu_i = \frac{\nu}{2+\nu} \tag{8.122}$$

These equations are identical to those derived by Jankus and Weeks [57]. Note that Eqs. 8.121,8.122 are independent of the principal direction considered for cracking.

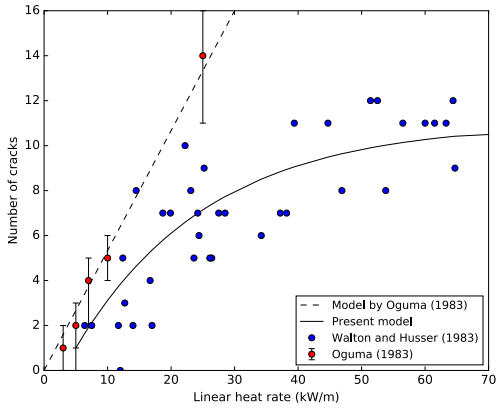

Figure 8.11: Number of cracks as a function of the rod average linear heat rate. Experimental data according to Oguma [58] and Walton and Husser [59]

The model allows for multiple cracks in the fuel by applying iteratively Eqs. 8.121,8.122. For n cracks, the elastic constants become

$$E_i(n) = [f(\nu)]^n E \tag{8.123}$$

$$\nu_i(n) = \frac{\nu}{2^n + (2^n - 1)\nu} \tag{8.124}$$

The number of cracks n is considered as a function of the rod average linear heat rate LHR. In particular, a correlation is developed based on the data reported by Oguma [58] and Walton and Husser [59]. No dependencies on burnup or on power operation history (i.e., cycling) are considered, in view of lack of data.

The resulting correlation for the number of cracks is

$$\begin{aligned} n &= 0 && \text{if } LHR < LHR_0 \\ n &= n_0 + (n_\infty - n_0)\left[1 - \exp\left(-\tfrac{LHR - LHR_0}{\tau}\right)\right] && \text{if } LHR \geq LHR_0 \end{aligned} \tag{8.125}$$

in which $LHR_0 = 1$ is the linear heat rate required to trigger the first $n_0 = 1$ crack. The parameters $n_\infty = 12$ and $\tau = 21$ kW/m have been determined by fitting [58, 59].

Figure 8.11 reports the correlation (Eq. 8.125) together with the data used to derive it. The correlation proposed by Oguma [58] is reported for comparison. The description of crack healing is currently not considered in the cracking model.

As an example, the application of the isotropic cracking model to a 2D axisymmetric model of a single UO_2 fuel pellet under typical PWR irradiation conditions is presented. The calculated principal stresses (i.e., in the considered coordinate system, radial, circumferential and axial stress), hydrostatic stress and Von Mises stress are shown in Fig. 8.12. Both isotropic cracking and creep models are activated. Results refer to irradiation times of 3 h (solid line) and after 3 years (dashed line) of irradiation, respectively. These results are in line with the expected stress values in a cracked material.

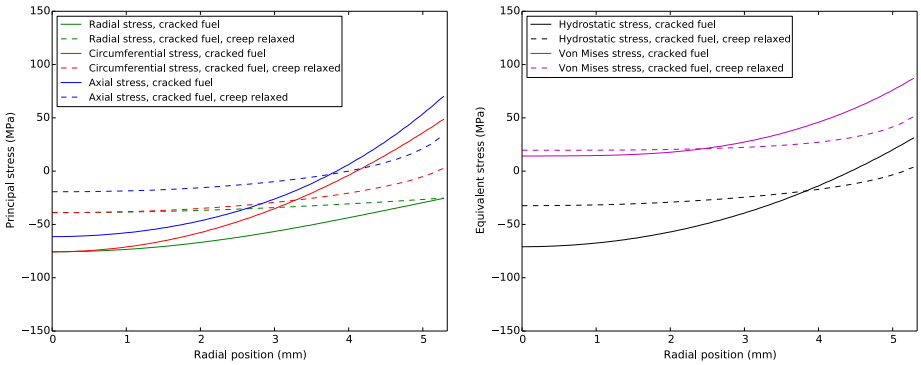

Figure 8.12: Calculated radial profiles of principal (left) and equivalent (right) stresses for a single-pellet analysis. Both visco-elastic (creep) constitutive model and isotropic cracking model are applied in the calculation.

8.8.15 Grain Growth

When a polycrystalline material is subject to high temperatures, larger grains tend to grow at the expense of the smaller ones. As a consequence, the latter gradually disappear, thus reducing the total number of grains per unit volume and increasing the average grain size. This phenomenon is known as grain growth. The granular structure of the fuel affects physical processes such as fission gas behavior (see Section 10).

A simple empirical model [60] is implemented in BISON for calculating grain growth in UO_2 fuel. According to this model, the kinetics of grain growth is described by the equation:

$$\frac{dD}{dt} = k\left(\frac{1}{D} - \frac{1}{D_m}\right) \tag{8.126}$$

where D (μm) is the 2-dimensional (linear intercept) average grain diameter, t (h) the time, k (μm^2/h) the rate constant, which is $5.24 \cdot 10^7\, exp(-2.67 \cdot 10^5/(RT))$ for R = 8.314 J/(mol·K), and D_m (μm) is the limiting grain size. The latter is a function of the temperature such that

$$D_m = 2.23 \cdot 10^3\, exp(-7620/T) \tag{8.127}$$

To obtain the 3-dimensional grain diameter, D is multiplied by a factor of 1.56 [61].

8.9 Uranium Metal

8.9.1 Thermal Properties `[ThermalU]`

Thermal conductivity k (W/m-K) of uranium metal is from [62], with F_P as a porosity correction given in 9.1, where it is assumed that $\beta = 2.5$:

$$k = 16.170 \times F_P, \qquad T \leq 255.4 \text{ K} \tag{8.128}$$

$$k = (5.907 \times 10^{-6} T^2 + 1.591 \times 10^{-2} T + 11.712) \times F_P, \qquad T \leq 1173.2 \text{ K} \tag{8.129}$$

$$k = 38.508 \times F_P, \qquad T > 1173.2 \text{ K} \tag{8.130}$$

Specific heat C_p (J/mol-K) of U metal is from [62]:

$$C_p = 27.699, \qquad T \leq 298 \text{ K} \tag{8.131}$$

$$C_p = (2.370 \times 10^{-5} T^2 + 2.132 \times 10^{-3} T + 24.959), \qquad T \leq 942 \text{ K} \tag{8.132}$$

$$C_p = 42.928, \qquad T \leq 1049 \text{ K} \tag{8.133}$$

$$C_p = 38.284, \qquad T \leq 1408 \text{ K} \tag{8.134}$$

$$C_p = 48.668, \qquad T > 1408 \text{ K} \tag{8.135}$$

The specific heat is converted to J/kg-K by dividing by 0.238 kg/mol.

8.10 U-Pu-Zr

Metallic fuels such as U-Zr and U-Pu-Zr alloys are used as fuel in fast breeder reactors. The following sections present the equations used to calculate the porosity, thermal properties and thermal and irradiation creep of these alloys.

8.10.1 Thermal Properties `[ThermalUPuZr]`

The material model `ThermalUPuZr` calculates the thermal conductivity and heat capacity of U-xPu-yZr, where x and y refers to the weight fraction of Pu and Zr respectively. The material model accepts either constant values for the weight fractions x and y, or can be coupled to molar fractions that in turn can be used by other kernels or material models. If atom fractions are provided, `ThermalUPuZr` converts them into weight fractions by:

$$w_U = (1 - x - y) A_U / M_A, \tag{8.136}$$

$$w_{Pu} = x A_{Pu} / M_A, \tag{8.137}$$

$$w_{Zr} = y A_{Zr} / M_A, \tag{8.138}$$

$$M_A = (1 - x - y) A_U + x A_{Pu} + y A_{Zr}, \tag{8.139}$$

where A is the atomic weight of each element in kg/mol, and M_A is the average atomic mass of the fuel mixture in kg/mol.

There are several different models available for calculation of thermal conductivity and heat capacity for unirradiated fuel as described in the following sections.

8.10.1.1 Billone thermal conductivity model

A generic model for the thermal conductivity of U, U-Zr and U-Pu-Zr alloys is given by Billone et al. [63]. The thermal conductivity of unirradiated fuel in units of W/m-K is given by

$$k_o = A + BT + CT^2, \tag{8.140}$$

where T is the temperature in Kelvin and A, B, and C are temperature coefficients. These coefficients are given by,

$$A = 17.5 \cdot \left(\frac{1 - 2.23W_z}{1 + 1.61W_z} - 2.62W_p \right), \tag{8.141}$$

$$B = 1.54 \times 10^{-2} \cdot \left(\frac{1 + 0.061W_z}{1 + 1.61W_z} + 0.90W_p \right), \tag{8.142}$$

$$C = 9.38 \times 10^{-6} \cdot (1 - 2.70W_p), \tag{8.143}$$

where W_p and W_z are the weight fractions of plutonium and zirconium respectively in the fuel mixture.

8.10.1.2 Galloway thermal conductivity model

A model for the thermal conductivity of U-Pu-Zr fuel with any concentration of constituents is given by [64]. Data used to develop the empirical model for thermal conductivity of U-Pu-Zr and U-Zr fresh fuels are obtained from [65, 62, 66, 67, 68]. The basis for the model is derived from the formulation given by [66] with coefficient adjustments to minimize the standard deviation of error between data and the current empirical model. The model consists of calculation of the thermal conductivity of each constituent, the thermal conductivity of the binaries U-Zr and Pu-Zr, and finally the thermal conductivity of the ternary U-Pu-Zr.

The thermal conductivities in W/m-K for each constituent is calculated by,

$$k_U = 21.73 + 1.591 \times 10^{-2} T + 5.907 \times 10^{-6} T^2, \tag{8.144}$$

$$k_{Pu} = -15.529 + 8.512 \times 10^{-2} T - 4.301 \times 10^{-5} T^2, \tag{8.145}$$

$$k_{Zr} = 8.853 + 7.082 \times 10^{-3} T + 2.533 \times 10^{-6} T^2 + 2.992 \times 10^{3} T^{-1}, \tag{8.146}$$

where T is temperature in K. The binary thermal conductivities are calculated by,

$$k_{U-Zr} = (1 - \sqrt{1 - f_{Zr}}) k_{Zr} + \sqrt{1 - f_{Zr}} (f_{Zr} k_{c,U-Zr} + (1 - f_{Zr}) k_U), \tag{8.147}$$

$$k_{Pu-Zr} = (1 - \sqrt{1 - f_{Pu}}) k_{Pu} + \sqrt{1 - f_{Pu}} k_{c,Pu-Zr}, \tag{8.148}$$

where the adjusted weight fractions for the binary formulations are given as,

$$f_{Zr} = \frac{w_{Zr}}{w_{Zr} + w_U}, \tag{8.149}$$

$$f_{Pu} = \frac{w_{Pu}}{w_{Pu} + w_{Zr}}. \tag{8.150}$$

The correction terms for the binaries are given as,

$$k_{c,U-Zr} = -102 + 200.1 f_{Zr} - 109.2 f_{Zr}^2 + 9.435 \times 10^{-3} T + 3.459 \times 10^{-5} T^2 - 0.02093 f_{Zr} T, \tag{8.151}$$

$$k_{c,Pu-Zr} = 29.469 - 118.811 f_{Pu} + 88.893 f_{Pu}^2 + 0.0117 T + 1.922 \times 10^{-5} T^2 - 0.00716 f_{Pu} T, \tag{8.152}$$

$$\tag{8.153}$$

Finally, the ternary thermal conductivity is calculated by,

$$k_{U-Pu-Zr} = \left(\frac{w_U}{w_U + w_{Pu}}\right)^2 k_{U-Zr} + \left(\frac{w_{Pu}}{w_U + w_{Pu}}\right)^2 k_{Pu-Zr} + 1.564 \frac{w_U w_{Pu}}{(w_U + w_{Pu})^2} \left(\frac{k_{U-Zr} k_{Pu-Zr}}{k_{U-Zr} + k_{Pu-Zr}}\right). \tag{8.154}$$

This empirical model gives an average error of -0.02 W/m-K with a standard deviation of 1.46 W/m-K.

8.10.1.3 Ternary thermal conductivity model: Kim

The Ternary thermal conductivity model is very similar to the model used by Galloway in the previous section, albeit with different coefficients and different formulation of the ternary thermal conductivity. The original formulation comes from [69].

The thermal conductivities in W/m-K for each constituent is calculated using Equations 8.145 and 8.146, with the forumlation for plutonium as,

$$k_{Pu} = -4.987 + 4.408 \times 10^{-2} T - 1.566 \times 10^{-5} T^2, \tag{8.155}$$

where T is temperature in K. The U-Zr binary thermal conductivitiy is calculated by:

$$k_{U-Zr} = (1 - \sqrt{1 - f_{Zr}}) k_{Zr} + \sqrt{1 - f_{Zr}} (f_{Zr} k_{c,U-Zr} + (1 - f_{Zr}) k_U), \tag{8.156}$$

where the adjusted weight fractions for the binary formulations are given as:

$$f_{Zr} = \frac{w_{Zr}}{w_{Zr} + w_U} \tag{8.157}$$

The correction terms for the U-Zr binary are given as,

$$k_{c,U-Zr} = -102 + 200.1 f_{Zr} - 109.2 f_{Zr}^2 + 9.435 \times 10^{-3} T + 3.459 \times 10^{-5} T^2 - 0.02093 f_{Zr} T \tag{8.158}$$

The thermal conductivity of the ternary fuel is given as,

$$k_{U-Pu-Zr} = (1 - \sqrt{1 - w_{pu}}) k_{Pu} + \sqrt{1 - w_{Pu}} [(1 - w_{Pu}) k_{U-Zr} + w_{Pu} k_{c,Pu}], \tag{8.159}$$

where w_{Pu} is the weight fraction of plutonium in the fuel and the plutonium thermal conductivity correction is given by,

$$k_{c,Pu} = -61.915 - 53.456 w_{Pu} + 362.452 w_{Pu}^2 + 0.1319 T - 7.851 \times 10^{-5} T^2 - 0.0115 w_{Pu} T. \tag{8.160}$$

8.10.1.4 Ternary thermal conductivity model: LANL

Recent work has been applied to extend Kim's model to more data, resulting in new coefficients [70]. These coefficients are also available as a separate model, designated `LANL`:

$$k_U = 21.76 + 1.665 \times 10^{-2} T + 5.167 \times 10^{-6} T^2, \tag{8.161}$$

$$k_{Pu} = -8.162 + 4.841 \times 10^{-2} T - 1.614 \times 10^{-5} T^2, \tag{8.162}$$

$$\begin{aligned} k_{c,U-Zr} = &-97.0 + 177.9 f_{Zr} - 95.94 f_{Zr}^2 + 8.351 \times 10^{-3} T \\ &+ 2.931 \times 10^{-5} T^2 - 5.694 \times 10^{-3} f_{Zr} T, \end{aligned} \tag{8.163}$$

$$k_{c,Pu} = -135.8 - 29.89 w_{Pu} + 351.9 w_{Pu}^2 + 0.3571 - 1.186 \times 10^{-4} T^2 - 0.961 w_{Pu} T. \tag{8.164}$$

Although only slightly different, when the updated coefficients are plugged into the remainder of the ternary model, the calculation of thermal conductivity results in a standard deviation of less than 1 W/m-K.

8.10.1.5 Porosity correction

When taking into account irradiation effects through the introduction and growth of porosity, the thermal conductivity becomes,

$$k = f_p k_o, \tag{8.165}$$

where,

$$f_p = \frac{1-p}{1+\beta p}. \tag{8.166}$$

The porosity p is determined by `[PorosityMetalAux]` and the constant β is typically taken as 2.5 for conservatism as recommended by Billone et al. [63].

8.10.1.6 Karahan Heat Capacity

The specific heat capacity of U-Pu-Zr alloys are dependent upon the phase ($\alpha+\delta$, $\beta+\gamma$ or γ) as per Karahan [46] where the transition temperatures are taken from Savage [71], as $T_1 = 600\ ^\circ C$ and $T_2 = 650\ ^\circ C$.

For the $\alpha+\delta$ phase:

$$c_{p1} = 26.58 + \frac{0.027}{M_A} T. \tag{8.167}$$

For the γ phase:

$$c_{p2} = 15.84 + \frac{0.026}{M_A} T. \tag{8.168}$$

For the $\beta+\gamma$ transition phase, interpolation has been performed such that,

$$c_p = \frac{c_{p2} - c_{p1}}{T_2 - T_1} (T - T_1) + c_{p1}. \tag{8.169}$$

In the above equations for specific heat capacity T is the temperature in Celsius and M_A is the average atomic mass of the fuel mixture in kg.

It is worth noting that this model presented by Karahan [46] but fails to divide the leading constant term by M_A, leading to miscalculation of the original data from [71].

8.10.1.7 Savage Heat Capacity

The correlation for heat capacity from Savage is split into the low temperature $\alpha+\delta$ region, and the high temperature γ region:

$$C_p^{\alpha+\delta}(T) = 6.36 + 0.00636 * T, \qquad \text{for } 25^\circ\text{ C} < T < 600^\circ\text{ C}, \tag{8.170}$$

$$C_p^{\gamma}(T) = 3.79 + 0.00623 * T, \qquad \text{for } T > 650^\circ\text{ C}, \tag{8.171}$$

where T is temperature in °C, and C_p is given in cal/mol-°C. A simple linear interpolation is used for the $\beta+\gamma$ region:

$$C_p^{\beta+\gamma}(T) = \left(\frac{C_p^{\gamma}(T_{high}) - C_p^{\alpha+\delta}(T_{low})}{T_{high} - T_{low}} \right) (T - T_{low}) + C_p^{\alpha+\delta}(T_{low}), \tag{8.172}$$

where T_{low} and T_{high} are the transition temperature 600° C and 650° C respectively.

Lastly, C_p is converted from cal/(mol-°C) to J/(kg-K) by multipling Equations 8.170, 8.171, or 8.172 by 4.184 [J/cal] and 0.205 [kg/mol]. It is important to note that the kg to mol conversion is kept constant, as it applies directly to the data captured by Savage. Changing the conversion factor will result in a dependency on the concentrations of Pu and Zr in the fuel that is not based on data, as is the case with the Karahan model described in Section 8.10.1.6

8.10.2 Thermal and Irradiation Creep `[CreepUPuZr]`

A model for combined secondary thermal creep and irradiation creep for U-Pu-Zr fast reactor fuel is available, with the creep rate modeled as a function of time, fuel porosity, effective stress, and fission rate. The constitutive relation is taken from Kutty et al. [72] and is given as

$$\dot{\varepsilon} = A_1 \left(1 + 7.9p + 470p^2\right) e^{\left(\frac{-Q_1}{RT}\right)} \sigma + A_2 \left(1 - p^{0.67}\right)^{-4.5} e^{\left(\frac{-Q_2}{RT}\right)} \sigma^{4.5} + A_3 \dot{F} \sigma \tag{8.173}$$

where $\dot{\varepsilon}$ is the creep rate (1/s), σ is the effective (Mises) stress (MPa), T is the temperature (K), p is the porosity, $\dot{F}$ is the volumetric fission rate (fissions/cm^3-s), Q_i are the activation energies (cal/mol), R is the universial gas constant (1.987 cal/mol-K) and A_{1-3} are material constants given as $A_1 = 5 \times 10^3$, $A_2 = 6$, and $A_3 = 7.7 \times 10^{-23}$. The first term represents diffusional thermal creep and is applicable to low stress and low temperature conditions. The second term represents thermal dislocation or power-law creep and is applicable to high stress and high temperature conditions. The third term represents the irradiation creep as it depends upon the fission rate. The activation energies for the thermal creep terms (Q_1 and Q_2) are given as $Q_1 = Q_2 = 52000$ cal/mol.

These U and Pu alloys have a phase change temperature of 923.15 K. Above this temperature, the creep rate equation changes to

$$\dot{\varepsilon} = A_4 \left(1 - p^{0.67}\right)^{-3} e^{\left(\frac{-Q_3}{RT}\right)} \sigma^3 + A_3 \dot{F} \sigma \tag{8.174}$$

where A_4 is 8.0×10^{-2} and Q_3 is 28500 cal/mol.

In addition to the thermal and irradiation creep, the negative strain component due to the compression of open pores [24] is also calculated in the `CreepUPuZr` model. The model for open pore compression strain is

$$\left(\frac{\Delta V}{V_0}\right)_{opc} = \Delta\varepsilon^{opc-} = 9\alpha_c \left(\sigma_r + \sigma_\theta + \sigma_z + 3P_p\right) \left(\frac{\Delta\varepsilon_{eq}^{creep}}{\sigma_{eq}}\right) \tag{8.175}$$

where $\Delta\varepsilon_{eq}$ is current increment of the creep strain, σ_{eq} is a modified equivalent stress measure, and α_c is the open pore compressibility factor. The modified equivalent scalar stress includes both the classical von Mises stress and the stress applied to the inside of the open pores; the plenum pressure is used as the internal pressure of the open pores [73].

$$\sigma_{eq} = \sqrt{\left(\sigma_{vonMises}\right)^2 + 3\alpha \left(\sigma_r + \sigma_\theta + \sigma_z + 3P_p\right)^2} \tag{8.176}$$

The modified equivalent stress measure is used only in Equation 8.175; the classical von Mises stress measure is used in the creep calculations, Equations 8.173 and 8.174.

The open pore compressibility factor is a function of the swelling strains due to interconnected bubbles and tearing [74]. At present this factor is defined as a step-function of porosity level in the metal fuel:

$$\alpha_c = \begin{cases} 0 & \text{if porosity } < 24\% \\ \frac{1}{6} & \text{if porosity } \geq 24\% \end{cases}$$

The open pore compression strain is a component of the isotropic volumetric swelling strain increment, along with gaseous swelling, Equation 8.180, and solid swelling, Equation 8.182.

8.10.3 Isotropic Volumetric Swelling `[VSwellingUPuZr]`

8.10.3.1 Gaseous Swelling

A mechanistic fuel swelling model for U-Pu-Zr systems was developed. The derivation below is originally presented in [3]. First assume that the fission gas generated in the fuel instantly forms fission gas bubbles having diameter of 5 μm. The mechanical force balance on an equilibrium bubble can be experessed as follows [75]:

$$p = \frac{2\gamma}{r_b} - \sigma_h + \sigma_{cr} \tag{8.177}$$

where p is the pressure of the fission gas in a bubble, γ is the surface tension of the fuel, r_b is the fission gas bubble size, σ_h is the hydrostatic stress in the fuel, and σ_{cr} is the creep strength stress of the fuel. The gas pressure in the bubble is governed by the ideal gas law:

$$pV = \nu RT \tag{8.178}$$

where p, V, ν, R, T, are the pressure, volume, amount, universal gas constant, and temperature of the fission gas, respectively. By rearranging the ideal gas law to calculated volume of the fission gas and substituting the mechanical force balance equation, the following is obtained for the volume of the fission gas:

$$V = \frac{\nu RT}{\frac{2\gamma}{r_b} - \sigma_h + \sigma_{cr}}. \tag{8.179}$$

Substituting $r_b = 0.5\mu$m, $\gamma = 0.8$ N/m [46], and $\sigma_{cr} = 6.9 \times 10^6$ Pa, from Churchman [76] for pure U, the fuel swelling due to fission gas is obtained:

$$\left(\frac{\Delta V}{V_0}\right)_g = \frac{3.59 \times 10^{-24} FT}{1.01 \times 10^7 - \sigma_h} \tag{8.180}$$

where T is in degrees Kelvin, F is in fission/m^3, and σ_h is in Pa. The porosity of metal fuel, also calculated in VSwellingUPuZr, is obtained from Medvedev's report [3] and is given by

$$p = \frac{\left(\frac{\Delta V}{V_o}\right)_g}{\left(\frac{\Delta V}{V_o}\right)_g + 1} \tag{8.181}$$

8.10.3.2 Solid Swelling

Swelling due to solid fission products is assumed to be 1.5 % per 1 % burnup as suggested by [73]:

$$\left(\frac{\Delta V}{V_0}\right)_s = 4.16 \times 10^{-29} F \tag{8.182}$$

where F is the fission rate density in fissions/m^3. Note that the dilatational components of the strain increment tensor can be scaled in this model with a user-defined input parameter called the `anisotropic_strain_scaling` vector. See the User's Manual.

8.10.3.3 Total Isotropic Volumetric Swelling

Following Karahan [24], the three isotropic volumetric swelling components, Equations 8.180, 8.182, and 8.175, are summed together:

$$\left(\frac{\Delta V}{V_0}\right)_{total} = \left(\frac{\Delta V}{V_0}\right)_g + \left(\frac{\Delta V}{V_0}\right)_s - \left(\frac{\Delta V}{V_0}\right)_{opc} \tag{8.183}$$

8.10.4 Fission gas release [FgrUPuZr]

The amount of fission gas generated per unit volume of fuel is given by

$$\nu = \frac{0.26F}{N_A} \tag{8.184}$$

where F is the fission density, 0.26 is the fission yield of gas atoms (can be provided by the user), and N_A is Avogadro's number. According to Barnes [75] when swelling due to fission gas bubbles reachs 33 % (Equation 8.180), the fission gas bubbles interconnect, and 80% of the fission gas is released. Interconnection of the fission gas bubbles transforms closed porosity into the open porosity that facilitates instant release of any consequently generated fission gas. Thus, the fission gas induced swelling is terminated, once the interconnection threshold is reached. In the code, porosity is calculated with Equation 8.181, which is monitored in `[FgrUPuZr]` (read-in as a material property from `[VSwellingUPuZr]`). When the porosity equals 0.24812 (corresponding to a gaseous swelling of 33%), 80% of the fission gas is released after which, all of the fission gas generated is released.

8.10.5 Mechanical Properties [MechUPuZr]

Due to the redistribution of zirconium in the fuel, and the need to model both U-Zr and U-Pu-Zr fuel, correlations included in `MechUPuZr` must be applicable to any concentration of plutonium or zirconium. Unfortunately, the available models for the elastic properties of U-Pu-Zr alloys are generally incomplete. Regardless, some correlations can be made given the sparse data, as described in the Metallic Fuels Handbook [23]. These correlations are described below.

The correlation for Young's modulus can be derived using data from U-11Pu-6.3Zr cast fuel pins as:

$$E = E_u(1-1.2P)\left(\frac{1+0.17W_{Zr}}{1+1.34W_{Zr}} - W_{Pu}\right)\left(1-1.06\left[\frac{T-588}{T_{mu}}\right]\right), \tag{8.185}$$

where $E_u = 1.6\times10^5$ MPa is the Young's modulus for pure U at the reference temperature of 588 K, P is the fractional porosity, W_{Zr} is the zirconium weight fraction, W_{Pu} is the plutonium weight fraction, T is the temperature in K, and $T_{mu} = 1405$ K is the melting temperature of pure uranium.

The correlation for Poisson's ratio can be derived from the U-Zr correlation as:

$$\nu = \nu_u(1-0.8P)\left(\frac{1+3.4W_{Zr}}{1+1.9W_{Zr}}\right)\left(1+1.2\left[\frac{T-588}{T_{mu}}\right]\right), \tag{8.186}$$

where $\nu_u = 0.24$ is the Poisson's ratio of pure U at the reference temperature of 588 K.

8.10.5.1 Thermal expansion

Using the available thermal expansion data for U-yZr [77] and U-xPu-yZr [23], a model can be created that accounts for any variation in x or y. In general, the thermal expansion of U-Zr and U-Pu-Zr fuels can be described as a high and low temperature temperature region of nearly linear

expansion, separated by a jump in the total expansion corresponding to the γ phase transition. For U-Zr, the high and low temperature regions can be described as,

$$(L/L_0)_{U-Zr} = C_1 + C_2 T \cdot 10^{-3} + C_3 T^2 \cdot 10^{-6} + C_4 X_{Zr} + C_5 X_{Zr}^2 + C_6 X_{Zr} T \cdot 10^{-3}, \quad (8.187)$$

where the C terms are constant coefficients, T is the temperature in K, and X_{Zr} is the mole fraction of zirconium. In U-Pu-Zr fuels, the high and low temperature regions can be determined by,

$$(L/L_0)_{U-Pu-Zr} = (L/L_0)_{U-Zr}(1 - X_{Pu}) + (L/L_0)_{cPu}(X_{Pu}) \quad (8.188)$$

where X_{Pu} is the plutonium mole fraction, $(L/L_0)_{U-Zr}$ is calculated using,

$$X_{Zr} = \frac{X_{Zr}}{1 - X_{Pu}}, \quad (8.189)$$

and,

$$(L/L_0)_{cPu} = K_1 + K_2 T \cdot 10^{-3} + K_3 T^2 \cdot 10^{-6} + K_4 X_{Pu} + K_5 X_{Pu}^2 + K_6 X_{Pu} T \cdot 10^{-3}. \quad (8.190)$$

The coefficients used for $(L/L_0)_{U-Zr}$ and $(L/L_0)_{cPu}$ in the high and low temperature regions are displayed in Table 8.11.

Table 8.11: Coefficients for the U-Pu-Zr thermal expansion model.

Coefficient	**Low temperature**	**High temperature**
C_1	-0.2950	0.9325
C_2	0.7236	-.003032
C_3	0.9980	0.9738
C_4	0.2907	0.5636
C_5	0.1650	0.01890
C_6	-1.152	-2.099
K_1	0.9091	-16.44
K_2	0.3875	23.97
K_3	2.5043	-8.002
K_4	-14.414	31.65
K_5	35.19	-48.12
K_6	2.636	-3.330

Given the mathematical representations of the high and low temperature regions, simple linear interpolation can be used to link the two regions:

$$(L/L_0)_{transition} = \left(\frac{(L/L_0)^{T_{end}} - (L/L_0)^{T_{start}}}{T_{end} - T_{start}} \right) (T - T_{start}) + (L/L_0)^{T_{start}}, \quad (8.191)$$

where L/L_0 is calculated at the starting and ending transition temperatures as noted.

The start and end temperatures of the transition regions can be estimated from the data as,

$$T_{start} = 55.59 + 2028T - 1138T^2, \quad (8.192)$$

$$T_{end} = 855.9 + 172.4T. \quad (8.193)$$

The precision of the model can be estimated through the difference between the measured and estimated expansion, as well as the percent difference between the measured and estimated expansion. The model described above results in a standard deviation of the differences of 0.03, (2.4% for percent difference), an average difference of -1×10^{-4}, (2% for percent difference), and an maximum difference of 0.1, (18% for percent difference).

8.11 U-10Mo

8.11.1 Thermal Properties `[ThermalU10Mo]`

Low enriched uranium alloyed with 10 wt% (nominally) molybdenum is herein referred to as U-10Mo. Thermal conductivity k (W/m-K) of U-10Mo is from [78], with F_P as a porosity correction given in 9.1, where it is assumed that $\beta = 2.5$:

$$k = (0.606 + 0.0351T) \times F_p \tag{8.194}$$

Specific heat C_p (J/kg-K) of U-10Mo is from [78]:

$$C_p = 113 + 0.0705T \tag{8.195}$$

8.11.2 Irradiation Creep `[CreepU10Mo]`

A model for the irradiation creep of Creep U-10Mo is available, with the creep rate modeled as a function of effective stress and fission rate. The constitutive relation is taken from [79] and given as

$$\dot{\varepsilon} = A\sigma\dot{F} \tag{8.196}$$

where $\dot{\varepsilon}$ is the creep rate (1/s), σ is the effective (Mises) stress (Pa), $\dot{F}$ is the volumetric fission rate (fissions/m^3-s), and A = 500×10^{-37} is a material constant.

8.12 U_3Si_2

8.12.1 Thermal Properties `[ThermalSilicideFuel]`

The `ThermalSilicideFuel` material model contains three different options to model thermal conductivity and specific heat of U_3Si_2: WHITE, SHIMIZU, and ZHANG. The default model (WHITE) for thermal conductivity is given by equation 4 in White et al. [80]:

$$k = 6.004 + 0.0151 \times T \tag{8.197}$$

where T is temperature in K. This expression is valid for temperatures up to 1773 K. An alternative model (SHIMIZU) is available for use in `ThermalSilicide` by using experimental data from figure 4 of [81]. The conservative expression for thermal conductivity k (W/m-K) of arc cast U_3Si_2 pellets is:

$$k = 7.98 + 0.0051 \times (T - 273.15) \tag{8.198}$$

where T is temperature in K. This expression is valid for temperatures from room temperature to 1473.15 K. This expression may underestimate the true thermal conductivity of U_3Si_2.

The default correlation for the specific heat of C_p (J/kg-K) of U_3Si_2 is equation 2 from White et al. [80]:

$$C_p = 140.5 + 0.02582 \times T \tag{8.199}$$

where T is temperature in K. An alternative correlation that can be used is taken from [82]:

$$C_p = 199 + 0.104 \times (T - 237.15) \tag{8.200}$$

where T is temperature in K. The reference does not state the validity range of this expression. The final thermal conductivity option known as the ZHANG model is more sophisticated because it is able to determine the thermal conductivity of pure uranium metal, pure silicon, U_3Si_2, U_3Si_5, and U_3Si. By utilizing details from Ho et al. [83], Tsiovkin et al. [84], and Glassbrenner and Slack [85], Zhang arrived at an equation of the form:

$$k(c) = \frac{(1-c)/w_e^U + c/w_e^{Si}}{1 + c(1-c)(L_1 + L_2(c^2 - (1-c)^2))} \tag{8.201}$$

where c is the silicon concentration (given as mole fraction in the fuel). For example, for U_3Si_2 c=0.4. $1/w_e^U$ and $1/w_e^{Si}$ are the conductivities of U and Si, respectively. L_1 and L_2 are fitting parameters. The first step is to find the values of w_e^U and w_e^{Si}. Zhang found that the exponential decay function can be used to reproduce these values well:

$$w_e = m_0 + m_1 e^{\left(-\frac{T-T_0}{T_1}\right)} + m_2 e^{\left(-\frac{T-T_0}{T_2}\right)} \tag{8.202}$$

where T is the temperature in K and, m_0, m_1, m_2, T_0, T_1, and T_2 are parameters unique to U or Si. The values of these parameters are summarized in Table 8.12.

Table 8.12: Parameters used to fit the intrinsic thermal resistivity of U and Si

Parameters	m_0	m_1	m_2	T_0	T_1	T_2
U	0.00448	0.0089	0.03267	0.0	500.76917	1555.4716
Si	0.08303	29.152	3.88841	645	87.48315	252.19318

Next, Zhang used the data from White et al.'s references for U_3Si_2 [80] and U_3Si_5 [86] to fit the parameters L_1 and L_2. The equation for these parameters are 5th order polynomials of temperature given by:

$$\begin{aligned} L_1 = {} & 6.0959 - 0.01457T + 1.75527 \times 10^{-5}T^2 - 1.13428 \times 10^{-8}T^3 \\ & + 4.05139 \times 10^{-12}T^4 - 6.04924 \times 10^{-16}T^5 \end{aligned} \tag{8.203}$$

$$\begin{aligned} L_2 = {} & -1.82488 + 0.0148T - 2.92953 \times 10^{-5}T^2 + 2.68933 \times 10^{-8}T^3 \\ & - 1.15846 \times 10^{-11}T^4 + 1.90712 \times 10^{-15}T^5 \end{aligned} \tag{8.204}$$

8.12.2 Volumetric Swelling [VSwellingU3Si2]

Since the data for U_3Si_2 is limited, an empirical expression for the swelling of U_3Si_2 was determined using data from figure 3 of [87]. The swelling of fuel particles was calculated by Finlay using the results of miniplate irradiation tests. To convert Finlay's data (fission density) to FIMA, a value of 10.735 g/cm^3 was used as the heavy metal density, equivalent to 95% theoretical heavy metal density. Based on Finlay's data the volumetric strain can be written as a function of burnup:

$$\frac{dV}{V} = 3.8808 \times Bu^2 + 0.79811 \tag{8.205}$$

where dV/V is the volumetric strain at a given burnup Bu. The burnup is in units of FIMA. The quadratic equation for the total volumetric strain is then decoupled into its solid and gaseous components. The solid swelling is a linear function of burnup based upon the data of Hofman [88] using the same conversion procedure from fission density to burnup given above:

$$\left(\frac{dV}{V}\right)_{solid} = 0.34392 \times Bu \tag{8.206}$$

which results in a gaseous swelling contribution given by the following quadratic function of burnup:

$$\left(\frac{dV}{V}\right)_{gaseous} = 3.8808 \times Bu^2 + 0.45419 \tag{8.207}$$

U_3Si_2 is expected to experience densification similar to UO_2. Thus, the fuel densification can be calculated using the ESCORE empirical model [48] given by:

$$\varepsilon_D = \Delta\rho_0 \left(e^{\left(\frac{Bu\, ln(0.01)}{C_D Bu_D}\right)} - 1 \right) \tag{8.208}$$

where ε_D is the densification strain, $\Delta\rho_0$ is the total densification that can occur (given as a fraction of theoretical density), Bu is the burnup, and Bu_D is the burnup at which densification is complete. For temperatures below 750 °C the parameter C_D is given by $7.2 - 0.0086(T - 25)$; above 750 °C it is 1.0 (T in °C).

8.13 U_3Si_5UN

8.13.1 Thermal Properties [ThermalU3Si5UN]

The `ThermalU3Si5UN` material model contains the model thermal conductivity and specific heat of U_3Si_5UN. The model for thermal conductivity, taken from IFR Handbook, is given by the equation :

$$k = (6.1 \times 10^{-3} \times T + 9) \times f_p \tag{8.209}$$

where f_p is defined by the equation :

$$f_p = \frac{1-p}{1+2.5p} \tag{8.210}$$

where T is temperature in K, and p is the porosity. This expression is valid for temperatures up to 1773 K.

The specific heat C_p, in J/(kg.K) of U_3Si_5UN is defined constant : $C_p = 120$ J/(kg.K).

8.13.2 Volumetric Swelling `[VSwellingUN]`

An empirical expression for the swelling of UN was determined using data from Journal of Nuclear Materials 170 (1990) 169-177 Uranium Nitride Fuel Swelling Correlation [89].

$$s = 0.001 \times 4.7 \times 10^{-11} \times T^{3.12} \times (100 \times Bu)^{0.83} \sqrt{95} \tag{8.211}$$

where Bu is the instantaneous burnup and T the temperature. The volumetric swelling, is calculated by integrating the incremental strain over burnup.

8.13.3 Mechanics `[MechU3Si5UN]`

Young's modulus (Pa) and Poisson's ratio for U3Si5UN, taken from IFR Handbook is :

$$E = 174.88 \times 10^9 Pa \tag{8.212}$$

and

$$v = 0.345 \tag{8.213}$$

The linear thermal expansion, from IFR Handbook is :

$$LTE = 3.8 \times 10^{-11} \times T^3 - 7.6 \times 10^{-8} \times T^2 + 5.8 \times 10^{-5} \times T - 1.2 \times 10^{-2} \tag{8.214}$$

8.14 Zircaloy

8.14.1 Irradiation Creep `[ThermalIrradiationCreepZr4]`

Irradiation-induced creep of cladding materials is based on an empirical model developed by Hoppe [90] that relates the creep rate to the current fast neutron flux and stress. The specific relation implemented is:

$$\dot{\varepsilon}_{ir} = C_0 \Phi^{C_1} {\sigma_m}^{C_2} \tag{8.215}$$

where $\dot{\varepsilon}_{ir}$ is the effective irradiation creep rate (1/s), Φ is the fast neutron flux (n/m^2-s), σ_m is the effective (Mises) stress (MPa), and C_0, C_1, and C_2 are material constants. The material constants C_0, C_1, and C_2 are shown in Table 8.13 for different cladding materials. Note that the original Hoppe formulation is given in terms of circumferential stress, whereas the relation implemented

in BISON assumes an effective (Mises) stress.

Table 8.13: Values of the Material Constants C_0, C_1, and C_2 for Different Cladding Materials

Clad Type	C_0	C_1	C_2
SRA	3.557×10^{-24}	0.85	1.0
RXA	1.654×10^{-24}	0.85	1.0
PRXA	2.714×10^{-24}	0.85	1.0
ZIRLO	2.846×10^{-24}	0.85	1.0

where, SRA = stress relief annealed; RXA = recrystallization annealed; PRXA = partially recrystallization annealed; ZIRLO = SRA ZIRLO^{TM}.

8.14.2 Thermal Creep

Two thermal creep models are available. The Hayes model describes only secondary creep while the Limback model includes both primary and secondary creep.

8.14.2.1 Hayes Secondary Creep `[ThermalIrradiationCreepZr4]`

Secondary thermal creep of zirconium alloys was thoroughly investigated by Hayes and Kassner [91] and found to be well-described by a traditional power-law creep formulation. The specific equation recommended there and implemented in BISON is

$$\dot{\varepsilon}_{ss} = A_0 \left(\frac{\sigma_m}{G}\right)^n e^{\left(\frac{-Q}{RT}\right)} \tag{8.216}$$

where $\dot{\varepsilon}_{ss}$ is the effective thermal creep rate (1/s), σ_m is the effective (Mises) stress (Pa), Q is the activation energy (J/mol), R is the universal gas constant (J/mol-K), T is the temperature (K), G is the shear modulus (Pa), and A_0 and n are material constants. For Zr-4, Moon et al. [92] recommend a temperature dependent shear modulus given by $G = 4.2519 \times 10^{10} - 2.2185 \times 10^7 T$ and Hayes and Kassner [91] specify a creep law power (n) of 5. A value for A_0 is not reported in [91]; however, based on experimental data presented there, an approximate value of $A_0 = 3.14 \times 10^{24}$ (1/s) was computed.

8.14.2.2 Limbäck Primary and Secondary Creep `[MechZry]` `[MechZryModel]`

The creep model proposed by Limbäck [93] includes an expression for primary creep. This can be important as part of power changes when the load on the cladding changes relatively suddenly.

Thermal creep in the Limbäck model is given as the Matsuo model [94] where the creep rate

(hr^{-1}) is

$$\dot{\varepsilon}_{th} = A\frac{E}{T}\left(\sinh\frac{a_i\sigma_{eff}}{E}\right)^n e^{-Q/RT} \tag{8.217}$$

$$a_i = a\left[1 - A_1\left(1 - e^{(-A_2\Phi^{A_3})}\right)\right] \tag{8.218}$$

$$E = 1.148\times10^5 - 59.9T \tag{8.219}$$

where the constants A, Q, and n are shown in Table 8.14 for the different cladding materials, T as temperature (K), $a = 650$ (dimensionless), $R = 8.314$ (J/mol/K), $A_1 = 0.56$ (dimensionless), $A_2 = 1.4\times10^{-27}$ ((n/cm^2)$^{-A_3}$), and $A_3 = 1.3$ (dimensionless).
Based on the Limbäck model, a new model on ZIRLO was developed by adjusting some parameters to fit data on ZIRLO^{TM} material [95, 96, 97].

Table 8.14: Values of the Constants A, Q, and n for Different Cladding Materials

Clad Type	A(K/MPa/hr)	Q(kJ/mol)	n
SRA	1.08×10^9	201	2.0
RXA	5.47×10^8	198	3.5
PRXA	7.06×10^8	199	2.3
ZIRLO	8.64×10^8	201	$f(\sigma_{eff})$

where, SRA = stress relief annealed; RXA = recrystallization annealed; PRXA = partially recrystallization annealed; ZIRLO = SRA ZIRLO^{TM}. $f(\sigma_{eff})$ is a function of effective stress. $f(\sigma_{eff}) = 2$ if $\sigma_{eff} < 220MPa$; $f(\sigma_{eff}) = 2.6$ if $\sigma_{eff} < 400MPa$; Otherwise, $f(\sigma_{eff}) = 1.2667 + 3.333\times10^{-3}\sigma_{eff}$.

Irradiation-induced creep in the Limbäck model is of the form given in Eq. 8.215. The secondary creep rate is then

$$\dot{\varepsilon}_s = \dot{\varepsilon}_{th} + \dot{\varepsilon}_{ir}. \tag{8.220}$$

Primary creep is defined as

$$\varepsilon_p = \varepsilon_p^s\left(1 - e^{(-C\sqrt{\dot{\varepsilon}_s t})}\right) \tag{8.221}$$

$$\varepsilon_p^s = B\dot{\varepsilon}_s^b\left[2 - \tanh(D\dot{\varepsilon}_s)\right]^d \tag{8.222}$$

where $C = 52$ (dimensionless), $B = 0.0216$ (hr^b), $b = 0.109$ (dimensionless), $D = 35500$ (hr), and $d = -2.05$ (dimensionless).

Total creep strain is the combination of the primary and secondary creep:

$$\varepsilon_c = \varepsilon_p^s\left(1 - e^{(-C\sqrt{\dot{\varepsilon}_s t})}\right) + \dot{\varepsilon}_s t. \tag{8.223}$$

8.14.2.3 High Temperature Creep (LOCA) `[MechZryModel]`

During a loss of coolant accident, or LOCA, outward creep deformation of the cladding tube under the effect of internal pressurization and high temperature drives cladding ballooning and

Table 8.15: Material parameters used to calculate creep of Zircaloy-4 [100, 101].

Phase	$\dot{\varepsilon}_{eff}$ (s^{-1})	A ($MPa^{-n}s^{-1}$)	Q (J/mol)	n (-)
α	any	8737	$321000 \cdot 10^5 + 24.69 \cdot (T - 923.15)$	5.89
50%α 50%β	$\leq 3 \cdot 10^{-3}$	0.24	102366	2.33
	$> 3 \cdot 10^{-3}$	Lin. interp. $\ln(A)$	Lin. interp	Lin. interp.
β	any	7.9	141919	3.78

eventual failure due to burst. For LOCA analysis, the large creep deformation of the cladding is defined by a strain rate correlation in the form of a Norton power equation [98, 99, 100]:

$$\dot{\varepsilon}_{eff} = A \cdot exp\left(\frac{-Q}{RT}\right) \cdot {\sigma_{eff}}^n, \tag{8.224}$$

where $\dot{\varepsilon}_{eff}$ (s^{-1}) is the effective creep strain rate, A ($MPa^{-n}s^{-1}$) the strength coefficient, Q (J/mol) the activation energy for the creep deformation, T (K) the temperature, σ_{eff} (MPa) the effective (Von Mises) stress, and n (-) the stress exponent. The components of the strain tensor are then updated at each time step based on the effective strain increment and a flow rule. The material parameters (Table 8.15) used in the model were obtained from tension tests on Zircaloy-4 tubes [99, 100]. In the mixed phase ($\alpha + \beta$) region, interpolations are made to calculate the Norton parameters. Depending on the strain rate, different approaches are adopted [99]:

- For $\dot{\varepsilon}_{eff} \leq 3 \cdot 10^{-3}$ s $^{-1}$, linear interpolation of ln(A), n, and Q is made between the values for pure α and middle of $\alpha + \beta$ (50%α 50%β) phase, and between 50%α 50%β and pure β phase.
- For $\dot{\varepsilon}_{eff} > 3 \cdot 10^{-3}$ s $^{-1}$, it is assumed that the values of ln(A), n, and Q vary linearly between the values for pure α and pure β phase.

To perform the interpolation, the fraction of each phase calculated from a dedicated model as described in Section 8.14.7 is used. The effective creep strain rate as a function of temperature for different stress values is illustrated in Fig. 8.13.

When running a simulation where the temperature in the cladding increases from normal operating conditions (˜600K) up to LOCA temperatures (˜900K), the effective creep strain rate is linearly interpolated between the Matsuo model [94] and the LOCA model. There are a number of regression tests that demonstrate the LOCA behavior and the transition between normal operation secondary thermal creep and LOCA creep.

8.14.3 Combined Creep and Instantaneous Plasticity `[ThermalIrradiationCreepPlasZr4] [MechZryModel]`

Material models are also available for combined instantaneous plasticity and time-dependent creep. Creep is modeled using the irradiation and thermal creep constitutive equations described above. Time-independent plasticity is modeled assuming J2 plasticity based on a simple linear

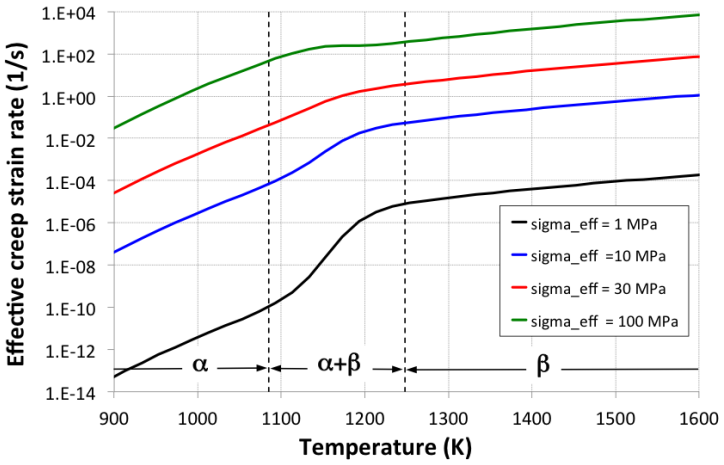

Figure 8.13: Effective creep strain rate of Zircaloy-4 as a function of temperature for different values of the effective stress. The approximate temperature regions corresponding to the different crystallographic phases of the material are highlighted.

strain hardening curve. For each stress update, the model first consideres only the creep contribution to compute a new stress, which is then compared to the yield strength. If above yield, instantaneous plasticity is applied to reduce the stress onto the yield curve. Iteration is employed to insure stress convergence.

8.14.4 Power law hardening plasticity `[ZryPlasticity]`

This is a plasticity model for the Ziracloy cladding taken from [102]. Before yield, the stress-strain relationship follows Hooke's law, i.e.,

$$\sigma = E\varepsilon \tag{8.225}$$

where σ is the stress, ε is the total strain and E is the Young's modulus.

After yield, the stress-strain relationship follows a power law as shown below

$$\sigma = K\varepsilon^n \left(\frac{\dot{\varepsilon}}{10^{-3}}\right)^m \tag{8.226}$$

where K is the strength coefficient, n is the strain hardening exponent, m is the strain rate exponent and $\dot{\varepsilon}$ is the strain rate. Note that the total strain (ε) is used in the above expression.

The yield stress (σ_y) is then the non-zero intersection of the above two equations and is given by

$$\sigma_y = \left[\frac{K}{E^n}\left(\frac{\dot{\varepsilon}}{10^{-3}}\right)^m\right]^{\left(\frac{1}{1-n}\right)} \tag{8.227}$$

In this material model, the Young's modulus E is a function of temperature of the cladding, fast neutron fluence, cold work factor and oxygen concentration and is calculated using the MATPRO material model CELMOD. It should be noted that the Young's modulus calculation is done using the MechZry model. So MechZry model is a requirement for the ZryPlasticity model to produce accurate results. The strength coefficient K, strain hardening exponent n and strain rate exponent m are functions of the cladding temperature, fast neutron fluence, fast neutron flux and cold work factor and the expressions for these are given in [102]. To account for the effect of annealing, the Matpro material model CANEAL is used correct the cold work factor and fast neutron fluence.

The option "use_matpro" can be used to model the strength coefficient K, strain hardening exponent n and strain rate exponent m as a function of the cladding temperature, fast neutron fluence, fast neutron flux and cold work factor as per the expressions given in MATPRO. Note that a fixed strain rate of 1e-3 is used when this option is set to true.

To use this model with the return mapping algorithm, the stress after yield needs to be written in terms of the plastic strain (ε_p) instead of the total strain (ε). This can be achieved by substituting σ/E for the elastic strain. Therefore, the stress-plastic strain relation after yield can be written as

$$\varepsilon_p = \left[\frac{\sigma}{K}\left(\frac{10^{-3}}{\dot{\varepsilon}}\right)^m\right]^{\frac{1}{n}} - \frac{\sigma}{E} \tag{8.228}$$

The hardening modulus can then be obtained as:

$$H = \frac{d\sigma}{d\varepsilon_p} = 1 \Bigg/ \left[\frac{1}{nK}\left(\frac{\sigma}{K}\right)^{\frac{1}{n}-1}\left(\frac{10^{-3}}{\dot{\varepsilon}}\right)^{\frac{m}{n}} - \frac{1}{E}\right] \tag{8.229}$$

8.14.5 Irradiation Growth `[IrradiationGrowthZr4]`

A model for irradiation growth of Zr4 cladding is available. It is taken from the ESCORE model (see [48], Volume 1: Theoretical and Numerical Bases, section 5.3.4). The axial strain is given as

$$\varepsilon = A(\phi t)^n \tag{8.230}$$

where A and n are constants and ϕt is fast neutron fluence. The value for A is 3×10^{-20} N/cm^2. The value for n is 0.794. We generate a strain increment for the irradiation growth as

$$\Delta\varepsilon = A\left((\phi t_i)^n - (\phi t_{i-1})^n\right) \tag{8.231}$$

with i representing the current step number.

Since irradiation growth should occur in the axial direction only while being volume conserving, it is necessary to specify a strain increment for the other two directions. This is given by

$$\Delta\varepsilon_{lateral} = -(1 - (1 + \Delta\varepsilon)^{-0.5}) \tag{8.232}$$

8.14.6 Damage [CumulativeDamageIndex]

Intergranular stress corrosion cracking, typically caused by pellet-clad interaction (PCI), can lead to clad failure during normal operation. A cumulative damage model by Rashid [103] is used in BISON to estimate clading damage for low temperature steady-state conditions. The model is based on the notion of a cumulative damage index, which has the following form.

$$D = \int_0^{t_n} \frac{dt}{t_f(\sigma_{\text{hoop}}, B, T)} \tag{8.233}$$

In Eq.8.233, D is the amount of damage at time t_n (all time in seconds), t_f is the failure time at stress σ_{hoop} (all stress in units of MPa), T is temperature (K), and B is burnup (MWd/MTU). The variable t_f has the form:

$$t_f = \bar{t}\ exp[(1.015\sigma_y + 1.74\sigma_{\text{ref}} - 2.755\sigma_{\text{hoop}})0.01] \tag{8.234}$$

where σ_y is the clad yield stress, and

$$\bar{t} = 5 \times 10^5 (1.13 \times 10^{-4} B - 0.13)^{-0.75} exp[-30(1 - 611/T)] \tag{8.235}$$

where the stress σ_{ref} is a threshold stress, which has the form:

$$\sigma_{\text{ref}} = \begin{cases} 336.476(B - 5000)^{-0.07262} & \text{for Zr2} \\ 310.275(B - 5000)^{-0.0440} & \text{for Zr4.} \end{cases} \tag{8.236}$$

The model for cumulative damage index (Eq.8.233) activates only when $\sigma_{\text{hoop}} > \sigma_{\text{ref}}$ and $B >$ 5000 MWd/MTU.

8.14.7 Phase transformation [ZrPhase]

Under extreme in-service conditions, e.g., during a postulated loss-of-coolant accident (LOCA), fuel cladding will be subjected to a rapid increase in temperature (up to 1000-1500K), which involves time-dependent phase transformation of Zr alloy from hexagonal (α-phase) to cubic (β-phase) crystal structure. Modeling the kinetics of crystallographic phase transformation is pivotal for the assessment of the mechanical properties essential for fuel rod integrity (deformation and burst) during a postulated LOCA.

The crucial parameter for the transformation kinetics is the evolution of the volume fraction of the new phase as a function of time and temperature. A model is available in BISON for calculation of the volume fraction of the favoured phase in Zircaloy-4 as a function of time and temperature during phase transformation in non-isothermal conditions. The model is based on [104, 105, 106]. The phase transformation rate is expressed by

$$\frac{dy}{dt} = k(T)\left[y_s(T) - y\right] \tag{8.237}$$

where y is the volume fraction of β-phase, t (s) the time, y_s (/) the steady-state or equilibrium value of y, and k (s^{-1}) the rate parameter. The β-phase equilibrium fraction is represented by a sigmoid function of temperature

$$y_s = \frac{1}{2}\left[1 + tanh\left(\frac{T - T_{cent}}{T_{span}}\right)\right] \tag{8.238}$$

where T_{cent} and T_{span} are material specific parameters related to the center and span of the mixed-phase temperature region, respectively. For Zircaloy-4, $T_{cent} = 1159 - 0.096w$ (K) and $T_{span} = 44 + 0.026w$ (K) [104] are used, with w being the hydrogen concentration in the range $0 \leq w \leq 1000$ wppm (weight parts per million hydrogen). The rate parameter is expressed in the form

$$k = k_0 exp\left[-\frac{E}{k_b T(t)}\right] + k_m \tag{8.239}$$

where k_0 is a kinetic prefactor, E an effective activation energy, k_b the Boltzmann constant, and k_m a constant. For Zircaloy-4, $k_0 = 60457 + 18129|Q|$ (s^{-1}) and $E/k_b = 16650$ (K) [104, 106] are used, where $Q = dT/dt$ (Ks^{-1}) is the heat rate in the range $0.1 \leq |Q| \leq 100$ Ks^{-1}. The $\alpha \rightarrow \beta$ transformation is purely diffusion controlled, while the $\beta \rightarrow \alpha$ transformation is partly martensitic. This is represented by the constant k_m given in the form [106]

$$\begin{cases} k_m = 0 & \alpha \rightarrow \beta \\ k_m = 0.2 & \beta \rightarrow \alpha \end{cases} \tag{8.240}$$

The starting temperatures for the onset of $\alpha \rightarrow \alpha + \beta$ and $\beta \rightarrow \alpha + \beta$ phase transformations are calculated as (in kelvin) [104]

$$T_{\alpha \rightarrow \alpha+\beta} = \begin{cases} 1083 - 0.152w & \text{for } 0 \leq Q < 0.1 \text{ Ks}^{-1} \\ (1113 - 0.156w)\, Q^{0.0118} & \text{for } 0.1 \leq Q \leq 100 \text{ Ks}^{-1} \end{cases} \tag{8.241}$$

$$T_{\beta \rightarrow \alpha+\beta} = \begin{cases} 1300 & \text{for } -0.1 < Q \leq 0 \text{ Ks}^{-1} \\ 1302.8 - 8.333\,|Q|^{0.477} & \text{for } -100 \leq Q \leq -0.1 \text{ Ks}^{-1} \end{cases} \tag{8.242}$$

for $0 \leq w \leq 1000$ wppm.

The β-phase volume fraction as a function of time is calculated by numerical integration of Eq. (8.237). As default option, this is accomplished using the second order Adams-Moulton (AM2) method. The backward Euler method is also available. The calculated volume fractions of β phase as a function of temperature at equilibrium and for temperature variation rates of ± 10 Ks^{-1} are shown in Fig. 8.14.

8.14.8 Hydride formation `[CladdingHydrides]`

In normal service, waterside oxidation of Zircalloy fuel cladding introduces hydrogen into the cladding. Where the dissolved hydrogen concentration is high enough or the temperature is low enough, zirconium hydride precipitates, forming thin platelets. The orientation of these hydrides depends on the local stress state when they are formed. Immediately after fuel rod removal, the platelets typically are oriented in circumferential rings. However, during later drying stages, the cladding material may heat up enough to re-dissolve the hydrides. Subsequent cooling of the rod at atmospheric pressure causes the hydrides to re-precipitate into radially-oriented crystals which form paths for radial crack formation. Predicting the potential for cracking therefore requires accurate modeling of the time evolution of the hydride concentration throughout the life of the fuel rod. Models for the spatial-temporal distribution of the dissolved and precipitated hydrogen are included in BISON and are discussed below; modeling the orientation of the hydride platelets is in progress in MARMOT.

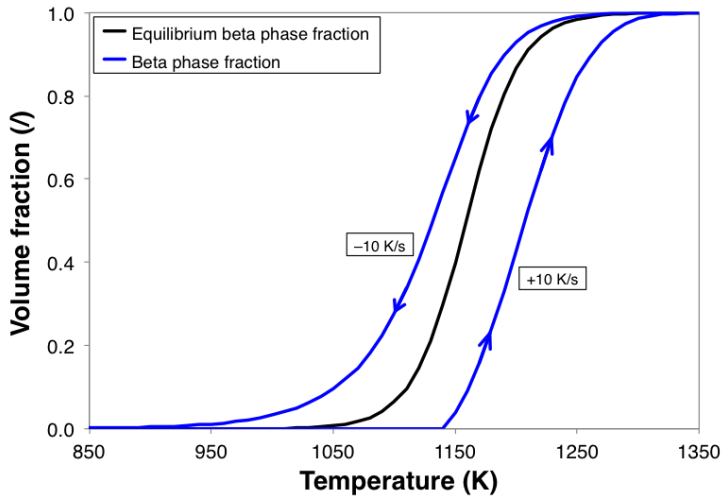

Figure 8.14: Calculated volume fraction of β phase as a function of temperature. Equilibrium conditions (slow temperature variation) and temperature variation rates of ± 10 Ks^{-1} are considered.

8.14.8.1 Hydrogen pickup `[HydrogenPickup]`

The waterside corrosion reaction of the zirconium alloy cladding generates hydrogen at the water-oxide interface:

$$Zr + 2H_2O \rightarrow ZrO_2 + 2H_2 \tag{8.243}$$

Some of the hydrogen migrates through the oxide layer and dissolves in the cladding, where it is slightly soluble. The fraction of the hydrogen produced by the corrosion reaction that ends up in the cladding is termed the hydrogen pickup fraction. Although the mechanism for hydrogen migration through the oxide layer is a topic of active research, the pickup fraction has been well characterized for various zirconium alloys. For example, [107] found the instantaneous hydrogen pickup fraction to be a strong function of alloying elements and to be a complex function of the exposure time.

In BISON, the user specifies a fixed instantaneous hydrogen pickup fraction, so that the average total concentration of hydrogen C_H (including dissolved hydrogen and hydrogen as ZrH_x) in the cladding is roughly proportional to the thickness of the oxide layer [108]:

$$C_H = \frac{4f}{R_{PB}} \frac{\delta}{L-\delta} \frac{M_H}{M_{Zr}} \tag{8.244}$$

where

f is the hydrogen pickup fraction
R_{PB} is the Pilling-Bedworth ratio for ZrO_2 (=1.56)
δ is the oxide thickness

L is the initial thickness of the cladding
M_H is the molecular weight of hydrogen
M_{Zr} is the molecular weight of zirconium
The hydrogen pickup model in BISON can be coupled to any of the oxide growth models described at Section 15.

8.14.8.2 Hydrogen diffusion in the cladding `[IsotropicDiffusion,ThermoDiffusion]`

Hydrogen in solid solution in zirconium will precipitate to form zirconium hydrides as the temperature of the sample is decreased. If the sample is then re-heated, dissolution will begin at a higher temperature than was required for precipitation. This hysteresis effect is due to a volumetric strain caused by mismatch of the density of the hydrides and the surrounding alloy. Thus, there are two terminal solid solubility (TSS) curves, denoted TSS_p for precipitation and TSS_d for dissolution. BISON uses the Arhennius fits from [109] for TSS_d and TSS_p

$$TSS_d = 1.06 \times 10^5 \,\text{ppm}\; e^{-35\,990\,\text{J mol}^{-1}/RT} \tag{8.245}$$

$$TSS_p = 1.39 \times 10^5 \,\text{ppm}\; e^{-34\,470\,\text{J mol}^{-1}/RT}. \tag{8.246}$$

Hydrogen in solid solution in zirconium diffuses under the influence of mass and temperature gradients by Fick's Law and the Soret effect, respectively. The mass flux J is

$$J = -D\left(\nabla C_{ss} + \frac{C_{ss}Q^*}{RT^2}\nabla T\right) \tag{8.247}$$

where
C_{ss} is the concentration of hydrogen in solid solution
D is the mass diffusivity
Q^* is the heat of transport for hydrogen in zirconium
BISON uses D and Q^* from [110]:

$$D = 0.8 \times 10^{-7}\,\text{m}^2\,\text{s}^{-1} e^{-33\,306\,\text{J mol}^{-1}/RT} \tag{8.248}$$

$$Q^* = 25\,070\,\text{J mol}^{-1} \tag{8.249}$$

$$\tag{8.250}$$

Note that since the stoichiometry of the hydride phase is fixed, there is little or no driving force for diffusion of hydrogen in the hydrides. In addition, the diffusivity of hydrogen in hydrides has been measured to be at least 3 times smaller than the diffusivity of hydrogen in zirconium. Thus, we do not account for diffusion of hydrogen in the hydride phase in BISON.

8.14.8.3 Hydride precipitation and dissolution `[HydridePrecipitationRate,HydrogenTimeDerivative]`

In addition to the hysteresis effect, precipitation of hydrides is a non-equilibrium phenomenon at the time scales of interest. Attempts to model the hydride precipitation as an equilibrium process

fail to predict the ingress of hydrogen into the cladding from the oxide interface. The ingress into the cold side of the cladding can only be predicted if the precipitation rate is slow enough to allow a flux of hydrogen into the cladding from the oxide. The rate of precipitation S is often modeled as a kinetic rate [111] that is non-zero in regions where $C_{ss} > TSS_p$:

$$S = K_p(C_{ss} - TSS_p) \tag{8.251}$$

If nucleation is relatively of lesser importance and if the rate of growth of the hydrides is diffusion-limited, the rate coefficient K_p should follow an Arrhenius relation with activation energy similar to the diffusivity D of hydrogen in solid solution. Various fits for K_p have been inferred from experiments to determine TSS_d and TSS_p [110, 112]. In addition, [113] performed an experiment to more directly determine the rate S and obtained reasonable agreement with the deduced rate dependences reported previously, but did not find a consistent temperature dependence for S. Nevertheless, an Arrhenius rate has been useful to model the effects of hydride rim formation in BISON because it improves results near the cold boundary. We have used the rate from [110]

$$K_p = 3881\,\mathrm{s}^{-1}\; e^{-82\,400\,\mathrm{J\,mol}^{-1}/RT} \text{ where } T \leq 625\text{ K} \tag{8.252}$$

The experiments by [112] show that even if a temperature dependence is appropriate, the rate does not increase at temperatures above 625 K. Therefore, in BISON the rate is clamped at a maximum value corresponding to a temperature of 625 K. Note that this rate form is somewhat different than was used in [108].

Relative to the rate of precipitation, the rate of dissolution is assumed to be so rapid that equilibrium is approached and therefore

$$C_{ss} \geq TSS_d \tag{8.253}$$

in regions where a hydride phase exists. To model the inequality in BISON, we again use a finite rate form similar to precipitation but with analogous terms for dissolution:

$$S = K_d(C_{ss} - TSS_d) \tag{8.254}$$

We then set $S = (TSS_d - C_{ss})/\Delta t$ where Δt is the size of the time step. Because we are using a Krylov method, intermediate solution estimates that violate the inequality in Eq. 8.253 will automatically be forced by Eq. 8.254 to converge to solutions that satisfy the inequality.

Combining the flux with the precipitation rate S, we obtain the evolution equations for C_{ss} and for ϕ, the volume fraction of $ZrH_{1.66}$

$$\frac{\partial \theta C_{ss}}{\partial t} = -\nabla \cdot \theta J - \theta S \tag{8.255}$$

$$\frac{\partial \phi}{\partial t} = \frac{M_{ZrH_{1.66}}}{M_H}\frac{\theta S}{1.66} \tag{8.256}$$

$$\tag{8.257}$$

where $\theta \equiv 1 - \phi$ is the volume fraction of the alloy phase. Thus, instead of integrating C_{ss} and $C_p(= C_H - C_{ss})$ (as in the previous implementation in BISON described in [108]), we integrate

C_{ss} and ϕ in time. This form allows us to remove the assumption of a dilute solution of hydrides, which is clearly a poor assumption in the region of the hydride rim. Note that C_{ss} is the *microscopic* concentration of dissolved hydrogen; that is, C_{ss} is the mass fraction of hydrogen in the Zr and not the overall mass fraction of hydrogen in the metal matrix. This is so that we can properly account for the reduced effectiveness of diffusion in the alloy phase as the hydride volume fraction becomes significant. Note also that we assume that there is no density difference between the two phases. This assumption is clearly violated as the less dense hydride phase grows to a large volume fraction in the hydride rim. However, since the hydrides are under compression and therefore do not expand to their full volume and since diffusion is negligible in the hydride phase, we do not expect this assumption to significantly degrade the model of diffusion of hydrogen throughout the cladding.

When applied to LWR cladding, the model described above correctly predicts diffusion of hydrogen towards cold regions and precipitation of hydrides in these regions. However, the model does not predict the measured thickness of the hydride rim for cases where the volume fraction of the hydride in the rim is much less than unity. Since this behavior is commonly observed and since the limiting mechanism for the behavior is currently unknown, BISON allows the user to specify a clamping factor f_{clamp} that reduces θ to an apparently smaller volume fraction of alloy

$$\theta_{\text{apparent}} = 1 - \phi / f_{\text{clamp}} \tag{8.258}$$

We then substitute $\theta \leftarrow \theta_{\text{apparent}}$. Thus, the clamping factor artificially reduces the maximum allowable volume fraction of hydride. For example, if the hydride concentration in the rim is expected to be only 2000 wt.ppm (corresponding to a volume fraction of approximately 0.1), the user can specify that $f_{\text{clamp}} = 0.1$ to limit precipitation of the hydride phase, therefore thickening the rim region artificially. This clamp also provides a numerically smooth limiting behavior in the region of the rim.

8.14.9 Dry cask storage systems (DCSS) `[DryCaskHeatFlux]`

Lifecycle analyses for Zircalloy-clad fuel rods includes estimation of cladding integrity during dry storage and transport in storage casks. Decay heat from radioactive nuclides increases the rod internal pressure and hoop stress and causes the cladding to reach temperatures up to 400° C. These conditions can lead to precipitation of zirconium hydride in radial orientations, reducing the ductility of the cladding.

Predicting the heat loss from a rod located inside an assembly which is packaged with many other assemblies inside of a single dry storage cask is difficult for several reasons. The emissivities and axial power profiles of the fuel rods have large uncertainties. In addition, the spatial distribution of power from the multiple rod assemblies is often unknown ahead of loading. Also, the composition of the fill gas in the cask can be difficult to predict.

These considerations lead to simplified calculations to predict worst-case heating and peak clad temperatures using homogenized models of the interior of the assembly [114]. The calculation includes terms for heat flux from the (homogenized) interior of the assembly to the edge of the rod bundle, from the edge of the rod bundle to the wall of the assembly, and from a single

assembly to the exterior of the cask:

$$Q = C_1(T_m - T_e) + C_2(T_m^4 - T_e^4) \tag{8.259}$$
$$Q = C_3(T_e - T_w) + C_4(T_e^4 - T_w^4) \tag{8.260}$$
$$Q = C_5(T_w - T_a) \tag{8.261}$$
$$\tag{8.262}$$

where
Q = heat flux
$C_1 \ldots C_5$ = lumped heat conductivities
T_m = temperature at middle of assembly (hottest rod)
T_e = temperature at edge of rod bundle
T_w = temperature at of assembly wall
T_a = temperature outside cask (ambient)

Manteufel tabulates values of $C_1 \ldots C_4$ for common geometries for PWR and BWR fuel assemblies using He and N_2 fill gases [114]. C_5 depends on the cask type and loading and is specified by the user in BISON.

8.14.10 Cladding failure (burst) criterion `[FailureCladding]`

For modeling failure due to burst of Zircaloy-4 claddings during LOCA accidents, the BISON code offers three different options:

1. An overstress criterion, which assumes that the time of burst is reached when the local hoop stress equals a limiting burst stress [100]:

$$\sigma_\theta \geq \sigma_b \tag{8.263}$$

   where σ_θ (MPa) is the hoop stress and σ_b (MPa) is the burst stress.

2. A plastic instability criterion, which considers cladding burst at the attainment of a limiting value for the effective plastic strain rate:

$$\dot{\varepsilon}_{pl,eff} \geq \dot{\varepsilon_b} \tag{8.264}$$

   where $\dot{\varepsilon}_{pl,eff}$ is the effective plastic (creep + plasticity) strain rate and $\dot{\varepsilon_b}$ is the limiting value. Following [115], we choose $\dot{\varepsilon_b} = 100\ \mathrm{h}^{-1} \cong 2.78 \cdot 10^{-2}\ \mathrm{s}^{-1}$.

3. A combination of the above criteria, which establishes that cladding burst occurs when either condition 8.263 or 8.264 is fulfilled.

The calculation of the burst stress follows the work of Erbacher et al. [100]. Based on experimental evidence, the burst stress is considered to depend on the temperature and oxygen concentration in the cladding, and is represented by [100]:

$$\sigma_b = a \cdot exp(-bT) \cdot exp\left[-\left(\frac{\eta - \eta_0}{9.5 \cdot 10^{-4}}\right)^2\right] \tag{8.265}$$

Table 8.16: Material parameters used to calculate the burst stress of Zircaloy-4 [100].

Phase	a (MPa)	b (K^{-1})
α	830	$1 \cdot 10^{-3}$
50%α 50%β	3000	$3 \cdot 10^{-3}$
β	2300	$3 \cdot 10^{-3}$

a (MPa) and b (K^{-1}) are constants determined experimentally, and η (-) is the oxygen weight fraction in the cladding. An oxygen weight fraction at fabrication, $\eta_0 = 1.2 \cdot 10^{-3}$, is considered [100]. The current oxygen weight fraction is computed based on the oxygen mass gain from the oxidation model (Section 15.2) as

$$\eta = \frac{2r_{cl,o}}{\rho_{Zy} \cdot \left(r_{met,o}^2 - r_{cl,i}^2\right)} \cdot g + \eta_0 \tag{8.266}$$

where $r_{cl,o}$ (m) is the cladding outer radius, ρ_{Zy} = 6550 kg·m^{-3} the density of the cladding metal, $r_{cl,i}$ (m) the cladding inner radius, g (kg·m^{-2}) the oxygen mass (Section 15.2), and $r_{met,o} = r_{cl,o} - S/R_{PB}$ with S (m) being the oxide layer thickness (Section 15.2) and R_{PB}=1.56 the Pilling-Bedworth ratio for Zr. The values for the parameters a and b are given in Table 8.16. In the mixed phase ($\alpha + \beta$) region, linear interpolations of ln(a) and b are made between the values for pure α and middle of $\alpha + \beta$ (50%α 50%β) phase, and between 50%α 50%β and pure β phase [100]. The volume fractions of each phase are calculated by the phase transformation model described in Section 8.14.7.

As the overstress criterion may lead to unsafe predictions in low-stress situations [115], the combined criterion (3) is recommended.

9 General Material Models

9.1 Thermal Conductivity Porosity Model

A common approach to correct thermal conductivity for fission gas porosity is given by [63]:

$$F_P = (1-P)/(1+\beta P) \tag{9.1}$$

where β is an empirical factor and P is the fission-gas porosity fraction.

9.2 Mass Diffusion Coefficients `[ArrheniusMaterialProperty]` `[ArrheniusDiffusionCoef]`

Mass diffusion coefficients are defined using an Arrhenius form [116]

$$D(T) = \sum_i D_{0,i} \exp\left(\frac{-Q_i}{RT}\right) \tag{9.2}$$

where $D_{0,i}$ is a pre-exponential factor, Q_i is the activation energy, R is the universal gas constant and T is temperature.

10 Fission Gas Behavior

The processes induced by the generation of the fission gases xenon and krypton in nuclear fuel have a strong impact on the thermo-mechanical performance of the fuel rods. On the one hand, the fission gases tend to precipitate into bubbles resulting in fuel swelling, which promotes pellet-cladding gap closure and the ensuing pellet-cladding mechanical interaction (PCMI). On the other hand, fission gas release (FGR) to the fuel rod free volume causes pressure build-up and thermal conductivity degradation of the rod filling gas.
The fundamental physical processes, which control the kinetics of fission gas swelling and release in irradiated UO_2 fuel, may be summarised as follows. Fission gas atoms generated in the fuel grains diffuse towards the grain boundaries through repeated trapping in and irradiation-induced resolution from nanometre-size intra-granular gas bubbles. Although a part of the gas atoms that reach the grain boundaries is dissolved back to the grain interior by irradiation, the majority of the gas diffuses into grain-face gas bubbles, giving rise to grain-face swelling. Bubble growth brings about bubble coalescence and inter-connection, eventually leading to the formation of a tunnel network through which a fraction of the gas is released to the fuel rod free volume.

In BISON, fission gas behavior is computed for each integration point in the fuel finite element mesh. The gas produced at each integration point is computed by a numerical time integration of the gas production rate, given as the product of the fission rate and fractional yield of gas atoms per fission.

The Sifgrs model is recommended.

10.1 Physics-Based Model `[Sifgrs]`

The Simple Integrated Fission Gas Release and Swelling (Sifgrs) model is intended for consistently evaluating the kinetics of both fission gas swelling and release in UO_2. The model incorporates the fundamental features of fission gas behavior, among which are gas diffusion and precipitation in grains, growth and coalescence of gas bubbles at grain faces, thermal, athermal, steady-state, and transient gas release. Through a direct description of the grain-face gas bubble development, the fission gas swelling and release are calculated as inherently coupled processes, on a physical basis. The level of complexity of the model is consistent with reasonable computational cost and the uncertainties inherent in engineering-scale fuel analysis. The Sifgrs model draws on and extends the approach described in [117].

10.1.1 Intra-granular gas behavior

Fission gas transport from within the fuel grains to the grain faces is computed through numerical solution of the relevant diffusion equation in one-dimensional spherical geometry

$$\frac{\partial C_t}{\partial t} = D_{eff}\frac{1}{r^2}\frac{\partial}{\partial r}\left(r^2\frac{\partial C_t}{\partial r}\right) + \beta \tag{10.1}$$

where C_t (m^{-3}) is the intra-granular gas concentration, t (s) the time, D_{eff} (m^2s^{-1}) the effective gas diffusion coefficient, r (m) the radial co-ordinate in the spherical grain, and β ($m^{-3}s^{-1}$) the gas generation rate. The effective diffusion coefficient, which accounts for the effects of repeated trapping in and irradiation-induced resolution from intra-granular bubbles, is calculated based on [118, 119]. Equation 10.1 is solved using dedicated numerical algorithms. Both the algorithm from [120] and the more recent one from [121] are available in BISON.

An empirical model [122] is included to consider intra-granular gas depletion in the high burnup structure (HBS). No specific model for gas release from the HBS is considered.

The contribution of intra-granular bubbles to fission gas swelling (intra-granular swelling), which is generally less important than the swelling due to grain-face bubbles (at least for burnup below about 45 GWd/t [123]), is presently not considered in the model.

10.1.2 Grain-face gas behavior

Numerical solution of Eq. 10.1 allows estimating the arrival rate of gas at the grain faces, thus providing the source term for the grain-face gas behavior module. The latter computes both the fission gas swelling and release through a direct description of the grain-face bubble development, including bubble growth and coalescence (which are reflected in fuel swelling), and eventual inter-connection (leading to thermal FGR). In outline:

- Peculiarities related to the presence of grain edges (where three grains meet) are neglected (e.g., [124, 125]).
- The flux of gas atoms dissolved from the grain faces back to the grain interior by irradiation is neglected [126].
- An initial number density of grain-face bubbles (nucleation centers) is considered, and further nucleation during the irradiation is neglected (one-off nucleation, e.g., [127]).
- The absorption rate of gas at the grain-face bubbles is assumed to equal the arrival rate of gas at the grain faces [127, 128].
- All grain-face bubbles are considered to have, at any instant, equal size and equal lenticular shape of circular projection (e.g., [129]). Hence, the fractional volume grain-face fission gas swelling is given by

$$\left(\frac{\Delta V}{V}\right) = \frac{1}{2}\frac{N_{gf}}{(1/3)r_{gr}}\left(\frac{4}{3}\pi\varphi(\Theta)R_{gf}^3\right) \tag{10.2}$$

  where N_{gf} is the number density of grain-face bubbles per unit surface, r_{gr} the grain radius, Θ the bubble semi-dihedral angle, $\varphi(\Theta)$ the geometric factor relating the volume of a lenticular-shape bubble to that of a sphere, which is $1-1.5\cos(\Theta)+0.5\cos^3(\Theta)$, and R_{gf} the bubble radius of curvature. The factor 1/2 is introduced in Eq. 10.2 because a grain-face bubble is shared by two neighboring grains.

- Bubble growth is treated using the model of Speight and Beere [130], which describes the growth (or shrinkage) of grain-face bubbles as proceeding by absorption (or emission) of vacancies in grain boundaries, induced by the difference between the pressure of the gas in the bubble, p (Pa), and the mechanical equilibrium pressure, p_{eq} (Pa). The vacancy absorption/emission rate at a bubble is given by

$$\frac{dn_v}{dt} = \frac{(2\pi D_v \delta_g)}{kTS}(p - p_{eq}) \tag{10.3}$$

where n_v (-) is the number of vacancies in the bubble, D_v ($m^2 \cdot s^{-1}$) the vacancy diffusion coefficient in grain boundaries, δ_g (m) the thickness of the diffusion layer in grain boundaries, and the parameter S (-) may be calculated as [127]

$$S = -\frac{1}{4}[(3 - F_c) \cdot (1 - F_c) + 2ln(F_c)] \tag{10.4}$$

with F_c being the fraction of grain faces covered by bubbles (fractional coverage). The mechanical equilibrium pressure, p_{eq}, of the gas in a lenticular bubble of circular projection is given by

$$p_{eq} = \frac{2\gamma}{R_{gf}} - \sigma_h \tag{10.5}$$

where γ ($J \cdot m^-2$) is the UO_2/gas specific surface energy, R_{gf} (m) the bubble radius of curvature, and σ_h (Pa) the hydrostatic stress (considered to be negative if the solid medium is under compression). For describing the bubble thermodynamic state, the Van der Waals' equation of state is adopted in the following form:

$$p(V_{gf} - n_g\omega) = n_g kT \tag{10.6}$$

where n_g (-) is the number of fission gas atoms per bubble, k [$J \cdot K^{-1}$] the Boltzmann constant, T (K) the temperature, V_{gf} (m^3) the bubble volume, and ω (m^3) the Van der Waals' volume of a fission gas atom. Given that each bubble consists of vacancies and gas atoms, the volume of a bubble comprising n_g fission gas atoms and n_v vacancies is given by

$$V_{gf} = n_g\omega + n_v\Omega_{gf} \tag{10.7}$$

where Ω_{gf} (m^3) is the atomic (vacancy) volume in the bubble. Combination of Eqs. 10.6 and 10.7 gives for the pressure of the gas in the bubble

$$p = \frac{kT}{\Omega_{gf}}\frac{n_g}{n_v} \tag{10.8}$$

The above approach allows computing the bubble growth rate from the rate of inflow of gas atoms along with the rate of absorption (emission) of vacancies at the bubble. The combined effects of gas atom inflow and vacancy absorption (emission) are interactive,

since the addition of fission gas atoms gives rise to a change in the bubble pressure via Eq. 10.8, which affects the propensity of the bubble to absorb (or emit) vacancies through Eq. 10.3. Given the volume, V_{gf}, of a lenticular bubble of circular projection, the bubble radius of curvature is calculated as

$$R_{gf} = \left(\frac{3V_{gf}}{4\pi\varphi(\Theta)} \right)^{\frac{1}{3}} \tag{10.9}$$

- The process of grain-face bubble coalescence, which leads to a progressive decrease of the bubble number density throughout irradiation, is described using an improved model of White [117, 127]. According to this model, the rate of loss of bubbles by coalescence is given by

$$\frac{dN_{gf}}{dt} = -\frac{6N_{gf}^2}{3+4N_{gf}A_{gf}} \frac{dA_{gf}}{dt} \tag{10.10}$$

  where N_{gf} and A_{gf} represent the number density and projected area of grain-face bubbles, respectively.

- The release of fission gas to the fuel rod free volume following inter-connection of grain-face bubbles and consequent formation of pathways for gas venting to the fuel exterior (thermal release) is modeled based on a principle of grain face saturation. More specifically, a saturation coverage concept is adopted, namely, it is considered that once the fractional coverage, F, attains a saturation value, F_{sat}, the bubble number density and projected area obey the saturation coverage condition

$$F = N_{gf}A_{gf} = F_{sat} \tag{10.11}$$

  where N_{gf} is the bubble number density and $A_{gf} = \pi(\sin(\Theta))^2 R_{gf}^2$ is the bubble projected area on the grain face. The commonly accepted value for F_{sat} is 0.5. Eq. 10.11 implies that, after attainment of the saturation coverage, a fraction of the gas reaching the grain faces is released to the fuel exterior to compensate for continuing bubble growth.

10.1.3 Transient gas behavior

Experimental observations relative to both in-reactor irradiation and post-irradiation annealing of oxide nuclear fuel indicate that substantial fission gas release can occur on a small time scale during temperature transients (burst release). The rapid kinetics of the process cannot be interpreted as purely diffusion-controlled. From the available experimental evidence (e.g., [131, 132, 133, 134]), the following main aspects of transient fission gas behaviour emerge:

- Burst release occurs through grain-face separation (micro-cracking) which entails gas depletion of a fraction of the grain faces.

- Release bursts are triggered by temperature variations, both heating and cooling.

- The rate of gas release during bursts is a peaked function of temperature with the maximum at a 'central' temperature of approximately 1500 C (1773 K).

An extension (transient model) of the treatment of grain-face gas behavior described in Section 10.1.2 is available in BISON, which introduces the effect of micro-cracking on fission gas behavior [135]. According to the BISON transient model, gas depletion of a fraction of the grain faces is modeled as a reduction of the fractional coverage, F. In particular, F is scaled by a factor, f, corresponding to the fraction of non-cracked (intact) grain faces. The reduction of the fractional coverage effectively leads to a decrease of the amount of gas retained in the fuel – consequently, of fission gas swelling – and to a corresponding increase of FGR. This contribution to thermal FGR supplements the diffusion-interconnection mechanism considered in the basic model (Section 10.1.2). Also, the lost gas storing capacity of cracked grain faces is represented by scaling the saturation coverage, F_{sat}, by the factor f. Moreover, the healing process of cracked grain faces is considered as a progressive restoration of the grain-face gas storing capacity. Therefore, the fractional coverage and saturation coverage obey

$$\frac{dF}{dt} = \left[\frac{dF}{dt}\right]_d + F\left[\frac{df}{dt}\right]_c \tag{10.12}$$

$$\frac{dF_{sat}}{dt} = F_{sat}\left(\left[\frac{df}{dt}\right]_c + \left[\frac{df}{dt}\right]_h\right) \tag{10.13}$$

where d stands for diffusion-controlled processes (basic model, Section 10.1.2), c stands for micro-cracking, and h for micro-crack healing. The value for the maximum (initial) saturation coverage (corresponding to all intact grain faces) is $F_{sat,i} = 0.5$. The calculation of the term representing the effects of micro-cracking is detailed hereinafter.

We simplify the micro-cracking process into a purely temperature-dependent behaviour, characterized by a micro-cracking parameter, m. We also observe that the process can only affect intact grain faces, and write

$$\left[\frac{df}{dt}\right]_c = -\frac{dm}{dt}f \tag{10.14}$$

where $\left[df/dt\right]_c$ is the reduction rate due to micro-cracking of the fraction of intact grain faces, f. The micro-cracking parameter is taken as a function of the sole temperature, hence

$$m(T,t) = m(T(t)) \tag{10.15}$$

Then, Eq. 10.14 can be written as

$$\left[\frac{df}{dt}\right]_c = -\frac{dm}{dT}\frac{dT}{dt}f \tag{10.16}$$

implying

$$\left[\frac{df}{dt}\right]_c = 0 \quad if \ \frac{dT}{dt} = 0 \tag{10.17}$$

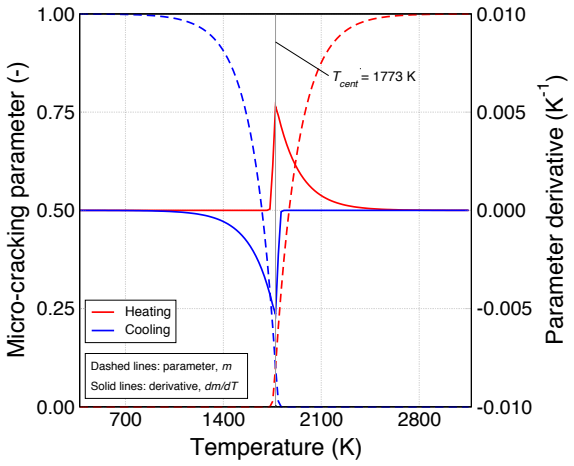

Figure 10.1: Micro-cracking parameter, m, and derivative, dm/dT, as a function of temperature.

which conforms to the experimentally observed characteristic of burst release as triggered by temperature variations. Under the condition expressed by Eq. 10.15, the analytic solution of Eq. 10.14 with initial conditions $f(t_0) = f_0$ and $m(T(t_0)) = m_0$ is

$$f(t) = f_0 \, exp\left[-\left(m(T(t)) - m_0\right)\right] \tag{10.18}$$

Based on the available experimental evidence, the functional form of m is chosen as a temperature-dependent sigmoid function

$$m(T) = 1 - \left[1 + Q \, exp\left(s\frac{T - T_{cent}}{T_{span}}\right)\right]^{-\frac{1}{Q}} \tag{10.19}$$

where T_{cent} (K) is the central temperature, T_{span} (K) is a measure of the temperature-domain width of the phenomenon, Q (-) is a parameter, and s is defined as

$$\begin{cases} s = +1 & if \;\; dT/dt > 0 \;\; \text{(heating transients)} \\ s = -1 & if \;\; dT/dt < 0 \;\; \text{(cooling transients)} \end{cases} \tag{10.20}$$

so that m increases during both heating and cooling transients. The following values are usedfor the parameters: T_{cent}=1773 K, T_{span}=5 K, Q=33. The micro-cracking parameter, m, and the parameter derivative, $dm//dT$, are plotted in Fig. 10.1.

A simple burnup-dependent model is used for micro-crack healing, which is not described here for brevity. Details can be found in [135]. The above treatment of transient fission gas behavior preserves the continuity in both time and space as well as the consistent coupling of the calculated fission gas release and swelling. Early validation has indicated that the model is capable of consistently representing the kinetics of FGR during transient fuel irradiations [135].

10.1.4 Athermal gas release

At low temperature, the fission gas in the matrix of the solid is relatively immobile. Only the gas formed at the external surface of the solid is capable of escape, with an emission rate that is independent of temperature. This athermal contribution to FGR arises from the surface-fission release mechanisms of recoil (direct release of a fission fragment due to its high kinetic energy) and knockout (ejection of a gas atom following elastic interaction with either a primary fragment or energetic particle created in a collision cascade) [136]. These release mechanisms affect only the outer layer of the fuel (within about 10 µm from the surface). The rate of gas atom release per unit fuel volume due to recoil and knock-out, R_a ($m^{-3}s^{-1}$), may be calculated as [136]

$$R_a = \frac{yF}{4V}\left(S_g\mu_f + 2S_t\mu_U^{ko}\right) \tag{10.21}$$

where y (/) is the fractional yield of fission gas atoms, F the fission rate density ($m^{-3}s^{-1}$), V (m^3) the volume of fuel, S_g (m^2) the geometrical surface area of fuel, S_t (m^2) the total surface area of fuel (including cracked surface), μ_f (m) the fission fragment range in the fuel, and μ_U^{ko} (m) the range of the higher order uranium knock-on in UO_2.
In line with [137], the number and length of cracks in each fuel pellet is estimated in a simple way. First, radial cracks are considered to cross the outer, brittle region of the fuel pellet with a temperature lower than 1200 C [138]. Second, the number of pellet cracks is considered to increase linearly with fuel linear power [58]. Then, once the linear power and pellet dimensions are given, the total pellet surface area available for athermal gas release can be calculated.

10.1.5 Grain growth and grain boundary sweeping

Being the fission gas behavior physically dependent on the granular structure of the fuel, the Sifgrs model is coupled with the grain growth model (Section 8.8.15). The grain growth phenomenon affects the fission gas release in three ways. First of all, due to the low solubility of the fission gas, the moving grain boundary does not redeposit any gas in the newly-formed crystal behind it, thus acting as a filter and contributing to the collection of gas at the grain faces (*grain boundary sweeping*). This effect is taken into account in Sifgrs by adding a supplementary fractional release term (s) from within the grains to the grain faces that is equal to the volume fraction of the fuel swept by the moving boundaries:

$$s = \frac{r_i^3 - r_{i-1}^3}{r_i^3} \tag{10.22}$$

where the indices $i-1$ and i refer to the previous and current time, respectively. Secondly, the diffusion distance for the fission gas atoms created in the grains increases as the grains grow. Unlike the first consequence this tends to reduce the release rate. Thirdly, grain growth reduces the capacity of the grain boundaries to store fission gas, as it results in a decrease of the total grain surface-to-volume ratio.

10.2 Modified Forsberg-Massih Model [ForMas]

As an additional option, fission gas release (FGR) can be computed based on the traditional Forsberg-Massih model (ForMas) [139]. This model considers FGR only, hence the fission gas swelling must be calculated separately by means of an empirical model (see Section 8.8.6).

ForMas incorporates a two-stage approach to predict gas release. The first stage computes diffusion of fission gas atoms from within the fuel grains to the grain boundaries, by solving numerically the relevant diffusion equation in spherical co-ordinates. An effective diffusion coefficient is employed, which accounts for gas atom resolution from and trapping into intra-granular bubbles. A formulation based on Turnbull et al. [140, 141] is used to calculate the single gas atom diffusion coefficient, and correction for the effects of intra-granular bubbles is modeled based on the correlations reported in [118]. The second stage of the model utilizes time-dependent boundary conditions to determine grain boundary gas accumulation as inter-granular lenticular bubbles, resolution, saturation, and release. FGR from the grain boundaries is controlled using a grain boundary saturation criterion that involves a threshold concentration of gas at the grain boundaries.

For the current implementation, the fuel grains are assumed to be constant in diameter, thus grain growth and grain-boundary sweeping effects are not considered. Further, the model describes a smooth continuous release process, and is thus not applicable to sudden releases or bursts. These are significant limitations, which must be alleviated to provide more realistic FGR predictions. Accordingly, a more mechanistic model is currently being implemented in BISON which considers the structure of both the fuel (fuel grains and pores) and grain boundaries, and includes the effects of grain growth and grain boundary sweeping. This model will be directly coupled to the volumetric swelling calculation, thus replacing the empirical model described in Eq. 8.80.

Following [142], the ForMas model implemented in BISON includes some modifications compared to the original Forsberg-Massih [139] model, namely:

- The following three-term formulation, based on Turnbull et al. [140, 141], is used to calculate the single gas atom diffusion coefficient

$$
\begin{aligned}
&D_{atomic} = D_1 + D_2 + D_3 \\
&D_1 = 7.6 \cdot 10^{-10} \cdot exp\left(-\frac{35250}{T}\right) \\
&D_2 = 1.41 \cdot 10^{-25} \sqrt{\dot{F}} \cdot exp\left(-\frac{13800}{T}\right) \cdot 4.0 \\
&D_3 = 2.0 \cdot 10^{-40} \cdot \dot{F}
\end{aligned}
\tag{10.23}
$$

  where T (K) is the temperature and $\dot{F}$ ($\mathrm{m}^{-3}\cdot\mathrm{s}^{-1}$) is the fission rate.

- The rate of gas atom resolution from the grain boundaries back into the grains is scaled by fission rate, in line with [118].

- Instead of assuming release of the total gas inventory at the grain boundaries upon saturation [139], only the gas above the saturation level is considered to be released.

The modified Forsberg-Massih model implemented in BISON was tested using a single LWR fuel pellet, assuming uniform constant power. Typical input parameters for UO_2 fuel, as shown in Table 10.1, were assumed. Calculations were compared to the well known Vitanza or Halden threshold [143], which correlates a large set of FGR data in terms of fuel centerline temperature versus burnup at roughly one percent gas release; this threshold is often used to evaluate and calibrate FGR models. A typical comparison is shown in Figure 10.2, which considers the effect of hydrostatic pressure on the computed gas release. Symbols in the figure indicate individual simulations at various axial power levels. As has been reported earlier [144], an increase in hydrostatic pressure significantly shifts the onset of gas release to higher burnups.

Table 10.1: Input parameters for the modified Forsberg-Massih fission gas release model

Fuel grain radius (m)	1.0×10^{-5}
Frac. yield of fission gas atoms per fission	0.3017
Reference resolution rate of intergranular gas (s^{-1})	1.0×10^{-7}
Resolution layer depth (m)	1.0×10^{-8}
Grain boundary bubble radius (m)	0.5×10^{-6}
Nonspherical bubble shape factor [/]	0.287
Bubble surface tension (J/m^2)	0.626
Grain boundary frac. coverage at saturation [/]	0.5

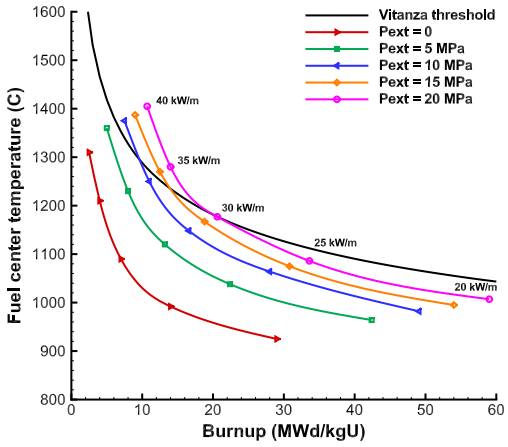

Figure 10.2: Effect of hydrostatic pressure on centerline temperature versus burnup for 1 percent average fission gas release. The Vitanza threshold [143] is included for comparison.

11 Power, Burnup, and Related Models

11.1 Power

The power associated with an LWR fuel rod is typically given as rod averaged linear power (or linear heat rate) in units of W/m. This power varies in time and space. The axial variation in power is given as a scaling factor as a function of distance from the bottom of the rod.

11.1.1 Radial Power Profile

The power density in a fuel pellet varies radially as a function of geometry, initial fuel characteristics, and irradiation history. At the beginning of irradiation (low burnup), the concentration of fissile material is uniform, which means that the radial power has a relatively small variation across the radius. With increasing burnup, the ^{239}Pu concentration markedly increases near the fuel surface due to the capture of epithermal neutrons in the resonances of ^{238}U. Consequently, the concentration of fissile material and the power density profile are steeper near the pellet surface at high burnup. These aspects need to be captured in order to calculate the heat generation and temperature distribution in the pellet accurately.

For this purpose, BISON uses the TUBRNP model of Lassmann ([145]; see also [48]). The local power density, $q'''(r)$, which is needed for the thermal analysis is proportional to the neutron flux and the macroscopic cross section for fission,

$$q'''(r) \propto \sum_k \sigma_{f,k} N_k \phi \tag{11.1}$$

where σ_f is the fission cross section for isotope k, N_k is the concentration (number of atoms per unit volume) of isotope k, and ϕ is the neutron flux. The model computes the radial power profile in the fuel pellet based on Eq. 11.1. Details are given hereinafter.

The average concentrations of heavy metal isotopes are

$$\frac{\mathrm{d}\overline{N}_{235}}{\mathrm{d}t} = -\sigma_{a,235}\overline{N}_{235}\phi, \tag{11.2a}$$

$$\frac{\mathrm{d}\overline{N}_{238}}{\mathrm{d}t} = -\sigma_{a,238}\overline{N}_{238}\phi, \tag{11.2b}$$

$$\frac{\mathrm{d}\overline{N}_{j}}{\mathrm{d}t} = -\sigma_{a,j}\overline{N}_{j}\phi + \sigma_{c,j-1}\overline{N}_{j-1}\phi, \tag{11.2c}$$

where $\overline{N}$ is the average concentration, σ_a is the absorption cross section, σ_c is the capture cross section, , and j represents each of the ^{239}Pu, ^{240}Pu, ^{241}Pu, and ^{242}Pu isotopes.

Recognizing the relationship between an increment of fluence ($\phi\Delta t$) and an increment of burnup (Δbu), the above equations can be reformed as

$$\frac{\mathrm{d}\overline{N}_{235}}{\mathrm{d}\,\mathrm{bu}} = -\sigma_{a,235}\overline{N}_{235}A, \tag{11.3a}$$

$$\frac{\mathrm{d}\overline{N}_{238}}{\mathrm{d}\,\mathrm{bu}} = -\sigma_{a,238}\overline{N}_{238}A, \tag{11.3b}$$

$$\frac{\mathrm{d}\overline{N}_{j}}{\mathrm{d}\,\mathrm{bu}} = -\sigma_{a,j}\overline{N}_{j}A + \sigma_{c,j-1}\overline{N}_{j-1}A, \tag{11.3c}$$

where

$$A = 0.8815\frac{\rho_{fuel}}{\alpha\sum_{k}\sigma_{f,k}\overline{N}_{k}}. \tag{11.4}$$

The leading coefficient (0.8815) is the ratio of the mass of U in UO_2 to the mass of UO_2 ($238/270$), and α is the energy released per fission.

The local isotope concentrations are modeled by

$$\frac{\mathrm{d}N_{235}}{\mathrm{d}\,\mathrm{bu}} = -\sigma_{a,235}N_{235}(r)A, \tag{11.5a}$$

$$\frac{\mathrm{d}N_{238}}{\mathrm{d}\,\mathrm{bu}} = -\sigma_{a,238}\overline{N}_{238}\overline{f}(r)A, \tag{11.5b}$$

$$\frac{\mathrm{d}N_{239}}{\mathrm{d}\,\mathrm{bu}} = -\sigma_{a,239}N_{239}(r)A + \sigma_{c,238}\overline{N}_{238}\overline{f}(r)A, \tag{11.5c}$$

$$\frac{\mathrm{d}N_{j}}{\mathrm{d}\,\mathrm{bu}} = -\sigma_{a,j}N_{j}(r)A + \sigma_{c,j-1}N_{j-1}(r)A, \tag{11.5d}$$

where j represents each of the ^{240}Pu, ^{241}Pu, and ^{242}Pu isotopes. The function $\overline{f}(r)$ is an empirical, normalised radial shape function which encapsulates the contribution of the resonance absorption to the total plutonium production, and is given as

$$\overline{f}(r) = \frac{f(r)}{\int_{r_{in}}^{r_{out}} f(r)r\,\mathrm{d}\,r} \tag{11.6}$$

which guarantees that

$$\frac{2\int_{r_{in}}^{r_{out}}\overline{f}(r)r\,\mathrm{d}\,r}{r_{out}^2 - r_{in}^2} = 1. \tag{11.7}$$

The function $f(r)$ is given as

$$f(r) = 1 + p_1 e^{-p_2(r_{out}-r)^{p_3}} \tag{11.8}$$

where p_1, p_2, and p_3 are constants, r_{out} is the outer radius of the pellet, and r is the radial position.

The neutron flux, $\phi(r)$, is calculated in an approximate way using thermal diffusion theory. The neutron diffusion equation is

$$\nabla^2\phi - \kappa^2\phi = 0 \tag{11.9}$$

The inverse diffusion length, κ, is calculated as

$$\kappa = \sqrt{\frac{\Sigma_{a,th,tot}}{D}} \tag{11.10}$$

where

$$\Sigma_{a,th,tot} = \sum_k \sigma_{a,th,k} \overline{N}_k$$

and

$$D = \frac{1}{3\sigma_s \overline{N}_{tot,HM}}.$$

Here $\sigma_{a,th,k}$ is the thermal absorption cross section of isotope k, $\overline{N}_{tot,HM}$ is the total average concentration of all considered heavy metal isotopes (^{235}U, ^{238}U, ^{239}Pu, ^{240}Pu, ^{241}Pu, and ^{242}Pu), and σ_s is a model parameter.
If the inverse diffusion length, κ, is uniform across the pellet radius (which is a reasonable assumption in absence of burnable absorbers), the solution of Eq. 11.9 is

$$\phi(r) = C_1 I_0(\kappa r) \tag{11.11a}$$

for a solid cylindrical pellet, or

$$\phi(r) = C_1 \left(I_0(\kappa r) + \left[\frac{I_1(\kappa r_{in})}{K_1(\kappa r_{in})} \right] K_0(\kappa r) \right) \tag{11.11b}$$

for a hollow cylindrical pellet

where I and K are the modified Bessel functions and C_1 is a constant.

An example of model results is given in Figure 11.1, which illustrates radial power factor and ^{239}Pu distributions for fresh fuel and at burnup levels of 20 and 40 GWd/tU. The model captures the variation of the radial distribution of fissile ^{239}Pu with burnup and the related effect on radial power distribution.

Figure 11.2 shows comparisons of the BISON model to detailed radial power factor calculations with the HELIOS neutronics code. Considering the simplicity of the model relative to a detailed neutronics analysis, the model appears to provide a satisfactory approximation for the purpose of fuel thermo-mechanics calculations.

BISON also contains the ability to estimate the radial power profile in U_3Si_2 fuel. The same formulation given above for UO_2 is used with different cross sections and mass ratios. The cross sections for U_3Si_2 were generated using the SERPENT neutronics code by Javier Ortensi at the INL. Note that the cross sections provided are one energy group averaged over the fuel pin and thus the thermal absorption cross sections are taken as the absorption cross section.

Standard cross section values used in the model are given in Table 11.1. The thermal absorption cross sections, $\sigma_{a,th}$ are used in the thermal neutron diffusion calculation (Eq. 11.10). The absorption cross sections, σ_a, are computed as sums of the fission and capture cross section values for each isotope. The one energy group cross sections for U_3Si_2 are provided in Table 11.2.

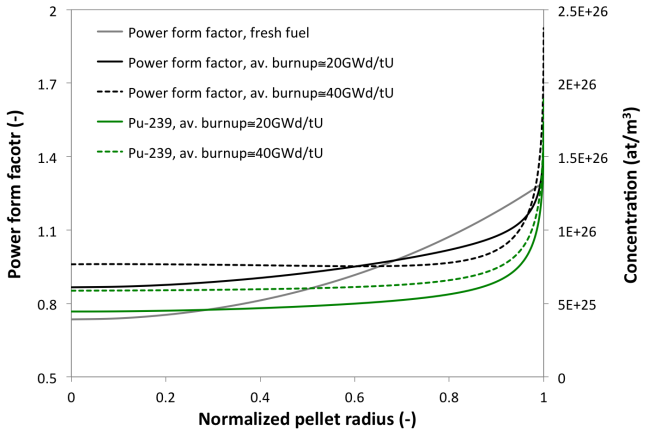

Figure 11.1: Example of calculated distributions of ^{239}Pu and radial power form factor (normalized) for fresh fuel and at 20 and 40 GWd/tU radially averaged burnup.

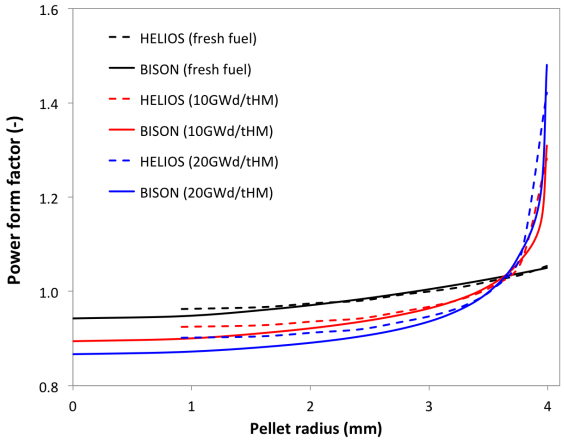

Figure 11.2: Comparisons between radial power form factors (normalized) at different burnups calculated by the BISON model and the HELIOS code.

11.2 Decay Heat

Heat generation due to the radioactive decay of fission products is computed using the "simplified method" described in the 1979 ANS-5.1 Standard on Decay Heat Power in Light Water Reactors [146]. This method assumes that the decay heat power from fissioning isotopes other than ^{235}U is identical to that of ^{235}U and that the fission rate is constant over the operating history at a maximum level corresponding to P_{max}. This simplified method overestimates decay

Table 11.1: Spectrum average cross sections for the TUBRNP model (in barns). See [48].

Light Water Reactor (BWR and PWR)

	^{235}U	^{238}U	^{239}Pu	^{240}Pu	^{241}Pu	^{242}Pu	^{155}Gd	^{157}Gd
Fission	41.5	0	105	0.584	120	0.458	-	-
Capture	9.7	0.78	58.6	100	50	80	490	1267
Thermal absorption	359.68	1.56	1207.5	193.5	1095.24	11.11	19800	85000

Heavy Water Reactor

	^{235}U	^{238}U	^{239}Pu	^{240}Pu	^{241}Pu	^{242}Pu	^{155}Gd	^{157}Gd
Fission	107.95	0	239.18	0.304	296.95	0.191	-	-
Capture	22.3	1.16	125.36	127.26	122.41	91.3	1471	3800
Thermal absorption	395.59	1.7	1095.7	202.2	1113.7	11.98	23924	102477

Table 11.2: One energy group averaged cross sections for U_3Si_2 (in barns).

Light Water Reactor

	^{235}U	^{238}U	^{239}Pu	^{240}Pu	^{241}Pu	^{242}Pu
Fission	23.9101	0.1060	56.8242	0.5939	60.2543	0.4651
Capture	6.4194	0.7540	32.1773	80.0460	21.6194	26.7065
Thermal absorption	30.3248	0.8539	89.0001	80.6386	81.8657	27.1692

heat power, especially with respect to LWR cores having an appreciable amount of plutonium. For finite reactor operating time, the decay heat power is approximated as

$$P_d(t,T) = P_{max}\frac{1.02G_n\left(F(t,\infty)-F(t+T,\infty)\right)}{Q_{mev}} \tag{11.12}$$

where t is the time following reactor shutdown (s), T is the total operating time including intermediate periods at zero power (s), G_n is the neutron capture factor, Q_{mev} is the energy released per fission (MeV/fission), and $F(t,\infty)$ is the decay heat power (MeV/fission) for thermal fission of ^{235}U for an infinite-time base irradiation (tabulated in Table 4 of [146]).

As implemented in BISON, the decay and peak powers are prescribed as fission power densities at finite element material volumes. Spatial variation of the peak power is dictated by the axial and radial power profiles in the fuel, thus the decay power follows the same profiles.

11.3 Burnup Calculation

Burnup is used to calculate fuel properties and the fuel densification and swelling rates. It is computed at each material or integration point based on the following equation from Olander [138]

$$\beta = \frac{\dot{F}t}{N_f^0} \tag{11.13}$$

where $\dot{F}$ is the volumetric fission rate, t is time, and N_f^0 is the initial density of heavy metal atoms in the fuel, which can be computed as

$$N_f^0 = \frac{\rho N_{av}}{M_w} \tag{11.14}$$

where ρ is the initial fuel density, N_{av} is Avagrado's number, and M_w is the molecular weight.

A burnup increment is computed for each time increment and summed to give the total burnup.

$$\beta_i = \beta_{i-1} + \frac{\dot{F}\Delta t}{N_f^0} \tag{11.15}$$

11.4 Fission Rate

The fission rate is calculated from the local power density.

$$\dot{F} = \frac{P}{\alpha} \tag{11.16}$$

where $\dot{F}$ is the fission rate (fission/m^3/s), P is the power density (W/m^3), and α is the energy released per fission (J/fission). α is commonly taken to be 3.28451e-11 J/fission.

11.5 Fast Neutron Flux

Fast neutron flux may be specified as problem input. However, it may also be estimated given the linear heat rate.

$$\dot{\Phi} = cP \tag{11.17}$$

where $\dot{\Phi}$ is the fast neutron flux, c is a conversion factor, typically 3e13 (n/(m^{2}s)/(W/m)), and P is the linear heat rate (W/m).

11.6 Fast Neutron Fluence

Fast neutron fluence is the time-integrated fast neutron flux. In incremental form,

$$\Phi_{n+1} = \Phi_n + \Delta t \dot{\Phi} \tag{11.18}$$

where Φ_n is the value of the fast neutron fluence at step n, Δt is the timestep size, and $\dot{\Phi}$ is the fast neutron flux.

12 Evolving Density

BISON computes the current density throughout the finite element mesh. Conservation of mass requires

$$\rho = \frac{\rho_0 V_0}{V} \tag{12.1}$$

where ρ and ρ_0 are the current and original mass densities, and V and V_0 are the current and original volumes.

The deformation gradient F is defined as

$$F = I + \nabla u \tag{12.2}$$

where I is the identity tensor and u is the displacement vector. The determinant of the deformation gradient is a measure of volume change:

$$\det(F) = \frac{dV}{dV_0}. \tag{12.3}$$

This allows

$$\rho = \frac{\rho_0}{\det(F)}. \tag{12.4}$$

This calculation is done at each integration point throughout the finite element mesh.

13 Gap/Plenum Models

13.1 Gap Heat Transfer

Gap heat transfer is modeled using the relation,

$$h_{gap} = h_g + h_s + h_r \tag{13.1}$$

where h_{gap} is the total conductance across the gap, h_g is the gas conductance, h_s is the increased conductance due to solid-solid contact, and h_r is the conductance due to radiant heat transfer.

The gas conductance h_g is described using the form proposed by Ross and Stoute [147]:

$$h_g = \frac{k_g}{d_g + C_r(r_1 + r_2) + g_1 + g_2} \tag{13.2}$$

where k_g is the temperature dependent thermal conductivity of the gas in the gap, d_g corresponds to the gap size (computed in the mechanics solution), C_r is a roughness coefficient with r_1 and r_2 the roughnesses of the two surfaces, and g_1 and g_2 are jump distances at the two surfaces. The conductivity of the gas mixture (k_g) is computed based on the mixture rule from MATPRO [39], which permits mixtures of ten gases (helium, argon, krypton, xenon, hydrogen, nitrogen, oxygen, carbon monoxide, carbon dioxide, and water vapor). The gas temperature is the average of the local temperatures of the two surfaces. The value of d_g takes the following form for `gap_geometry_type` = PLATE, CYLINDER, and SPHERE respectively:

$$d_g = \text{gap width (PLATE)} \tag{13.3a}$$

$$= r \cdot ln\left(\frac{r_2}{r_1}\right) \text{(CYLINDER)} \tag{13.3b}$$

$$= r^2 \cdot \left(\frac{1}{r_1} - \frac{1}{r_2}\right) \text{(SPHERE)} \tag{13.3c}$$

Temperature jump distance is calculated using Kennard's model based on a review by Lanning [148].

$$g_1 + g_2 = 5756\left(\frac{2 - a_{mix}}{a_{mix}}\right)\left(\frac{k_g\sqrt{T_g}}{P}\right)\left(\sum_{i=1}^{10}\frac{f_i}{M_i}\right)^{-1/2} \tag{13.4}$$

where the units of $g_1 + g_2$, k_g, and P are cm , $\frac{cal}{cm-K-s}$, and $\frac{dynes}{cm^2}$ respectively, f_i is mole fraction of i-th gas species, M_i is molcular weight of i-th gas species, and a_{mix} is accomodation coefficient for the gas mixture. The accomodation coefficients for helium and xenon are as follows:

$$a_{He} = 0.425 - 2.3 \times 10^{-4} T_g \tag{13.5}$$

$$a_{Xe} = 0.749 - 2.5 \times 10^{-4} T_g \tag{13.6}$$

For a gas mixture,

$$a_{mix} = a_{He} + \frac{(a_{Xe} - a_{He})(M_{mix} - M_{He})}{(M_{Xe} - M_{He})} \tag{13.7}$$

where M_{Xe} is molecular weight of xenon, M_{He} is molecular weight of helium, and M_{mix} is molecular weight of gas mixture.

The increased conductance due to solid-solid contact, h_s, is described using the correlation suggested by Ross and Stoute [147]:

$$h_s = C_s \frac{2k_1 k_2}{k_1 + k_2} \frac{P_c}{\delta^{1/2} H} \tag{13.8}$$

where C_s is an empirical constant, k_1 and k_2 are the thermal conductivities of the solid materials in contact, P_c is the contact pressure, δ is the average gas film thickness (approximated as $0.8(r_1 + r_2)$, and H is the Meyer hardness of the softer material. From measurements on steel in contact with aluminum, Ross and Stoute [147] recommend $C_s = 10\ m^{-1/2}$, which is the default value in BISON. As an option, the chemical interaction layer at the fuel-cladding interface can be taken into account in the contact term. Based on experimental work [149], the growth of a (U,Zr)O_{2-x} layer is considered during fuel-cladding contact, and is described based on a parabolic law

$$\frac{dS^2}{dt} = G \tag{13.9}$$

where S (m) is the layer thickness, and $G = 4 \times 10^{-18}$ [149] is the parabolic growth rate. Equation 13.9 is solved numerically by

$$S_i = \sqrt{G\Delta t + S_{i-1}^2} \tag{13.10}$$

where

S_i is the layer thickness at the current time step (m)

S_{i-1} is the layer thickness at the previous time step (m)

Δt is the time increment (s)

The chemical interaction layer is assumed to fill the fuel and cladding roughnesses according to its thickness, effectively reducing the r_1 and r_2 terms in Eq. 13.8 and improving the heat transfer.

The conductance due to radiant heat transfer, h_r, is computed using a diffusion approximation. Based on the Stefan-Boltzmann law

$$q_r = \sigma F_e (T_1^4 - T_2^4) \approx h_r (T_1 - T_2) \tag{13.11}$$

where σ is the Stefan-Boltzmann constant, F_e is an emissivity function, and T_1 and T_2 are the temperatures of the radiating surfaces. The radiant conductance is thus approximated

$$h_r \approx \frac{\sigma F_e (T_1^4 - T_2^4)}{T_1 - T_2} \tag{13.12}$$

which can be reduced to

$$h_r = \sigma F_e (T_1^2 + T_2^2)(T_1 + T_2) \tag{13.13}$$

For infinite parallel plates, the emissivity function is defined as

$$F_e = \frac{1}{1/\varepsilon_1 + 1/\varepsilon_2 - 1} \tag{13.14}$$

where ε_1 and ε_2 are the emissivities of the radiating surfaces. This is the specific function implemented in BISON.

13.2 Mechanical Contact

Mechanical contact between fuel pellets and the inside surface of the cladding is based on three requirements:

$$g \leq 0, \tag{13.15}$$

$$t_N \geq 0, \tag{13.16}$$

$$t_N g = 0. \tag{13.17}$$

That is, the penetration distance (typically referred to as the gap g in the contact literature) of one body into another must not be positive; the contact force t_N opposing penetration must be positive in the normal direction; and either the penetration distance or the contact force must be zero at all times.

In BISON, these contact constraints are enforced through the use of node/face constraints. Specifically, the nodes of the fuel pellets are prevented from penetrating cladding faces. This is accomplished in a manner similar to that detailed by Heinstein and Laursen [150]. First, a geometric search determines which fuel pellet nodes have penetrated cladding faces. For those nodes, the internal force computed by the divergence of stress is moved to the appropriate cladding face at the point of contact. Those forces are distributed to cladding nodes by employing the finite element shape functions. Additionally, the pellet nodes are constrained to remain on the pellet faces, preventing penetration. BISON supports frictionless and tied contact. Friction is an important capability, and preliminary support for fricitonal contact is available.

Finite element contact is notoriously difficult to make efficient and robust in three dimensions. That being the case, effort is underway to improve the contact algorithm.

13.3 Gap/plenum pressure

The pressure in the gap and plenum is computed based on the ideal gas law,

$$P = \frac{nRT}{V} \tag{13.18}$$

where P is the gap/plenum pressure, n is the moles of gas, R is the ideal gas constant, T is the temperature, and V is the volume of the cavity. The moles of gas, the temperature, and the cavity volume in this equation are free to change with time. The moles of gas n at any time is the original amount of gas (computed based on original pressure, temperature, and volume) plus the amount in the cavity due to fission gas released. The temperature T is taken as the average

temperature of the pellet exterior and cladding interior surfaces, though any other measure of temperature could be used. The cavity volume V is computed as needed based on the evolving pellet and clad geometry.

13.4 Gap/plenum temperature

The gap/plenum pressure (Section 13.3) requires the temperature of the gas inside the cladding. Many choices are possible when supplying this temperature. It may be appropriate to supply the temperature at a node, the average temperature of several nodes, or data from an experiment. In this section, we outline an approach for calculating an average gas temperature that takes into account the entire fuel/cladding system.

We seek a weighted average temperature that accounts for the fact that the majority of the gas is in the plenum region. Using a volume-weighted average, the average gas temperature $\bar{T}$ can be approximated as

$$\bar{T} = \frac{\int T \mathrm{d}V}{\int \mathrm{d}V} \tag{13.19}$$

where T is the temperature at a point in the gap/plenum and V is the volume occupied by the gas.

It is necessary to make some approximations in the calculation of this temperature since the gap and plenum volumes are not meshed. We assume that a differential volume ($\mathrm{d}V$) is equal to a varying distance times a differential area ($\delta\ \mathrm{d}A$). This change is appropriate for replacing the integral over the volume of an enclosed space with the integral of the medial surface of that space times a distance representing the depth of the volume at a particular point on the surface.

With this change, it is necessary to replace T with the temperature associated with $\delta\ \mathrm{d}A$. We take this temperature to be the average temperature of the outer and inner surfaces bounding the volume:

$$T = \frac{T_o + T_i}{2}.$$

The medial surface of the gas volume is not known. We instead use the fuel surface. This gives

$$\bar{T} = \frac{\int_{A_f} \frac{T_o+T_i}{2} \delta\ \mathrm{d}A}{\int_{A_f} \delta\ \mathrm{d}A}$$

where A_f is the fuel surface, T_o is the temperature across the gap, T_i is the temperature on the fuel surface, and δ is the gap distance. This approximation is a good one for the plenum region since the plenum volume can be accurately calculated given our assumptions. The accuracy of the calculation will be lower for the gap volume contribution, but since this volume is small (zero in areas of fuel/cladding contact) it is less important.

Note that since this approach places an appropriately large weight on the gas in the plenum, it is important that the temperature of the fuel adjacent to the plenum be accurate. It may be necessary to place insulating pellets in a model in order to calculate realistic temperatures at the top of the fuel stack.

13.5 Integral Fuel Burnable Absorber (IFBA)

An integral fuel burnable absorber (IFBA) is used for optimizing fuel assembly reactivity and power distribution in a core. The IFBA is usually applied as a thin layer of ZrB_2 over some length of a fuel rod. The boron-10 isotope in the IFBA material absorbs a neutron and results in a lithium and helium atom according to the following reaction:

$$^{10}_{5}B + ^{1}_{0}n \rightarrow ^{7}_{3}Li + ^{4}_{2}He$$

Since the IFBA layer is normally on the order of a few microns thick, the helium atoms generated are assumed to be released immediately into the plenum. In addition, the IFBA layer is depleted very quickly and is typically used up in the first $\sim 3\%$ of burnup or ~ 18 months of exposure.

Two models for the helium gas production (i.e., boron-10 depletion) have been implemented in BISON. The first model uses an equation based on burnup while the second is the model used in FRAPCON.

13.5.1 Burnup Based Model

This burnup based equation for boron-10 depletion was generated using a DeCART depletion calculation for boron in an IFBA rod. The effects of boron concentration and U-235 enrichment were studied. In addition, an improved approximation for the time dependency of U-235 number density decrease and fissile plutonium production resulted in the following relationship for the number density of boron-10:

$$N_{^{10}B}(t) = N_{^{10}B}(0) exp\left(\frac{-Bu}{aw_{25} + (bw_{25} + c)Bu}\right) \tag{13.20}$$

where

$$\begin{aligned} N_{^{10}B}(t) &= \text{ Boron-10 number density at time } t \\ N_{^{10}B}(0) &= \text{ Initial boron-10 number density} \\ w_{25} &= \text{ U-235 enrichment} \\ Bu &= \text{ Burnup} \\ a &= 1.59389 \\ b &= -0.00773 \\ c &= 0.01051 \end{aligned}$$

13.5.2 FRAPCON Model

In FRAPCON the helium production rate is derived using an MCNP calculation for boron depletion. The empirical fit to this calculation is

$$\dot{P}_{He} = (A_1 f_{IFBA} + A_2) C_{B_{10}}^2 + (B_1 f_{IFBA} + B_2) C_{B_{10}} \tag{13.21}$$

where

$$\begin{aligned}
\dot{P}_{He} &= \text{ helium production rate (number of atoms/cm}^3\text{-sec)} \\
f_{IFBA} &= \text{ the percent of IFBA fuel rods in a reactor core (valid between 10\% and 50\%)} \\
C_{B_{10}} &= \text{ Boron-10 enrichment (percent) (between 0 and 90\%)} \\
A_1 &= 6.23309 \times 10^{-9} \\
A_2 &= 7.02006 \times 10^{-7} \\
B_1 &= -1.35676 \times 10^{-7} \\
B_2 &= 3.1506 \times 10^{-5}
\end{aligned}$$

The implementation of this empirical relationship in the FRAPCON code uses the following form to calculate the helium production rate

$$\dot{P}_{He} = \left[(A_1 f_{IFBA} + A_2) C_{B_{10}}^2 + (B_1 f_{IFBA} + B_2) C_{B_{10}}\right] \frac{q'}{5.64} \times \frac{\rho_{ZrB_2}}{4.53} \text{ in (atoms/cm}^3\text{-s)} \qquad (13.22)$$

where

$$\begin{aligned}
q' &= \text{ linear power in kW/ft} \\
\rho_{ZrB_2} &= \text{ density of } ZrB_2 \text{ in g/cm}^3 \\
A_1 &= -9.66127 \times 10^8 \\
A_2 &= -1.088109 \times 10^{11} \\
B_1 &= -2.10296 \times 10^{10} \\
B_2 &= 4.8843 \times 10^{13}
\end{aligned}$$

Therefore, the boron depletion rate is $-\dot{P_{He}}$ as given in the equation below

$$\frac{C_{B_t}}{100} = \frac{C_{B_{t-\Delta t}}}{100} - \dot{P}_{He} \Delta t / (5.84 \times 10^{22} \rho_{ZrB_2} / \rho_{90\%TD}) \qquad (13.23)$$

The parameters listed in Table 13.1 are used to calculate the initial number density of boron-10 atoms and therefore the limiting value for the moles of He gas generated by the IFBA material. The model specific parameters for the two equations are listed in Table 13.2. In addition, the burnup equation requires a postprocessor to provide the average burnup in the fuel and the FRAPCON equation requires a postprocessor to provide the rod average linear power.

		Units	
	Parameter	Typical	BISON
	ZrB_2 Loading	mg/in	kg/m
	B-10 Loading	mg/in	kg/m
	IFBA Length	cm	m
	B-10 Enrichment	%	fraction
	ZrB_2 Density	% TD	kg/m^3
or			
and	ZrB_2 Thickness	μm	m
	Fuel Outer Radius	cm	m

Table 13.1: Input Parameters for IFBA Postprocessor

Burnup Based Model

	Units	
Parameter	Typical	BISON
U-235 Enrichment	%	(fraction)

FRAPCON Model

	Units	
Parameter	Typical	BISON
IFBA Rod %	%	(fraction)

Table 13.2: Model Specific Input Parameters for IFBA

14 Coolant Channel Model

In the operating conditions of Light Water Reactors, fuel rods are surrounded by flowing water coolant; the flowing coolant carries the thermal energy generated from nuclear fission reaction and transfers the heat into a steam generator or drives a turbine directly. To predict the thermal response of a fuel rod, thermal hydraulic condition of the surrounding coolant needs to be determined. Such condition in modeling the energy transport aspect of the coolant in BISON code is described by a single coolant channel model. This single channel is used mathematically to describe the thermal boundary condition for modeling the fuel rod behavior. This model covers two theoretical aspects, i.e., the local heat transfer from cladding wall into the coolant and the thermal energy deposition in the coolant in steady state and slow operating transient conditions.

Assumptions and limitations of the coolant channel model are summarized below:

1. Closed channel
   The lateral energy, mass, and momentum transfer in the coolant channel within a fuel assembly is neglected. Therefore, the momentum, mass continuity, and the energy equations are only considered in one-dimension, i.e., the axial direction.

2. Homogeneous and equilibrium flow
   For the flow involving both the vapor and liquid phases, the thermal energy transport and relative motions between the two phases are neglected. This essentially assumes the two-phase flow is in a form of one pseudo fluid.

3. Fully developed flow
   In the application of most heat transfer correlations, the entrance effects are neglected. The heat transfer is assumed to happen in a condition that the boundary layer has grown to occupy the entire flow area, and the radial velocity and temperature profiles are well established.

4. Pressure drop neglected
   The pressure drop due to flow induced resistance is not accounted for in the coolant channel model. Instead, coolant pressure as a function of time and axial location can be an input provided by user through a hand calculation or using a computer code.

14.1 Coolant Enthalpy Model

In steady state operation, the enthalpy rise in a coolant channel with incompressible fluid can be derived using energy conservation equation:

$$H(z) = H_{in} + \frac{\int_0^Z q''(z)\pi D_h \mathrm{d}z + \int_0^Z f_c q' \mathrm{d}z}{GA} \tag{14.1}$$

where
H_{in} is the coolant enthalpy at inlet in (J/kg)
$H(z)$ is the coolant enthalpy at axial location z in (J/kg)
z is axial location (m)
q'' is fuel rod surface heat flux (W/m^2)
q' is fuel rod linear heat generation rate (W/m)
f_c is the fraction of heat generated in the coolant by neutron and gamma rays (dimensionless)
D_h is heated diameter (m)
G is coolant mass flux (kg/sec-m^2)
A is flow area of the coolant channel (m^2)

The mass flux, pressure, and coolant temperature at the inlet of coolant channel are provided as input for calculating coolant enthalpy rise. With calculated enthalpy and input coolant pressure, the corresponding thermodynamic condition can be determined using a steam table. The coolant temperature can be obtained and would be used in the convective boundary condition to compute the clad temperature. The thermal-physical properties of water and steam are evaluated at the corresponding bulk coolant temperature and/or at the cladding wall temperature for the use of calculating heat transfer coefficients between the cladding wall and the coolant.

The inlet mass flux, pressure, and coolant temperature can be provided as functions of time in the code input. Allowing the variation of inlet thermal-hydraulic conditions can be used to model a quasi-steady state when the velocity and thermal energy of coolant at a given location are assumed to achieve the equilibrium condition instantaneously.

14.2 Pre-CHF Heat Transfer Correlations

Depending on the flow rate, flow pattern, and cladding wall surface heat flux, the heat transfer from cladding wall outer surface to coolant can be characterized into different heat transfer regimes.

A set of heat transfer correlations to describe the heat transfer condition prior to the point of Critical Heat Flux (CHF) is described follows:

- Dittus-Boelter correlation:
  Under forced flow condition and when the coolant is still in the liquid phase, the heat transfer from the cladding wall to the coolant is in the regime of single phase forced convection, and the heat transfer can be described by Dittus-Boelter equation.

$$Nu = 0.023 Re^{0.8} Pr^{0.4} \tag{14.2}$$

  The equation is applicable for $0.7 <$ Pr < 100, Re $> 10{,}000$, and $L/D > 60$. Fluid properties are evaluated at the arithmetic mean bulk temperature [151].

- Jens-Lottes correlation:

$$\Delta T = 25 \left(\frac{q''(z)}{10^6} \right)^{0.25} / e^{P/6.2\times 10^6} \tag{14.3}$$

Where, ΔT is the cladding wall super heat = T_W-T_{sat} in (K). q'' is the cladding wall surface heat flux (W/m^2-K)), and P is the coolant pressure (Pa). This correlation is developed based on data at a pressure between 500 psi (3.45 MPa) and 2000 psi (13.79 MPa) in sub-cooled boiling regime. The heat transfer coefficient is given as:

$$h = \frac{[(T_W - T_{sat})e^{P/6.2\times10^6}/25]^4 \times 10^6}{T_W - T_b} \tag{14.4}$$

- Thom correlation:
  A similar correlation is given as follows:

$$\Delta T = 22.7\left(\frac{q''(z)}{10^6}\right)^{0.5}/e^{P/8.7\times10^6} \tag{14.5}$$

  The heat transfer coefficient is:

$$h = \frac{[(T_W - T_{sat})e^{P/8.7\times10^6}/22.7]^2 \times 10^6}{T_W - T_b} \tag{14.6}$$

  This correlation is for water at a pressure between 750 psi (5.17 MPa) and 2000 psi (13.79 MPa); but much of Thom's data were obtained at relatively low heat fluxes according to Tong [152].

- Shrock-Grossman correlation
  Shrock-Grossman heat transfer correlation is used in the regime of saturated boiling. The heat transfer coefficient is given as:

$$h = \left(a_1\frac{q''}{Gh_{fg}} + a_2 X_{tt}^{-b}\right)h_l \tag{14.7}$$

$$X_{tt}^{-1} = \left(\frac{x}{1-x}\right)^{0.9}\left(\frac{\rho_f}{\rho_g}\right)^{0.5}\left(\frac{\mu_g}{\mu_f}\right)^{0.1} \tag{14.8}$$

  Where,
  x is the steam quality
  h_{fg} is the latent heat of vaporization (J/kg)
  h_l is the heat transfer coefficient in the liquid phase at the same mass flux (J/kg)
  G is the mass flux (kg/m^2-sec)
  a_1, a_2, and b are constants as follows:
  $a_1 = 7400$
  $a_2 = 1.11$
  $b = 0.66$

- Chen's correlation

  An alternative correlation that is used in the saturated boiling regime is Chen's correlation. Chen's correlation consists of a convective term (Fh_c) and a nucleation term (Sh_{NB}):

$$h = Fh_c + Sh_{NB} \tag{14.9}$$

  h_c is the modified Dittus-Boelter correlation:

$$h_c = 0.023 \left(\frac{G(1-x)D_e}{\mu_f} \right)^{0.8} Pr_f^{0.4} \frac{k_f}{D_e} \tag{14.10}$$

  F is a factor to account for the enhanced heat transfer due to the turbulence caused by vapor.

$$F = 1, \text{ for } \frac{1}{X_{tt}} < 0.1 \tag{14.11}$$

$$F = 2.35 \left(0.213 + \frac{1}{X_{tt}} \right)^{0.736}, \text{ for } \frac{1}{X_{tt}} > 0.1 \tag{14.12}$$

  The nucleation term is the Forster-Zuber equation:

$$h_{NB} = 0.00122 \left[\frac{(k^{0.79} c_p^{0.45} \rho^{0.49})_f}{\sigma^{0.5} \mu_f^{0.29} h_{fg}^{0.25} \rho_g^{0.24}} \right] \Delta T_{sat}^{0.24} \Delta P^{0.75} \tag{14.13}$$

$$\Delta T_{sat} = T_W - T_{sat} \tag{14.14}$$

$$\Delta P = P(T_W) - P(T_{sat}) \tag{14.15}$$

  S is a suppression factor:

$$S = \frac{1}{1 + 2.53 \times 10^{-6} Re^{1.17}} \tag{14.16}$$

  Where $Re = Re_l F^{1.25}$; Re_l is the Reynold number for liquid phase only.

14.3 Critical Heat Flux Correlations

The sub-cooled and saturated boiling can enhance the heat transfer; however at a critical condition when the cladding outer surface is enclosed by vapor film, the heat transfer can deteriorate significantly, the corresponding heat flux is the Critical Heat Flux (CHF). The following correlations are implemented in BISON to calculate CHF, which can be used to estimate the thermal margin in a coolant channel.

- EPRI-Columbia correlation

$$\frac{q_{CHF}}{10^6} = \frac{A - x_{in}}{C + \left(\frac{x - x_{in}}{q''} \right)} \tag{14.17}$$

where
$A = F_a p_1 p_r^{p_2} G^{(p_5+p_7 p_r)}$
$C = F_c F_{AP} p_3 p_r^{p_4} G^{(p_6+p_8 p_r)}$
$p_1 = 0.5328$
$p_2 = 0.1212$
$p_3 = 1.6151$
$p_4 = 1.4066$
$p_5 = -0.3040$
$p_6 = 0.4843$
$p_7 = -0.3285$
$p_8 = -2.0749$
p_r = critical pressure ratio=system pressure/critical pressure
G = local mass velocity (Mlbm/hr-ft^2)
x_{in} = inlet quality
$F_a = G^{0.1}$
$F_c = 1.183G^{0.1}$
$F_a = F_c = 1$ for no cold wall
q'' =local heat flux (MBtu/hr-ft^2)

F_{AP} is the non-uniform axial heat flux distribution parameter:

$$F_{AP} = 1 + \frac{(Y-1)}{(1+G)} \tag{14.18}$$

Y is Bowring's non-uniform parameter defined as:

$$Y = \frac{\int_0^z q''(z)\mathrm{d}z}{q''(z)z} \tag{14.19}$$

- GE correlation

$$q_{CHF} = 10^6(0.8-x) \text{ for } G \geq 0.5\times 10^6 \text{ lb}_\text{m}/\text{ft}^2\text{-hr} \tag{14.20}$$

$$q_{CHF} = 10^6(0.84-x) \text{ for } G < 0.5\times 10^6 \text{ lb}_\text{m}/\text{ft}^2\text{-hr} \tag{14.21}$$

The correlation is applicable for mass fluxes less than 0.75×10^6 lb$_\text{m}$/ft^2-hr.

- Zuber correlation [153]

$$q_{CHF} = 0.131 h_{fg} \rho_g^{0.5} (\sigma g(\rho_f - \rho_g))^{0.5} \tag{14.22}$$

where
q_{CHF} is the critical heat flux (W/m^2)

h_{fg} is the latent heat of vaporization (kJ/kg)
g is the acceleration due to gravity = 9.8 (m/s^2)
ρ_g is the density of vapor at saturation temperature (kg/m^3)
ρ_f is the density of liquid at saturation temperature (kg/m^3)
σ is the surface tension energy at saturation temperature (N/m)

- BIASI correlation
  BIASI correlation is a function of pressure, mass flux, flow quality, and tube diameters. The correlations are provided in following equations. For $G < 300$kg/m^2-s, the Eq. 14.23 is used; for higher mass flux, the Eq. 14.23 or Eq. 14.24 whichever higher is used.

$$q_{chf} = (15.048 \times 10^7)(100D)^{-n} G^{-0.6} H(p_{bar})(1-x) \tag{14.23}$$

$$q_{chf} = (2.764 \times 10^7)(100D)^{-n} G^{-0.6} \left[1.468 F(p_{bar}) G^{-1/6} - x\right] \tag{14.24}$$

  where,
  $F(p_{bar}) = 0.7249 + 0.099 p_{bar} exp(-0.032 p_{bar})$
  $H(p_{bar}) = -1.159 + 0.149 p_{bar} exp(-0.019 p_{bar}) + 9 p_{bar}(10 + p_{bar}^2)^{-1}$
  $p_{bar} = 10P$
  P is the pressure (MPa)

$$n = \begin{cases} 0.4 & \text{for} \quad D \geq 0.01\text{m} \\ 0.6 & \text{for} \quad D < 0.01\text{m} \end{cases}$$

  The database for the correlation is
  D=0.003-0.0375 m
  L=0.2-6.0 m
  P=0.27-14 MPa
  G=100-600 kg/m^2-s
  x=$1/(1+\rho_f/\rho_g)$-1

The EPRI correlation is used as the correlation for a Pressurized Water Reactor (PWR) environment. The GE correlation is used as the correlation for a Boiling Water Reactor (BWR) environment. Alternatively, an input temperature at critical heat flux is allowed, which would use the selected heat transfer in the nucleate boiling regime and the input temperature to compute the critical heat flux.

14.4 Post-CHF Heat Transfer Correlation

The post-CHF heat transfer regime is divided into transition boiling and film boiling. The transition boiling heat transfer regime occurs when the cladding wall temperature exceeds the Critical Heat Flux (CHF) temperature, but remains below the minimum film boiling temperature. The

heat flux decreases significantly with increasing temperature in this regime. Two heat transfer correlations are implemented for the transition boiling regime. The two correlations are McDonough-Milich-King and modified Condie-Bengtson correlations. The film boiling heat transfer regime occurs when the wall temperature reaches the minimum film boiling temperature. Two correlations are provided for the film boiling region. The correlations are Dougall-Rohsenow and Groenveld correlations. The heat transfer correlations at CHF and in the post-CHF regimes implemented in the BISON code is described as follows:

14.4.1 Transition Boiling

McDonough-Milich-King correlation and modified Condie-Bengtson correlation are implemented for the transition boiling regime.

- McDonough-Milich-King correlation [151] [48]
  The McDonough-Milich-King correlation for forced convection transition boiling is given as follows:

$$\frac{(q_{CHF} - q_{TB})}{(T_W - T_{CHF})} = 4.15e^{3.97/P} \tag{14.25}$$

  The heat transfer coefficient is:

$$h_{TB} = \frac{q_{CHF} - 4.15e^{3.97/P}(T_W - T_{CHF})}{(T_W - T_b)} \tag{14.26}$$

  Where,
  q_{CHF} is the critical heat flux (kW/m^2)
  q_{TB} is the transition region heat flux (kW/m^2)
  T_{CHF} is the wall temperature at critical heat flux (K)
  T_b is the bulk temperature of coolant (K)
  T_W is the wall temperature in the transition region (K)
  P is the system pressure (MPa)
  h_{TB} is the transition boiling heat transfer coefficient (kW/m^2-K)

  The data range for this correlation is as follow:
  Pressure: 5.5 - 13.8 MPa
  Mass Flux: 271.246 - 1898.722 kg/m^2-sec
  Channel Geometry: Tube
  Diameter: 0.00386 m
  Length: 0.3048 m
  Fluid: Water

- Modified Condie-Bengtson correlation [48]
  The modified Condie-Bengtson correlation for high flow rate transition boiling is given as

follows:

$$q_{TB} = C_1 e^{-\frac{(T_W - T_{sat})^{1/2}}{2}} (T_W - T_{sat}) \tag{14.27}$$

The heat transfer coefficient is:

$$h_{TB} = C_1 e^{-\frac{(T_W - T_{sat})^{1/2}}{2}} \tag{14.28}$$

$$C_1 = e^{ln(q_{CHF} - q_{FB}) + 0.5(T_{CHF} - T_{sat})^{1/2} - ln(T_{CHF} - T_{sat})} \tag{14.29}$$

where,
q_{CHF} is the critical heat flux (Btu/hr-ft^2)
q_{TB} is the transition heat flux (Btu/hr-ft^2)
$q_{FB} = h_{FB}(T_{CHF} - T_{sat})$ is the film boiling heat flux at T_{CHF} (Btu/hr-ft^2)
T_{CHF} is the wall temperature at critical heat flux (^{o}F)
T_{sat} is the saturation temperature (^{o}F)
T_W is the cladding wall temperature (^{o}F)
h_{TB} is the transition boiling heat transfer coefficient (Btu/hr-ft^2-^{o}F)

At the CHF point, T_W = T_{CHF}, and

$$q_{TB} = q_{CHF} - q_{FB} \tag{14.30}$$

At T_{CHF}, the critical heat flux is equal to the sum of the film boiling component and the transition boiling component to ensure the predicted boiling curve is continuous.

14.4.2 Film Boiling

Two correlations, Dougall-Rohsenow correlation and Groenveld correlation, are provided for modeling the heat transfer in the film boiling region. In the transition from the transition boiling regime to the film boiling regime, the intercept of the selected film boiling correlation and transition boiling correlation was used to determine the minimum film boiling temperature and minimum film boiling heat flux.

- Dougall-Rohsenow correlation [154] [48]
  The Dougall-Rohsenow correlation for forced convection stable film boiling was developed for high flow rate and low quality (x $<$ 0.3) flow. The heat transfer coefficient is given as:

$$h_{FB} = 0.023 \frac{k_g}{D_{hy}} \left[\frac{GD_{hy}}{\mu_g} \left(x + (1-x) \frac{\rho_g}{\rho_l} \right) \right]^{0.8} \left[\frac{C_{pg}\mu_g}{k_g} \right]^{0.4} \tag{14.31}$$

  Where,
  G is the mass flux (kg/m^2-sec)
  D_{hy} is the hydraulic diameter (m)
  k_g is the thermal conductivity of vapor (W/m-K)

μ_g is the viscosity of vapor (kg/m-sec)
ρ_g is the density of vapor (kg/m^3)
ρ_l is the density of liquid (kg/m^3)
C_{pg} is the specific heat of vapor (J/kg-K)
x is the local quality

The vapor properties of the Prandtl number are evaluated at the saturation temperature. The data range for this correlation is as follow:
Pressure: 0.1154 - 0.1634 MPa
Mass Flux: 450.268 - 1109.396 kg/m^2-sec
Heat Flux: 45.426 - 131.862 kW/m^2
Exit Quality: up to 0.4
Fluid: Freon
Geometry: Tubes
Inner Diameter: 0.004572 m, 0.01036 m
Length: 0.381 m

- Groenveld correlation [151] [48]
The Groenveld correlation for forced convection stable film boiling heat transfer coefficient is:

$$h_{FB} = a\frac{k_g}{D_{hy}}\left[\frac{GD_{hy}}{\mu_g}\left(x+(1-x)\frac{\rho_g}{\rho_l}\right)\right]^b (Pr_{\text{film}})^c Y^d \tag{14.32}$$

Where the parameter Y is given as

$$Y = 1.0 - 0.1\left[(1-x)(\frac{\rho_l}{\rho_g}-1)\right]^{0.4} \quad or \quad Y = 0.1 \tag{14.33}$$

whichever is larger.

Where,
G is the mass flux (kg/m^2-sec)
D_{hy} is the hydraulic diameter (m)
k_g is the thermal conductivity of vapor (W/m-K)
μ_g is the viscosity of vapor (kg/m-sec)
ρ_g is the density of vapor (kg/m^3)
ρ_l is the density of liquid (kg/m^3)
x is the local quality

The coefficients a, b, c and d are given in Table 14.1 below. The Prandtl number of the film is given by

$$Pr_{\text{film}} = \frac{C_{pf}\mu_f}{k_f} \tag{14.34}$$

C_{pf} is the specific heat of vapor at film temperature (J/kg-K)
μ_f is the viscosity of vapor at film temperature (kg/m-sec)
k_f is the thermal conductivity of vapor at film temperature (W/m-K)

The vapor properties of the Prandtl number should be evaluated at the film temperature according to Ref. [1].

$$T_{\text{film}} = \frac{(T_W + T_{sat})}{2} \tag{14.35}$$

where,
T_{sat} is the saturation Temperature (K)
T_W is the cladding wall temperature (K)

Prandtl number is currently evaluated at the saturation temperature in the code.

Table 14.1: Groenveld correlation coefficients a, b, c, d

Parameter	Value
a	0.0522
b	0.688
c	1.26
d	-1.06

The applicable range of data for annuli geometry is shown in the Table 14.2 below.

Table 14.2: Range of data for Groenveld correlation

Parameter	Data Range for Annuli Geometry
Hydraulic Diameter (mm)	1.5 - 6.3
Pressure (MPa)	3.4 - 10
Mass Flux (kg/m^2-sec)	800 - 4100
Heat Flux (kW/m^2)	450 - 2250
Quality	0.1 - 0.9

14.5 Logic to Determine Heat Transfer Regime

The boiling curve in the BISON code depends on the selected pre-CHF, CHF, and post-CHF correlations. The diagrams in Figure 14.1 shows the criteria used in the selection of different heat transfer regimes.

Dittus-Boelter correlation is used for the single phase liquid forced convection and for the single phase vapor forced convection. Thom or Jens-Lottes correlation is used for the sub-cooled boiling regime. Thom, Jens-Lottes, or Chen correlation is used for the forced boiling convection regime. Shrock-Grossman correlation is used for the forced boiling convection and vaporization

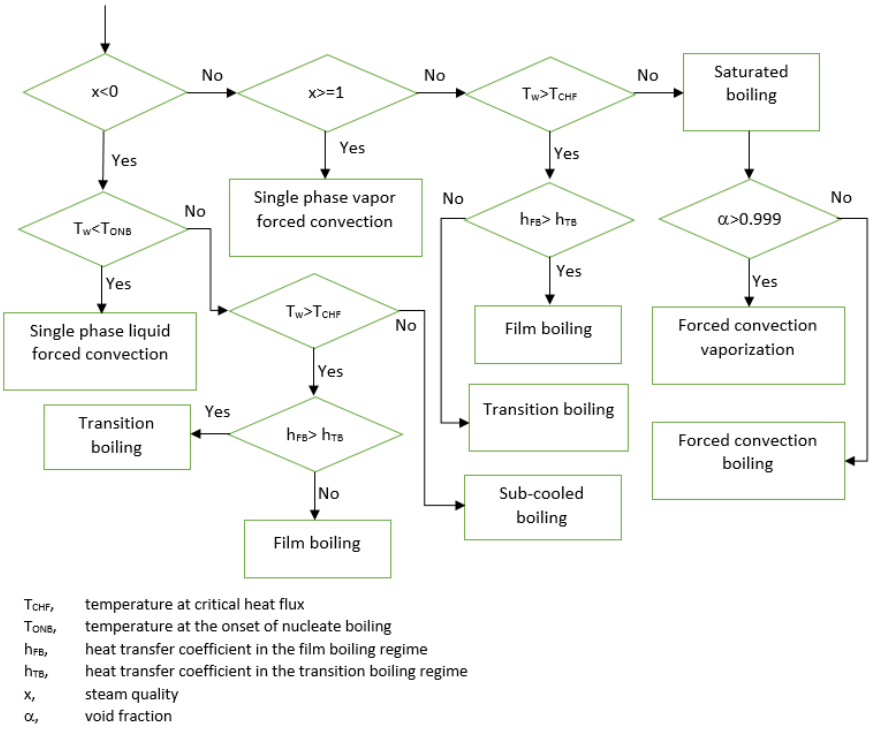

Figure 14.1: Schematic of heat transfer regimes selection criteria

regime. In the transition boiling regime, either the MCDonough-Milich-King ocrrelation or the modified Condie-Bengtson correlation is ued. In the film boiling regime, Dougall-Rohsenow or Groenveld correlation is used. T_{ONB} is the temperate at the onset of nucleate boiling. T_{CHF} is the temperature at the critical heat flux. The selection of different types heat transfer correlations is described in the users manual.

14.6 FLECHT Reflood Heat Transfer Correlations

An empirical approach for modeling the reflooding phase of a LOCA is using the correlations derived from Full Length Emergency Cooling Heat Transfer (FLECHT) tests [155] [156].

Two reflood heat transfer correlations are implemented in BISON code. The first correlation is provided in Ref. [155], and the second one is described in Ref. [156].

The heat transfer correlations compute heat transfer coefficients during reflooding phase of LOCA as a function of flooding rate, cladding temperature at the start of flooding, fuel rod power at the start of flooding, flooding water temperature, pressure, rod elevation and time. The applicable ranges of these variables are shown in Table 14.3 and Table 14.4 for the heat transfer

correlations given in Ref. [155] and Ref. [156] respectively.

The variables are defined as follow:

V_{in} = flooding rate (in/s)
T_{init} = Peak cladding temperature at start of flooding (°F)
Q'_{max} = fuel rod power at axial peak at start of flooding (kW/ft)
P = reactor vessel pressure (psia)
Z = equivalent FLECHT elevation (ft)
T_{sub} = flood water subcooling at inlet (°F)
t = time after start of flooding as adjusted for variable flooding rate (s)
h = heat transfer coefficient (Btu/(hr-ft^2-°F))
Q'_{maxtq} = radial power shape factor
= 1.0 for a nuclear fuel rod
= 1.1 for electrical rod with radially uniform power
B = flow blockage (%)

14.6.1 Generalized FLECHT correlation

The generalized FLECHT correlation from Ref. [155] divides the reflood heat transfer into four time periods: period of radiation only, period I, period II, and period III.

14.6.1.1 Period of Radiation Only

The heat transfer due to radiation is modeled during the time range of t > 0 and t $\leq t_1$. The heat transfer coefficient expression is given as

$$h = h_o + \Delta h[1 - e^{-0.0025t^2}] \tag{14.36}$$

where

$$t_1 = \frac{274e^{-0.0034T_{init}}e^{-0.465V_{in}}e^{-1.25Q'_{max}}}{(1+50^{-0.2(P-30)})} \tag{14.37}$$

$$h_o = 3.67Q'_{max}\left[1 - e^{\left(-\frac{(T_{init}-700)}{435}\right)}\right]F \quad if \quad T_{init} > 700^{\circ}\text{F} \tag{14.38}$$

$$h_o = 0 \quad if \quad T_{init} \leq 700^{\circ}\text{F} \tag{14.39}$$

$$F = F_2 + \frac{(1-F_2)}{(1+50^{(Z-7)})} \tag{14.40}$$

$$F_2 = 0.3 + \frac{0.7}{(1+50^{(2-V_{in})})} \tag{14.41}$$

$$\Delta h = 0.0397 Q'_{max}(T_{init} - 100) \tag{14.42}$$

14.6.1.2 Period I

During Period I, the flow develops from the radiation dominated pre-reflood condition to heat transfer conditions in reflooding phase.

$$t_1 < t \quad and \quad t_q < t_{q2} \tag{14.43}$$

where t_q is defined as

$$t_q = \frac{t - t_1}{t_{q6} - t_1} \tag{14.44}$$

$$\begin{aligned} t_{q6} = 98.39[&e^{-0.0107\Delta T_{sub}}(1 - e^{-0.667 V_{in}})(1 + 0.5e^{-0.000037P^3} + 1.3e^{-0.111V_{in}^2} \\ &+ 17.3e^{-0.000037P^3}e^{-0.49V_{in}^2})(1.207 {Q'_{maxtq}}^{1.5} - 0.667) + \left(\left(\frac{3.28}{V_{in}}\right)^{1.1} - 2.8e^{-V_{in}}\right) \\ &(1 + 0.5e^{-0.000037P^3})](1 + 0.0000588T_{init} - 1.05e^{-0.0025T_{init}}) \\ &\left(1 + \frac{0.5}{(1 + 50^{(2 - 0.667V_{in})})}\right)\left((1 + \frac{0.32}{(1 + 50^{(5 - 0.1P)})}\right) \end{aligned} \tag{14.45}$$

t_{q2} is defined as

$$t_{q2} = 0.62[(1 - e^{-0.192Z}) - 0.115Ze^{-0.0368Z^2}] \tag{14.46}$$

The heat transfer coefficient during Period I is calculated as follow

$$\begin{aligned} h = h_1\left[1 - e^{\left(-\frac{10(X_2 - X)}{X_2}\right)}\right] + \left[h_{12} - h_1\left(1 - e^{\left(-\frac{10(X_2 - X)}{X_2}\right)}\right)\right] \\ [1 - e^{-X} - 0.9Xe^{-X^2}]\left[1 - \frac{2.21e^{-0.4V_{in}}ue^{-u}e^{-(0.588Z - 3.824)^2}}{\left(1 + 100^{10(\frac{t_q}{t_{q2}} - 9)}\right)}\right] \end{aligned} \tag{14.47}$$

where

$$h_1 = 3.67 Q'_{max}\left(1 - e^{\left(-\frac{T_{init} - 700}{435}\right)}\right) + \Delta h(1 - e^{-0.0025t_1^2}) \quad if\ T_{init} > 700^{\circ}\mathrm{F} \tag{14.48}$$

$$h_1 = \Delta h(1 - e^{-0.0025t_1^2}) \quad if \quad T_{init} \leq 700^{\circ}\mathrm{F} \tag{14.49}$$

$$X_2 = 17.6[1 + 4.37e^{-0.0166\Delta T_{sub}}][1 - e^{-(0.00075 + 0.0000272(V_{in} - 8)^2)f_6}]t_{q2}f_1 \tag{14.50}$$

$$h_{12} = 2.644 + 1.092Q'_{max} + [35.7 + (22 - 0.00303Z^{4.1})(1 - e^{-0.0383P} - 0.034Pe^{-0.0011P^2})][1 - e^{-0.2V_{in}}] + 8[1 - e^{-2V_{in}}]\left[1 - e^{\left(-\frac{B}{25}\right)}\right] \quad (14.51)$$

$$X = 17.6[1 + 4.37e^{-0.0166\Delta T_{sub}}][1 - e^{-(0.0075+0.0000272(V_{in}-8)^2)f_6}]t_q\left(\frac{t - t_1}{t_{q2}(t_{q6} - t_1)}\right)^{f_2} \quad (14.52)$$

$$u = 9\left[\frac{f_1 t_q}{(t_{q2}^{1+f_2 f_3})}\right]^2 \quad (14.53)$$

$$f_1 = 0.436 + 0.455f_5 \quad (14.54)$$

$$f_2 = 0.564 - 0.455f_5 \quad (14.55)$$

$$f_3 = 2.8 - 4.8e^{0.688-1.67V_{in}} \quad (14.56)$$

$$f_4 = 1 - e^{-(0.026P+1.041V_{in}+10.28e^{-3.01Q'_{max}}-0.651)} \quad (14.57)$$

$$f_5 = Q'_{max} + \frac{(1.24 - Q'_{max})}{(1 + 50^{(5-2V_{in})})} \quad (14.58)$$

$$f_6 = 0.5[T_{init} - 1000 + (T_{init}^2 - 2000T_{init} + 1.0001(10^6))^{0.5}] + 350 \quad (14.59)$$

14.6.1.3 Period II

During this period, the heat transfer coefficient reaches a plateau with a rather slow increase. The time range for Period II is

$$t_{q2} < t_q < t_{q3} \quad (14.60)$$

where

$$t_{q3} = 1.55[(1 - e^{-0.205Z}) - 0.154Ze^{-0.0421Z^2} + 0.26e^{-2.77(10^{-6})T_{init}^2}] \quad (14.61)$$

The heat transfer coefficient during Period II is computed by the equation

$$h = h_2 + b_1[y^2 + b_2(y^2 - b_3y^3) + b_4y^2e^{-6.38y}] + 60e^{-2.77(10^{-6})T_{init}^2}\left(\frac{y}{y_3}\right)e^{-2.25\left(\frac{y}{y_3}\right)^2} \quad (14.62)$$

$$h_2 = h_{12}[(1-e^{X_2}) - 0.9X_2 e^{-X_2^2}] \tag{14.63}$$

$$\begin{aligned} b_1 = {} & [682 - 650(1-e^{4-Z})][1-e^{-0.95(1-0.0488Z)V_{in}}][1-e^{-0.0238\Delta T_{sub}}] \\ & \left[0.696 + 0.304e^{-\left(\frac{B}{25}\right)}\right][1+0.2(1-f_4)][1+e^{-0.8503Z^2+1.0986123Z+2.3025851}] \end{aligned} \tag{14.64}$$

$$y = t_q - t_{q2} \tag{14.65}$$

$$y_3 = t_{q3} - t_{q2} \tag{14.66}$$

$$b_2 = 0.4Z[1-e^{-2(Z-3.5)}][1.33(1-e^{-0.0227P})-1] - 2.9[1-e^{-\frac{V_{in}}{2.5}}][1-e^{-\frac{B}{25}}] \tag{14.67}$$

$$b_3 = 2.55(Z-3.7)^2 e^{3.7-Z} \tag{14.68}$$

$$b_4 = 87.5V_{in}e^{-V_{in}^2}e^{-0.036\Delta T_{sub}} \tag{14.69}$$

$$if \quad Z < 4, \quad b_3 = b_2 = 0 \tag{14.70}$$

14.6.1.4 Period III

During this period, the flow pattern might have changed to film boiling regime ,and the heat transfer coefficient increases rapidly as the quench front approaches. The time range of Period III is

$$t_{q3} < t_q \tag{14.71}$$

t_q is the time of quenching

The heat transfer coefficient during Period III is calculated as follow

$$h = h_3 + C(t_q - t_{q3}) \tag{14.72}$$

where

$$h_3 = h_2 + b_1[y_3^2 + b_2(y_3^2 - b_3 y_3^3) + b_4 y_3^2 e^{-6.38y_3}] \tag{14.73}$$

$$C = 420[1-e^{-0.00625b_1}]f_4 \tag{14.74}$$

$$y_3 = t_{q3} - t_{q2} \tag{14.75}$$

14.6.1.5 Modification for Low Flooding Rates

The heat transfer coefficients for Periods I, II, and III is multiplied by a factor f to best match the test data performed at low flooding rates. The factor f is calculated as follow

$$f = f_7 - f_8 \tag{14.76}$$

where

$$f_7 = 0.978 + \frac{0.022}{[1 + 30^{(t_{q2} - t_q)}(t_{q6} - t_1)]} \tag{14.77}$$

$$f_8 = f_a + \frac{1 - f_a}{[1 + 50^{(Z-7)}]} \tag{14.78}$$

$$f_a = f_b + \frac{1 - f_b}{[1 + 50^{(2 - V_{in})}]} \tag{14.79}$$

$$f_b = 0.3 + 0.7[1 - e^{-1.5 t_q}] \tag{14.80}$$

The above correlations are valid over the following ranges of parameters:

Table 14.3: Range of applicability of generalized FLECHT correlation [155]

Variable	Applicable range of variable in British unit	Applicable range of variable in SI unit
Flooding rate	0.4 - 10 in/s	0.0102 - 0.254 m/s
Reactor vessel pressure	15 - 90 psia	0.103 - 0.62 MPa
Inlet coolant subcooling	16 - 189 ^{o}F	264.3 - 360.4 K
Initial cladding temperature	300 - 2200 ^{o}F	420 - 1478 K
Flow blockage ratio	0 - 75 %	0 - 75 %
Equivalent elevation in FLECHT facility	2 - 10 ft	0.6096 - 3.048 m

14.6.2 WCAP-7931 FLECHT correlation

The WCAP-7931 correlation [156] divides the reflood heat transfer into three time periods which are designated as Period I, Period II, and Period III.

14.6.2.1 Period I

The time range of Period I is

$$0 < t_q < t_{q2} \tag{14.81}$$

where t_q is defined as

$$t_q = \frac{t}{t_{q6}} \tag{14.82}$$

The quench time is defined as

$$\begin{aligned} t_{q6} = 98.39[&e^{-0.0107\Delta T_{sub}}(1-e^{-0.667V_{in}})(1+0.5e^{-0.000037P^3}+1.3e^{-0.111V_{in}^2} \\ &+17.3e^{-0.000037P^3}e^{-0.49V_{in}^2})(1.207{Q'_{max}}^{1.5}-0.667)+\left(\left(\frac{3.28}{V_{in}}\right)^{1.1}-2.8e^{-V_{in}}\right) \\ &(1+0.5e^{-0.000037P^3})](1+0.0000588T_{init}) \end{aligned} \tag{14.83}$$

t_{q2} is defined as

$$t_{q2} = 0.62[(1-e^{-0.192Z})-0.115Ze^{-0.0368Z^2}] \tag{14.84}$$

The heat transfer coefficient during Period I is calculated as follow

$$\begin{aligned} h = h_1\left[1-e^{\left(-\frac{10(X_2-X)}{X_2}\right)}\right]+\left[h_{12}-h_1\left(1-e^{\left(-\frac{10(X_2-X)}{X_2}\right)}\right)\right] \\ [1-e^{-X}-0.9Xe^{-X^2}]\left[1-2.21e^{-0.4V_{in}}ue^{-u}e^{-(0.588Z-3.824)^2}\right] \end{aligned} \tag{14.85}$$

where

$$h_1 = 3.67Q'_{max}\left(1-e^{\left(-\frac{T_{init}-700}{435}\right)}\right) \tag{14.86}$$

$$X_2 = 17.6[1+4.37e^{-0.0166\Delta T_{sub}}][1-e^{-(0.00075+0.0000272(V_{in}-8)^2)(T_{init}-650)}]t_{q2} \tag{14.87}$$

$$\begin{aligned} h_{12} = 4+[35.7+(22-0.00303Z^{4.1})(1-e^{-0.0333P} \\ -0.034Pe^{-0.0011P^2})][1-e^{-0.2V_{in}}]+8[1-e^{-2V_{in}}]\left[1-e^{\left(-\frac{B}{25}\right)}\right] \end{aligned} \tag{14.88}$$

$$X = 17.6[1+4.37e^{-0.0166\Delta T_{sub}}][1-e^{-(0.0075+0.0000272(V_{in}-8)^2)(T_{init}-650)}]t_q \tag{14.89}$$

$$u = 9[\frac{t_q^2}{t_{q2}^2}] \tag{14.90}$$

14.6.2.2 Period II

The time range of Period I is

$$t_{q2} < t_q < t_{q3} \tag{14.91}$$

where

$$t_{q3} = 1.55[(1 - e^{-0.205Z}) - 0.154Ze^{-0.0421Z^2}] \tag{14.92}$$

The heat transfer coefficient during Period II is computed by the equation

$$h = h_2 + b_1[y^2 + b_2(y^2 - b_3y^3) + b_4y^2e^{-6.38y}] \tag{14.93}$$

where

$$h_2 = h_{12}[(1 - e^{X_2}) - 0.9X_2e^{-X_2^2}] \tag{14.94}$$

$$b_1 = [682 - 650(1 - e^{4-Z})][1 - e^{-0.95(1-0.0488Z)V_{in}}][1 - e^{-0.0238\Delta T_{sub}}] \left[0.696 + 0.304e^{-\left(\frac{B}{25}\right)}\right] \tag{14.95}$$

$$y = t_q - t_{q2} \tag{14.96}$$

$$b_2 = 0.4Z[1 - e^{-2(Z-3.5)}][1.33(1 - e^{-0.0227P}) - 1] - 2.9[1 - e^{-\frac{V_{in}}{2.5}}][1 - e^{-\frac{B}{25}}] \tag{14.97}$$

$$b_3 = 2.55(Z - 3.7)^2e^{3.7-Z} \tag{14.98}$$

$$b_4 = 87.5V_{in}e^{-V_{in}^2}e^{-0.036\Delta T_{sub}} \tag{14.99}$$

14.6.2.3 Period III

The time range of Period III is

$$t_{q3} < t_q \tag{14.100}$$

The heat transfer coefficient during Period III is calculated as follow

$$h = h_3 + C(t_q - t_{q3}) \tag{14.101}$$

where

$$h_3 = h_2 + b_1[y_3^2 + b_2(y_3^2 - b_3 y_3^3) + b_4 y_3^2 e^{-6.38 y_3}] \tag{14.102}$$

$$C = 420[1 - e^{-0.00625 b_1}] \tag{14.103}$$

$$y_3 = t_{q3} - t_{q2} \tag{14.104}$$

The above correlations are valid over the following ranges of parameters:

Table 14.4: Range of applicability of FLECHT correlation from WCAP-7931 report

Variable	Applicable range of variable in British unit	Applicable range of variable in SI unit
Flooding rate	0.4 - 10 in/s	0.0102 - 0.254 m/s
Reactor vessel pressure	15 - 90 psia	0.103 - 0.62 MPa
Inlet coolant subcooling	16 - 189 ^{o}F	264.3 - 360.4 K
Initial cladding temperature	1200 - 2200 ^{o}F	922 - 1479 K
Flow blockage ratio	0 - 75 %	0 - 75 %
Equivalent elevation in FLECHT facility	4 - 8 ft	1.219 - 2.438 m

14.7 Properties for Water and Steam

Properties for water and steam consist of thermodynamic properties, transport properties, and other physical properties used in the heat transfer correlations. They are implemented based on a few standards specified by the International Association or Properties for Water and Steam (IAPWS). The thermodynamic properties, or the steam tables, are implemented in the MOOSE module, `water_steam_eos`, using a standard for industry application, IAPWS-IF97 standard [157].

IAPWS-IF97 covers thermodynamic properties for water and steam in following range:

$$273.15 \text{ K} < T < 1073.15 \text{ K}, \; p \leq 100 \text{ MPa} \tag{14.105}$$

$$1073.15 \text{ K} < T < 2273.15 \text{ K}, \; p \leq 50 \text{ MPa} \tag{14.106}$$

Figure 14.2 shows the five regions defined in IAPWS-IF97. Region 1 represents the liquid phase. Region 2 describes the vapor phase. Region 4 is the saturation curve that separates the liquid phase and the vapor phase. Region 3 describes water properties near the critical point. Region 5 is used for very high temperature condition and is not of interest to any reactor operation; thus region 5 is not included in the BISON coolant channel model.

Ref [157] describes the equations used in the calculation of thermodynamic properties using basic equations which are functions of temperature and/or pressure or temperature and density.

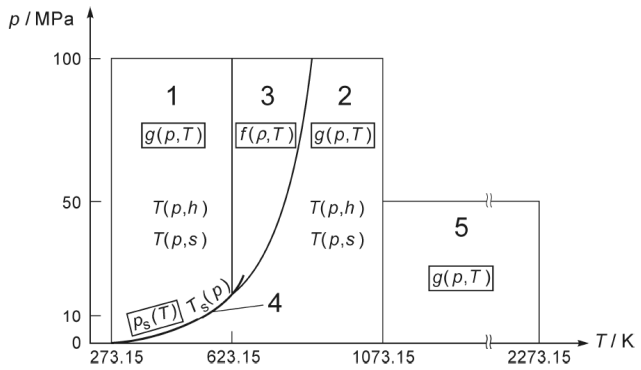

Figure 14.2: Regions and Equations of IAPWS-IF97 [157]

Viscosity and thermal conductivity of water and steam are functions of density and temperature; these transport properties are implemented based on the information in [158] and [159]. Surface tension of water as a function of temperature is given in [160].

These physical properties are used together with IAPWS-IF97 standard in evaluating properties for water and steam.

14.8 Sodium Coolant

Sodium coolant for fast reactors can also be simulated in BISON. The model uses the same framework as the above calculations for water/steam, but with an appropriate correlation for liquid sodium. The model uses the modified Schad correlation

$$Nu = 4.496\left(-16.15 + 24.96\left(\frac{P}{D}\right) - 8.55\left(\frac{P}{D}\right)^2\right)\frac{Pe}{150}^{0.3} \tag{14.107}$$

where

$Nu \equiv hD/k$ is the Nusselt number

$Pe \equiv Re\,Pr$ is the Peclet number

P/D is the pitch-to-diameter ratio

Sodium properties are taken from the ANL/RE-92/2 report [161]:

$$k = 124.67 - 0.11381T + 5.5226\cdot 10^{-5}T^2 - 1.1842\cdot 10^{-8}T^3 \tag{14.108}$$

$$H = -365770 + 1658.2T - 0.42395T^2 + 1.4847\cdot 10^{-4}T^3 + 2992600/T \tag{14.109}$$

where k is thermal conductivity, H is enthalpy, and units are SI.

15 Cladding Corrosion Model

15.1 Zirconium Alloy at Normal Operating Temperatures

15.1.1 Introduction

Zirconium alloy cladding can have an exothermic reaction with coolant water which converts metal to oxide at the cladding outer surface:

$$Zr + H_2O \rightarrow ZrO_2 + 2H_2 + 6.5 \times 10^6 \text{ J/kgZr} \tag{15.1}$$

Such an oxidation process, which is referred to as water-side corrosion, is a fundamental aspect of LWR fuel performance. The resultant oxide film on the outer surface of cladding can affect both the thermal and mechanical properties of cladding. Because of the lower thermal conductivity of zirconium oxide in comparison with zirconium alloys, the oxidation of the cladding adds to thermal resistance to heat transfer from the fuel to the coolant. Zirconium oxide is a brittle material and can be easily cracked. Thus it is expected that the mechanical strength of cladding is mainly determined by the metallic wall, which is thinned after corrosion. Concurrent to the oxidation process, a fraction of hydrogen can be absorbed into the metal and can diffuse under the influences of both temperature and stress. Due to the low solubility of hydrogen in zirconium and its alloys, hydrogen can precipitate as δ-phase hydrides ($ZrH_{1.66}$), which are known to further reduce the ductility of irradiated cladding material. In fact, the hydrogen content in the zircaloy cladding has become a limiting parameter for burnup extension of LWR fuel. An oxidation model which can predict the growth of oxide layer as a function of operation conditions and metallurgical variables of cladding materials is essential to the study of LWR fuel performance. In addition, it is also of interest to account for the effects of the oxide layer on the thermal and mechanical properties of cladding.

Low temperature (250 ^{o}C/ 523 K to 400 ^{o}C/ 673 K) oxidation is calculated considering that cladding oxidation under normal LWR conditions occurs in two stages: a pre-transition oxidation process that follows a cubic time dependence up to a transition oxide thickness, and a post-transition process that follows a linear time dependence. The transition between the two stages typically occurs at 2 micron.

For the pre-transition period, the corrosion rate is given by an Arrhenius equation [162]:

$$\frac{dS^3}{dt} = C_1 \exp\left(\frac{-Q_1}{RT_I}\right), \text{ for } S \leq S_{trans}. \tag{15.2}$$

For the post-transition period, the corrosion rate is given by [162]:

$$\frac{dS}{dt} = C_2 \exp\left(\frac{-Q_2}{RT_I}\right), \text{ for } S > S_{trans} \tag{15.3}$$

where

S is the oxide thickness

T_I is the metal-oxide interface temperature

C_1 is the rate constant for pre-transition oxidation

Q_1 is the activation energy for pre-transition oxidation

C_2 is the rate constant for post-transition oxidation

Q_2 is the activation energy for post-transition oxidation

R is the universal gas constant

S_{trans} is the transition oxide thickness

The metal-oxide interface temperature, T_I, is calculated assuming steady-state heat conduction across the oxide thickness as:

$$T_I = T_{co} + \frac{q'' S}{k_{ox}} \tag{15.4}$$

where T_{co} is the outer surface (waterside) oxide temperature and k_{ox} is thermal conductivity of zirconium oxide.

In most BISON simulations, the oxide layer is not meshed independently. Instead, the oxide layer is modeled as a virtual layer within the clad, and the code keeps track of the thickness S, as shown in Figure 15.1. Since the oxide causes a larger temperature jump than would be caused by the same thickness of metal, T_{co} calculated by BISON does not correspond to the true temperature at the coolant-clad interface. Therefore, we must modify the heat transfer coefficient so that the driving force $h(T_{co} - T_b)$ (T_b is the bulk coolant temperature) is correct.

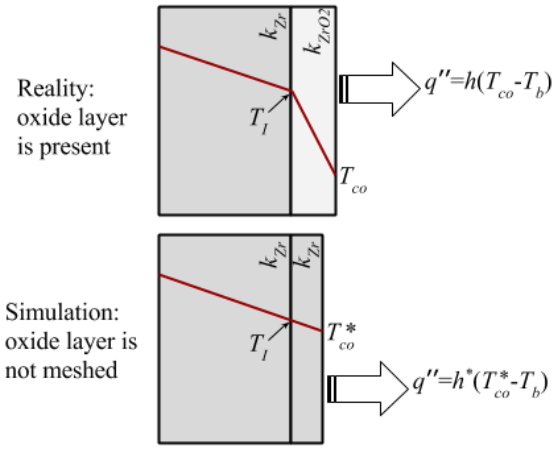

Figure 15.1: Diagram showing how BISON accounts for the temperature jump across the oxide without explicitly meshing the oxide layer. The red lines indicate temperature profiles.

In this approach, zircaloy material is used in the thermal solution while an effective heat transfer coefficient is used to compute a "fictitious" boundary condition to match the true temperature

at the metal and oxide interface. We begin with two equivalent statements for heat flux into the coolant

$$q'' = h(T_{co} - T_b) \tag{15.5}$$
$$q'' = h^*(T^*_{co} - T_b) \tag{15.6}$$

where h is the true heat transfer coefficient. The starred values T^*_{co} and h^* are the simulated (fictitious) temperature of the oxide surface (waterside) and corresponding effective heat transfer coefficient, respectively. The temperature at the interface between the oxide and metal must also match:

$$T_I = T_{co} + \frac{q''}{k_{ZrO_2}} S \tag{15.7}$$
$$T_I = T^*_{co} + \frac{q''}{k_{Zr}} \frac{S}{R_{PB}} \tag{15.8}$$

where

T_I is the temperature at the interface of the oxide and metal
k_{Zr} is the thermal conductivity of zirconium alloy
k_{ZrO_2} is the thermal conductivity of zirconium oxide
R_{PB} is the Pilling-Bedworth ratio

These equations can be combined to eliminate T_I and T^*_{co}

$$h^* = \frac{q''}{T_{co} - T_b + q''(\frac{S}{k_{ZrO_2}} - \frac{S}{k_{Zr}R_{PB}})} \tag{15.9}$$
$$= \frac{1}{\frac{1}{h} + S(\frac{1}{k_{ZrO_2}} - \frac{1}{k_{Zr}R_{PB}})} \tag{15.10}$$
$$= \frac{h}{1 + \frac{hS}{k_{Zr}R_{PB}}(\frac{k_{Zr}}{k_{ZrO_2}} - 1)} \tag{15.11}$$

The oxide growth calculation requires T_{co}, which can be calculated directly from T^*_{co} by

$$T_{co} = T^*_{co} + q''S\left(\frac{1}{k_{Zr}R_{PB}} - \frac{1}{k_{ZrO_2}}\right) \tag{15.12}$$

15.1.2 EPRI KWU CE Model

For normal operating temperatures below 673 K, the EPRI/KWU/C-E oxidation model [163, 164] is used as the default corrosion model. The formulation is analogous to that described in (Eqs. 15.2 and 15.3), with [163, 164]:

$C_1 = 6.3 \times 10^9$ μm^3/day
$Q_1/R = 16266$ K
$C_2 = 8.04 \cdot 10^7 + 2.59 \cdot 10^8 \cdot \left(7.46 \cdot 10^{-15} \cdot \phi\right)^{0.25}$ μm^3/day

$Q_2/R = 13775$ K

where ϕ is the fast neutron flux in n/cm^{2}s. C_2 accounts for the irradiation enhancement to corrosion.

15.1.3 EPRI SLI Model

The EPRI/SLI model is also implemented in BISON code for modeling of the corrosion of PWR fuel cladding materials. This model uses enhancement factors on C_1 and C_2. For the pre-transition period, C_1 is multiplied by two factors, one related to the lithium concentration in the coolant and the other related to the iron concentration in the cladding. These are given as [165]

$$C_1 = C_{10} F_{Li}(1 + F_{Fe}) \tag{15.13}$$

$$F_{Li} = \exp\left(C_{Li}(0.12[Li] - 23[Li]/T)\right) \tag{15.14}$$

$$F_{Fe} = C_{Fe}[Fe] \tag{15.15}$$

where $[Li]$ = lithium concentration [ppm] in the coolant, and $[Fe]$ = fraction of iron particles dissolved (%) for a given initial particle size distribution. The parameters used in above equations are as follows:

C_{10}=5.876 $\times 10^{10}\mu$m^3/day
Q_1=33662.7 cal/mol
C_{Li}=0.65
C_{Fe}=0.02(%)$^{-1}$

The post-transition coefficient C_2, is multiplied by several enhancement coefficients as follows:

$$C_2 = C_{20} F_{Li} F_{Sn} F_{Q/A}(1 + F_H + F_{Fe} + F_\phi) \tag{15.16}$$

where C_{20} = 7.619$\times$ $10^6\mu$m/day
The coolant chemistry (LiOH) enhancement factor is given by:

$$F_{Li} = \exp(C_{Li}(0.17[Li] - 20.4[Li]/T_I)) \tag{15.17}$$

The cladding tin content enhancement factor is given by:

$$F_{Sn} = \begin{cases} 1.25(\text{Sn} - 1.38) + 1.0 & \text{for Sn} \leq 1.38 \text{ wt\%} \\ 0.75(\text{Sn} - 1.38) + 1.0 & \text{for Sn} > 1.38 \text{ wt\%} \end{cases} \tag{15.18}$$

where Sn is tin content of cladding in (wt%). The heat flux normalization factor is given by:

$$F_{Q/A} = 1 + 0.0881(Q/A)/100 \tag{15.19}$$

where Q/A (W/cm^2) is the heat flux at cladding outer surface.

The hydrogen redistribution enhancement factor is:

$$F_H = \begin{cases} 0 & \text{for} \quad [H_2] < 400 \text{ ppm} \\ 0.699 ln([H_2]/400) & \text{for} \quad 18811.25 \text{ ppm} \geq [H_2] \geq 400 \text{ ppm} \\ 2.691 & \text{for} \quad [H_2] > 18811.25 \text{ ppm} \end{cases} \tag{15.20}$$

where $[H_2]$ = cold side hydrogen content in the cladding metal-oxide interface.

The fast neutron flux enhancement factor is:

$$F_\phi = C_\phi \phi^{Po} \tag{15.21}$$

where ϕ = fast flux (E $>$ 1 MeV, n/cm^2-s), C_ϕ = 1.2 $\times 10^{-4}$ (n/cm^2-s)$^{-0.24}$, and Po = 0.24.

The iron enhancement factor is defined by Eq. 15.15.

Activiation energy in the post-transition period is found to be dependent on hydrogen content [166]:

$$Q_2 = \begin{cases} Q_{2L} & \text{for} \quad [H_2] < 400 \text{ ppm} \\ (Q_{2U} - Q_{2L})F_H/F_{HU} + Q_{2L} & \text{for} \quad 18811.25 \text{ ppm} \geq [H_2] \geq 400 \text{ ppm} \\ Q_{2U} & \text{for} \quad [H_2] > 18811.25 \text{ ppm} \end{cases} \tag{15.22}$$

where F_{HU} = hydrogen enhancement factor at hydride rim ($[H_2]$ = 18811.25 ppm), Q_{2L} = 24825 cal/mol, and Q_{2U} = 9135.6 cal/mol.

15.1.4 Zirconium Oxide Thermal Conductivity

Thermal conductivity of zirconia in the model is a constant value of 1.5 W/m-K for PWR applications [165]. However the reported value of zirconium oxide thermal conductivity varies greatly from different sources.

In the NFIR experimental program, the ZrO_2 thermal conductivity was estimated using cladding elongation measurements during power ramps as a representation of cladding temperature changes [167]. By comparing the cladding elongation of a fuel rod with an external oxide to a reference rod without an external oxide, the thermal impact of the oxide layer was determined. Experiments were performed at oxide layer thicknesses between 30 and 82 μm. In determining the thermal conductivity from the measured data, considerations were made for external crud layers, power increases, power decreases, and oxide layer thickness. The results of the experiments found that the thermal conductivity of ZrO_2 is independent of oxide thickness and temperature in the temperature range between 240°C and 300°C. An NFIR corrosion model was developed with a constant thermal conductivity value of 2.7 W/m-K (which tends to be on the high side of the data). The NFIR model is based on a series of in-pile experiments performed in the Halden test reactor that were designed to determine the thermal conductivity of external oxide layers on fuel rods [167].

The MATPRO-11 Rev. 2 model for Zircaloy oxide thermal conductivity is based on several different data sources of thermal conductivity measurements [39]. These measurements were performed using a variety of oxide morphologies (stabilized oxides, nodular, and black) and oxide formation techniques (steam oxidation and plasma sputtering).

Using thermal diffusivity measurements, the thermal conductivity was determined for the different oxide types as a function of temperature. The MATPRO model used primarily data from tests with black oxide layers to develop the thermal conductivity as a function of temperature [39].

The resultant correlation is

$$k_{ox} = 0.835 + 1.81 \times 10^{-4} T \tag{15.23}$$

where k_{ox} is the oxide thermal conductivity (W/m-K) T is the oxide temperature (K).

The correlation above is applicable to solid Zircaloy oxide found on fuel rods. These other values are typical of other models found in the literature. Further information on the MATPRO Zircaloy oxide model can be found in Reference [39].

Nuclear Electric (NE PLC) use a different correlation starting at a value of 1.5 W/m-K. The value then decreases with oxide thickness according to the following relationship [165]:

$$k_{ox} = \begin{cases} 1.5, & 0\,\mu\text{m} < S \leq 48\,\mu\text{m} \\ 3.48 - 0.0412S, & 48\,\mu\text{m} < S \leq 65\,\mu\text{m} \\ 0.8, & S > 65\,\mu\text{m} \end{cases} \tag{15.24}$$

The CEA Cochise code uses a constant value of 1.6 W/m-K [165].

15.1.5 Numerical Method

Numerical solution of the oxide thickness growth consists of pre-transition and post-transition period.

In the pre-transition period:

$$\Delta S = \sqrt[3]{C_1 \exp\left(\frac{-Q_1}{RT_{co}}\right)\Delta t + S} \tag{15.25}$$

where

S is oxide thickness at previous time step (μm)
C_1 is rate constant for pre-transition oxidation (μm^3/day)
Q_1 is activation energy for pre-transition oxidation (cal/mol)
R is gas constant = 1.987 (cal/mol-K)
T_{co} is cladding outer surface temperature (K)
Δt is time increment (day)
ΔS is oxide thickness increment (μm)

In the post-transition oxidation period, an approximate integral method is used [163] to account for the metal-oxide interface temperature change on the oxygen weight gain:

$$\Delta S = \gamma \Delta W / 100 \tag{15.26}$$

$$\Delta W = \frac{RT_{co}^2 k_{ox}}{\gamma Q_2 q''} \ln\left[1 - \frac{\gamma Q_2 q''}{RT_{co}^2 k_{ox}} k_0 \exp\left(-\frac{Q_2}{RT_{co}}\right) \exp\left(\frac{\gamma Q_2 q'' W}{RT_{co}^2 k_{ox}}\right)\right] \tag{15.27}$$

where

T_{co} is cladding outer surface temperature (K)
k_{ox} is thermal conductivity of zirconium oxide (W/cm-K)
ΔW is weight gain (g/cm ^{2})
γ (=0.6789 cm^3/g) is a factor that converts weight gain (g/cm^2) to thickness (cm)
Q_2 is activation energy for post-transition phase
q is heat flux (W/cm^2)

k_0 is rate constant for post-transition phase (g/cm^2-day)
Δt is time increment (day)
R is ideal gas constant = 1.987 (cal/mol-K)
W is weight gain at previous time step (g/cm^2)
S is oxide layer thickness at previous time step (μm)

15.2 Zirconium Alloy at High Temperature `[OxidationCladding]`

In the high temperature range (e.g., accident situations) the coolant has become steam, and oxidation proceeds much more rapidly than at normal LWR operating temperatures. Under these conditions, the kinetics of oxide scale growth and oxygen mass gain in the cladding can be described by a parabolic law, with the reaction rate constant defined as a function of the temperature through an Arrhenius relation [168]

$$\frac{d\xi^2}{dt} = A \exp\left(\frac{-Q}{RT_I}\right) \tag{15.28}$$

where
ξ is either the oxide scale thickness, ξ=S (m), or the oxygen mass, ξ=g (kg·m^{-2})
T_I is the metal-oxide interface temperature (K)
A is the oxidation rate constant (m or kg·m^{-2})
Q is the activation energy (J/mol)
R is the universal gas constant (J/mol-K)

Following the recommendations in [168], the BISON model includes correlations for oxide scale growth and oxygen mass gain rates in Zircaloy-2/4 appropriate to different temperature ranges. In particular, the following approach is adopted.

- For metal-oxide interface temperatures from 673 K up to 1800 K, the Leistikov [169] correlation is used. The Cathcart-Pawel correlation [170] is also available and can be chosen as an option. The Leistikov correlation has been selected as reference in view of the larger underlying database, the availability of experimentally determined mass gain for all tests, and the better fit for lower temperature relative to the Cathcart-Pawel correlation [168].
- Above 1900 K, the Prater-Courtright correlation [171] is used.
- Between 1800 and 1900 K, a linear interpolation is made. Linear interpolation between two correlations of Arrhenius type is obtained by a third correlation of the same type [168].

The values of the parameters in Eq. 15.28 relative to the different correlations are given in Table 15.1.

Table 15.1: Parameters of the correlations for oxide scale (S) and oxigen mass gain (g) at high temperature [168].

Correlation	A_S (m^2s^{-1})	Q_S/R (K)	A_g ($kg{\cdot}m^{-2}$)	Q_g/R (K)
Leistikov	7.82×10^{-6}	20214	52.42	20962
Cathcart-Pawel	2.25×10^{-6}	18062	36.22	20100
Prater-Courtright	2.98×10^{-3}	28420	3.3×10^{3}	26440

15.3 Aluminum

According to [172, 173], corrosion of aluminum in ATR follows

$$t_{ox} = 0.7\cdot 25.4\cdot 443\cdot \theta^{0.778}\exp(-4600/T) \tag{15.29}$$

where

t_{ox} is the oxide thickness (μm)

θ is time (hours)

T is temperature (K)

This corrosion thickness may be used in the coolant channel model.

15.4 FCCI Interaction Layer Thickness `[ThicknessLayerFCCI]`

For metal fuel, the Fuel-Clad Chemical Interaction layer develops as fission products diffuse from the fuel into the cladding. During long transients, such as burnup simulations, an interaction layer develops in the clad. In BISON, the change in thickness layer is tracked similar to the approach used in [24]. Two methods are provided to related mass flux at a boundary to interaction layer growth.

The first method is adapted from [174] to be a change in layer thickness. The interaction layer thickness was given as

$$J = \frac{\delta\rho}{MWt} \tag{15.30}$$

where J is the mass flux through the boundary, δ is the interaction layer thickness at time t, ρ is the density of the layer, and MW is the molecular weight of the layer. Eq. 15.30 may be easily arranged into a change in thickness, $\Delta\delta$, relation assuming the mass flux is constant over the Δt giving

$$\Delta\delta = J\frac{MW}{\rho}\Delta t \tag{15.31}$$

assuming the thickness layer growth is the same direction of the mass flux according to the boundary normal.

The second method is provided from [175] relating the movement of the boundary between two diffusion couples to the mass flux across the boundary. The relation is given as

$$(C - C_f)\frac{d\delta}{dt} = D\left.\frac{\partial C}{\partial x}\right|_{x=\delta} \tag{15.32}$$

where C is the solubility fraction of the fission product, C_f is the solubility limit of the fission product in the fuel, and the right side terms are the mass flux across the boundary. As the fuel is producing fission products the boundary moves in the opposite direction than in diffusion couples. As long as the solubility fraction remains above the fuel solubility limit, the change in thickness is

$$\frac{d\delta}{dt} = \frac{J}{C - C_f} \tag{15.33}$$

assuming the thickness layer growth is the same direction of the mass flux according to the boundary normal.

15.5 FCCI Eutectic Penetration Thickness `[EutecticThicknessFCCI]`

For metal fuel, a Fuel-Clad Chemical Interaction eutectic may form and melt when the temperature is above the eutectic melting temperature. The formation and melt front then move through the cladding, which thins the clad weakening it. This usually occurs during shorter transients, such as TOP events. In BISON, the penetration thickness of this eutectic melt is tracked similar to the approach used in [24]. However, instead of using a diffusion coefficient, which can already be accomplished in BISON, this module relates temperature to penetration rate taken from [176] as

$$\dot{r}\,[\mu\mathrm{m/s}] = e^{22.847 - 27624/T} \tag{15.34}$$

where $\dot{r}$ is the eutectic penetration rate reported in micrometers per second and T is the temperature in Kelvin. Between 1353.15 K and 1506.15 K, the penetration rate becomes

$$\dot{r}\,[\mu\mathrm{m/s}] = 922 + 2.9265\,(T - 1388) - 0.21522\,(T - 1388)^2 + 0.0011338\,(T - 1388)^3 \tag{15.35}$$

which accounts for the melting of the protective UFe_2 layer. The eutectic only penetrates if the temperature is above the melting point usually taken as 988.15 K. BISON converts the rate to meters per second and provides a unit factor which multiplies this rate. The units or scaling may be adjusted using this unit factor. The rate is multiplied by the time step size and added to the current penetration thickness.

16 Zirconium Redistribution in U-Pu-Zr

Zirconium redistribution in U-Zr and U-Pu-Zr based fuels is important for both fuel integrity and thermal limits. As zirconium redistributes, the uranium moves in the opposite direction and what was once a uniform isotopic concentration across the fuel rod becomes concentrated in zirconium, primarily at rod center and rod edge. This preferential accumulation at rod edge and rod center, with a corresponding decrease in the central region can affect local thermal limits (margin to melting temperature for example), radial power peaking, with potential enhances to lanthanide and actinide migration, all due to a significantly varying radial isotopic composition. A strong understanding of this process along with a robust method for predicting zirconium concentrations is vital to advanced metallic fuel designs, particularly those designs with minor actinide loadings, lanthanide loadings and new proposed metallic alloys.

16.1 Background

The prediction of zirconium redistribution is difficult for several reasons. First, fuel behavior under irradiation is a multi-physics, multi-scale problem that requires the coupling of neutronic solutions due to uranium migration which induces radial power peaking. Correspondingly, burnup effects in the fuel cause changes in both power and the thermo-mechanical-diffusion fuel behavior. Additionally there are thermal considerations primarily related to thermal conductivity; as zirconium migrates, the thermal conductivity changes inversely with zirconium concentration - an increase in zirconium concentration causing a decrease in thermal conductivity and vice-versa. Fuel burnup increases porosity in the fuel, which degrades thermal conductivity. However, near the rod edge liquid sodium infiltration due to fuel cracking can occur, causing some recovery of the degraded conductivity. This porosity itself appears to be phase-dependent, particularly in the beta phase region of the fuel where porosity appears to be at a minimum and thermal conductivity degradation is expected to be lower. Along with neutronic and thermal-mechanical concerns, the phase properties of the fuel and our fundamental understanding of fuel properties and fuel behavior, particularly U-Pu-Zr based fuel, is not well known.

The microstructure of irradiated U-Pu-Zr fuel exhibits three distinct concentric zones where the effective heat of transport drives the direction of zirconium migration atoms in different phases: a zirconium-enriched central zone, a zirconium-depleted and uranium-enriched intermediate zone, and a zirconium-enriched zone on the outer periphery. Phase-dependent diffusion coefficients and heats of transport are not well known, with early evidence indicating the phase transition temperatures, experimentally derived from fresh fuel, may not be consistent with irradiated fuel. Final considerations are related to the phase diagram itself. Figure 16.1 below shows the experimentally derived phase diagram for U-19Pu-10Zr fuel from [177, 178]. Noting the complexity and difficulty associated with programming logic for such a diagram, along

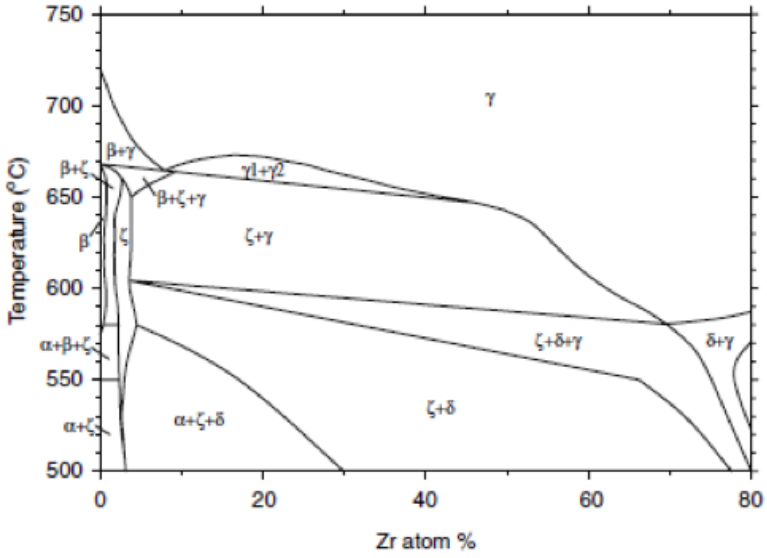

Figure 16.1: Pseudo-binary (U-Pu)-Zr phase diagram with Pu content fixed at 19 wt% [178, 179].

with the lack of any material property information for several of the phases, a simplified version based on those used in several other models [46, 177, 178] was used in practice, shown here in Figure 16.2.

There have been several published papers that analyze constituent distribution in metallic fuels mechanistically for U-Zr and U-Pu-Zr fuels [46, 177, 178, 180, 179]. In the most recent paper published by Kim et al. [178], a new computational model was developed to solve the diffusion equations using a simplified pseudo-binary phase diagram (similar to Figure 16.2). The model was in one dimension and the diffusion equation was not solved simultaneously with the thermal conduction equation due to the difficulties encountered in predicting the experimental data. In order to predict the location of the phase transitions correctly an artificial temperature gradient was imposed as a boundary condition and phasic diffusion coefficients were evaluated to match the data. However, the imposed temperature profile resulted in an unphysical heat flux that is not consistent with the operator-declared linear heating rate. The use of reported enthalpies of solution and the simplified phase diagram have inconsistencies. Karahan [46] repeated aspects of earlier work by Kim et al. [177, 178], aiming to develop an improved capability but used the same artificial temperature boundary condition in their validation of FEAST metallic fuel code [46].

Our model, as we will summarize in the next section and published previously [64] is similar to the models from [177, 178, 179], but several significant differences are listed here. Our model corrects an inconsistency between the enthalpies of solution and the solubility limit curves of the phase diagram. It also adds an artificial diffusion term when in the 2-phase regime that stabilizes

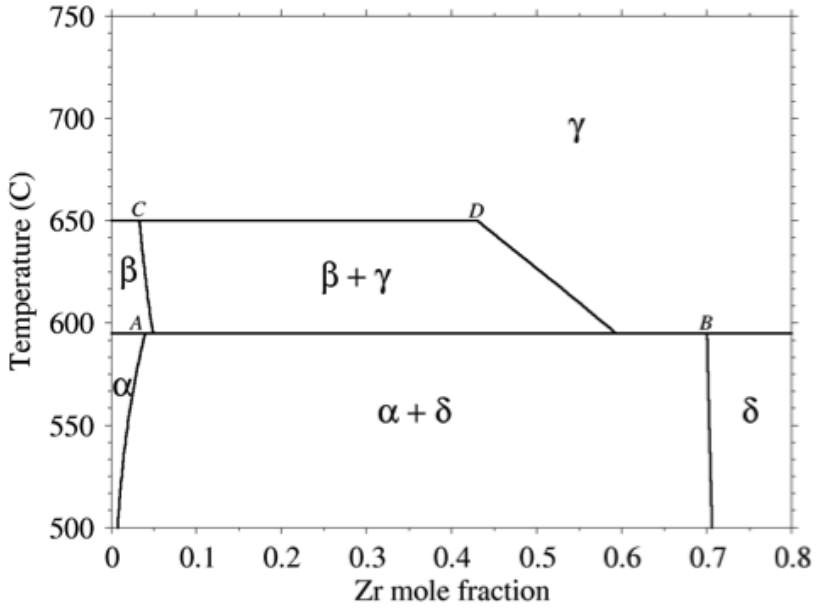

Figure 16.2: Simplified pseudo-binary (U-Pu)-Zr phase diagram used in BISON model.

the standard Galerkin FE method used by BISON [181]. Another improvement made is in the formulation of the zirconium flux. The Soret diffusion term used in the previous metallic codes includes a zirconium concentration multiplied by the sum of heat of reaction and enthalpies of solution. To ensure a physical zirconium mole fraction, in the presence of a fixed plutonium mole fraction, it is necessary that the zirconium flux tend to 0 as the concentration of zirconium tends to either limiting value (0 or 1, less the plutonium mole fraction). This is true for the lower limit (0), but not the upper limit (1). To address this issue we introduced an additional factor into the Soret term coefficient. With these new modifications we first reanalyze the data taken from rod T179 [177, 178] of EBR-II to revaluate the previously recommended diffusion coefficients. This is important in two aspects. First, we have an experimental program measuring diffusion coefficients from diffusion-coupled experiments. The predictions reported in this manual may be validated with the diffusion-coupled data to provide a better predictive capability. Secondly, the use of a better-validated coupled solution will provide greater confidence in the design of advanced fuels. Therefore, we believe the formulation and framework presented in this manual are credible and represent a significant improvement relative to previous work. The model we presented below is primarily sourced from the paper by Galloway et al. [64]. While the constituent redistribution model we discussed below is given for U-Pu-Zr fuels, it is equally applicable to U-Zr fuels, albeit with different material properties. This is because of the EBR data which showed no significant redistribution of Pu in ternary U-Pu-Zr fuels. Thus, the model for U-Pu-Zr fuels assumes Zr moves in U only while Pu is not mobile in U or Zr. Therefore,

the mathematical model and numerical implementation of it are valid for U-Zr fuels. The only difference between these two fuel types is the use of different phase diagrams and property models. Thermal conductivity of fresh U-Zr is already described in the property description in this Section 8.10.1 for both U-Zr and U-Pu-Zr fuels.

16.2 Constituent Redistribution Model

In this section we present a model [64] of constituent migration in U-Pu-Zr fuel. It is a refinement of an earlier model [182] that was based on the model developed by [183] for U-Zr nuclear fuel and later used in [177, 178] in a pseudo-binary study of U-Pu-Zr fuel. Similar models are considered in [46, 179]. These models adapt the original work of [184] in the approach to 2-phase regions.

16.2.1 Binary constituent redistribution model

We begin by considering a binary substitutional alloy, U-Zr for definiteness. Let c_0 be the density of lattice sites, which for simplicity we will assume is independent of composition and temperature, and let x_{Zr}, $x_{\mathrm{U}} \geq 0$, and $x_{\mathrm{Zr}} + x_{\mathrm{U}} = 1$ be the atomic fractions of zirconium and uranium. In the presence of thermal gradients, the Zr atom flux in a single-phase region is,

$$\mathbf{J}_{\mathrm{Zr}} = -c_0 D(\nabla x_{\mathrm{Zr}} + S\nabla T), \tag{16.1}$$

where D is the interdiffusion coefficient of Zr in the phase. The term involving ∇T is the so-called Soret effect or thermodiffusion. The coefficient $S(x_{\mathrm{Zr}}, T)$ may be positive or negative. This term contributes an advective component to the Zr flux directed toward lower temperatures when positive and higher temperatures when negative. To ensure physical compositions, i.e. $0 \leq x_{\mathrm{Zr}} \leq 1$, the flux $\mathbf{J}_{\mathrm{Zr}}$ must tend to 0 as x_{Zr} tends to either 0 or 1. This leads us to take as a leading order approximation,

$$S = x_{\mathrm{Zr}}(1 - x_{\mathrm{Zr}})\frac{Q^\star}{RT^2}. \tag{16.2}$$

where $Q^\star$ is the heat of transport of Zr in the phase and R is the gas constant. In the dilute limit $x_{\mathrm{Zr}} \ll 1$, we recover the usual form $S = x_{\mathrm{Zr}}Q^\star/RT^2$ used in previous models. The additional factor $1 - x_{\mathrm{Zr}}$ ensures that $x_{\mathrm{Zr}} \leq 1$. Thus in a single-phase region the Zr flux is:

$$\mathbf{J}_{\mathrm{Zr}} = -c_0 D\left(\nabla x_{\mathrm{Zr}} + x_{\mathrm{Zr}}(1 - x_{\mathrm{Zr}})\frac{Q^\star}{RT^2}\nabla T\right), \tag{16.3}$$

where D and $Q^\star$ are coefficients associated with the phase. It is important to recognize that the usual form of S proportional to x_{Zr} alone is not a fundamental law, but is itself merely a leading order approximation that is only valid for small x_{Zr}. This can be seen in two ways. First, as just noted, it gives a non-zero flux when $x_{\mathrm{Zr}} = 1$ that leads to unphysical solutions with $x_{\mathrm{Zr}} > 1$. Second, S and its approximations should exhibit a certain symmetry. The problem could just as well be posed in terms of x_{U} with the U flux $\mathbf{J}_{\mathrm{U}}$ given by an expression analogous to Equation 16.1. On the other hand $\mathbf{J}_{\mathrm{U}} = -\mathbf{J}_{\mathrm{Zr}}$. Both should lead to the same flux, and reconciling

the two leads to the symmetry. Our approximation Equation 16.2 exhibits this symmetry, and the necessary asymptotic behavior, while the usual form does not.

Next consider the flux in a 2-phase region very near a solubility curve defined by $x_{\mathrm{Zr}} = X(T)$. For $x_{\mathrm{Zr}} \leq X(T)$ suppose the alloy is single-phase, but for $x_{\mathrm{Zr}} > X(T)$ a second Zr-rich precipitant phase appears. Following [184] we will assume that a local equilibrium between the two phases is maintained at each point in a temperature gradient through rapid adjustment of the phase fractions via local diffusion processes. This means the composition of the major continuous phase is fixed, $x_{\mathrm{Zr}} = X(T)$ and as a consequence,

$$\nabla x_{\mathrm{Zr}} = X'(T)\nabla T. \tag{16.4}$$

Assuming that the flux of Zr (or counter flux of U) occurs only through the continuous phase, we then have,

$$\mathbf{J}_{\mathrm{Zr}} = -c_0 D\left(X'(T) + X(T)(1-X(T))\frac{Q^\star}{RT^2}\right)\nabla T, \tag{16.5}$$

where D and $Q^\star$ are the coefficients associated with the continuous phase. For simplicity we consider solubility curves $X(T)$ satisfying,

$$\frac{dX}{dT} = X(1-X)\frac{\Delta H}{RT^2}, \quad X(T_0) = X_0, \tag{16.6}$$

where ΔH, X_0, and T_0 are constant model parameters. Note that this equation uniquely determines the solubility curve. With this choice Equation 16.5 becomes,

$$\mathbf{J}_{\mathrm{Zr}} = -c_0 D X(T)(1-X(T))\frac{\Delta H + Q^\star}{RT^2}\nabla T. \tag{16.7}$$

This approach mimics [184] who took, in the dilute limit $x_{\mathrm{Zr}} \ll 1$,

$$\frac{dX}{dT} = X\frac{\Delta H}{RT^2}. \tag{16.8}$$

The models developed in [46, 177, 178] also adopted this approach, but the expressions they use for ΔH are inconsistent with their phase diagrams, and have the wrong sign in several cases. If one desires to use arbitrary solubility curves, then equation Equation 16.5 must be used for the flux.

The mirror situation where the alloy is single phase for $x_{\mathrm{Zr}} \geq X(T)$and two-phase for $x_{\mathrm{Zr}} < X(T)$ is precisely the same. The Zr flux in the two-phase region very near the solubility curve $X(T)$ is also given by Equation 16.7 when $X(T)$ is of the form Equation 16.6, with the coefficients D and $Q^\star$ associated with the continuous phase.

16.2.2 Constituent migration model for U-Pu-Zr

For U-Pu-Zr fuel it has been argued that a pseudo-binary treatment, in which the Pu fraction is assumed fixed, is justified both theoretically and on the basis of experimental data that show the Pu is largely immobile [177, 178]. Thus we consider a ternary U-Pu-Zr alloy where the Pu fraction is a fixed, spatially uniform value x_{Pu}. As in a true binary alloy, the remaining U and

Zr constituents flow counter to each other, and if we set $\tilde{x}_{\mathrm{Zr}} = x_{\mathrm{Zr}}/(1-x_{\mathrm{Pu}})$ we may apply the preceding binary model to the relative Zr atom fraction $\tilde{x}_{\mathrm{Zr}}$. Expressing the result in terms of the original ternary atom fraction x_{Zr} we obtain,

$$\mathbf{J}_{\mathrm{Zr}} = -c_0 D \left(\nabla x_{\mathrm{Zr}} + \frac{x_{\mathrm{Zr}}(1-x_{\mathrm{Pu}}-x_{\mathrm{Zr}})}{1-x_{\mathrm{Pu}}} \frac{Q^\star}{RT^2} \nabla T \right), \tag{16.9}$$

for the Zr flux in a single-phase region, where the coefficients D and $Q^\star$are associated with the phase, and,

$$\mathbf{J}_{\mathrm{Zr}} = -c_0 D \left(\frac{X(T)(1-x_{\mathrm{Pu}}-X(T))}{1-x_{\mathrm{Pu}}} \right) \left(\frac{\Delta H + Q^\star}{RT^2} \right) \nabla T, \tag{16.10}$$

for the flux in a 2-phase region very near the solubility curve $x_{\mathrm{Zr}} = X(T)$, where the coefficients D and $Q^\star$ are those associated with the continuous phase. The solubility curves are chosen to satisfy,

$$\frac{dX}{dT} = \frac{X(1-x_{\mathrm{Pu}}-X)}{1-x_{\mathrm{Pu}}} \frac{\Delta H}{RT^2}, \quad X(T_0) = X_0, \tag{16.11}$$

for some choice of parameters ΔH, X_0, and T_0, which has the solution:

$$X(T) = (1-x_{\mathrm{Pu}}) \left\{ 1 + \frac{1-x_{\mathrm{Pu}}-X_0}{X_0} \exp\left[\frac{\Delta H}{R} \left(\frac{1}{T} - \frac{1}{T_0} \right) \right] \right\}^{-1}. \tag{16.12}$$

We use the simple pseudo-binary U-19Pu-Zr phase diagram shown in Figure 16.2 which is based on the phase diagrams used in [46, 177, 178]. There are two 2-phase regions, $\alpha+\delta$ and $\beta+\gamma$, depending on the temperature range. The nominal transition temperatures are $T_\alpha = 595$ C and $T_\beta = 650$ C, but these two values were varied in the simulations presented in this manual. The parameters defining the solubility curves are given in Table 16.1.

Table 16.1: Parameters used in simplified phase diagram from Figure 16.2.

Phase/Point	X_0 (solubility intersection)	T_0 ($^\circ$ C) (upper transition)	ΔH (kJ/mol)
α/A	0.04	595	100
δ/B	0.70	595	-3
β/C	0.033	650	100
γ/D	0.43	650	100

The 2-phase flux Equation 16.10 only applies very near a solubility curve and supposes that all the flux occurs through the major continuous phase, ignoring the precipitant phase. This is a reasonable assumption near a solubility limit, but we need an expression for the flux that spans the entire 2-phase region from the Zr-poor phase solubility limit to the Zr-rich phase solubility limit. For this we use a simple weighted average of the two fluxes that apply near the solubility

limits. For the + region we take:

$$\begin{aligned}\mathbf{J}_{\mathrm{Zr}} = &- w\, c_0 D_\beta \left(\frac{X_\beta(T)(1-x_{\mathrm{Pu}}-X_\beta(T))}{1-x_{\mathrm{Pu}}}\right)\left(\frac{\Delta H_\beta + Q^*_\beta}{RT^2}\right)\nabla T \\ &- (1-w)\, c_0 D_\gamma \left(\frac{X_\gamma(T)(1-x_{\mathrm{Pu}}-X_\gamma(T))}{1-x_{\mathrm{Pu}}}\right)\left(\frac{\Delta H_\gamma + Q^*_\gamma}{RT^2}\right)\nabla T. \end{aligned} \tag{16.13}$$

The weight factor w is set equal to the β phase fraction $f = (X_\gamma(T) - x_{\mathrm{Zr}})/(X_\gamma(T) - X_\beta(T))$. The flux in the $\alpha+\beta$ region is defined analogously. Some computational experiments were done using the more sophisticated weighting $w = \exp(a) f^b/[\exp(a) f^b + (1-f)^b]$ for parameters a and $b > 0$, however in the end we opted for the simple linear weighting ($a = 0$, $b = 1$).

16.2.3 Numerical Implementation

The preceding pseudo-binary model for U-19Pu-10Zr fuel was implemented into BISON with two essential numerical modifications: addition of an artificial diffusion term in the 2-phase region to stabilize the algorithm, and smoothing of the model coefficients near phase diagram curves. The full model with these modifications is described in this section. We solve the coupled system of equations,

$$\rho c_p \frac{\partial T}{\partial t} = \nabla \cdot k(x,T)\nabla T + q(\mathbf{r},x), \tag{16.14}$$

$$\frac{\partial x}{\partial t} = \nabla \cdot D(x,T)\nabla x + \nabla \cdot S(x,T)\nabla T, \tag{16.15}$$

for an evolving temperature distribution $T(\mathbf{r},t)$ and Zr atom fraction distribution $x_{\mathrm{Zr}} = x(\mathbf{r},t)$. This is a departure from the model considered in [177, 178] which used a fixed temperature profile. We use a variable heat source q that will depend on the axial position in the fuel rod and the local Zr fraction (actually the local fraction of actinides, which is the complement of the Zr fraction). Additionally a thermal conductivity model that accounts for constituent migration as well as porosity effects was used (Galloway model described in Section 8.10.1).

In a single-phase region of the phase diagram (here π denotes the arbitrary phase) we have,

$$D(x,T) = D_\pi(x,T), \tag{16.16}$$

$$S(x,T) = D_\pi(x,T)\left(\frac{x(1-x_{\mathrm{Pu}}-x)}{1-x_{\mathrm{Pu}}}\right)\frac{Q^\star_\pi}{RT^2}, \tag{16.17}$$

where D_π is the diffusivity and $Q^\star_\pi$ the heat of transport of Zr in the phase π. In the 2-phase $\beta+\gamma$ region bounded by the solubility limit curves X_β and X_γ, the Soret term coefficient is,

$$S(x,T) = f_\beta D_\beta(X_\beta(T),T)\left(\frac{X_\beta(T)(1-x_{\mathrm{Pu}}-X_\beta(T))}{1-x_{\mathrm{Pu}}}\right)\left(\frac{\Delta H_\beta + Q^*_\beta}{RT^2}\right), \tag{16.18}$$

$$+ (1-f_\beta) D_\gamma(X_\gamma(T),T)\left(\frac{X_\gamma(T)(1-x_{\mathrm{Pu}}-X_\gamma(T))}{1-x_{\mathrm{Pu}}}\right)\left(\frac{\Delta H_\gamma + Q^*_\gamma}{RT^2}\right), \tag{16.19}$$

where $f_\beta = (X_\gamma(T) - x)/(X_\gamma(T) - X_\beta(T))$ is the phase fraction of β according to the lever rule. In a 2-phase region one ought to take $D = 0$, however this would result in Equation 16.15 being purely advective with a transport velocity proportional to the temperature gradient. Mathematically this leads to jump discontinuities in the Zr atom fraction profile at domain boundaries and boundaries between single and 2-phase regions. Moreover, it is well-known that standard centered finite difference or Galerkin finite element schemes are unstable for pure advection, leading to spurious oscillations. Thus to stabilize our Galerkin finite element implementation we add some artificial diffusion and take,

$$D(x,T) = f_\beta D_\beta(X_\beta(T),T)p_\beta + (1 - f_\beta)D_\gamma(X_\gamma(T),T)p_\gamma, \tag{16.20}$$

where p_β and p_γ are dimensionless numerical parameters taken as small as possible while maintaining stability. In future work we plan to replace this simple stabilization approach with the SUPG (streamline upwind Petrov-Galerkin) finite element method, which can be also implemented within BISON.

The D and S coefficients in the 2-phase $\alpha + \delta$ region are defined in the analogous way.

16.2.4 Smoothing D and S

As defined above, D and S do not vary smoothly (or even continuously) with x and T when crossing phase diagram boundaries, and consequently the discretized system will be much more difficult to solve than it would otherwise be. We have ameliorated this effect by smoothing the relative phase contributions at each location in the phase diagram, discussed in detail in Section 16.4.1.

16.3 Modeling Parameters

There are many inputs needed for the fuel performance code BISON and all are not listed here. However a subset of inputs was determined to be either important for the simulations and worth mentioning, or newly added inputs for the constituent redistribution kernel and are given here.

- System power,
- Linear power for a specific height for single level 2-D simulations,
- Rod average linear power scaled with axial power profile for full length 2D-RZ simulations,
- Phase transition temperatures,
- Alpha-delta to beta-gamma transition temperature quoted to be 595 °C,
- Beta-gamma to gamma transition temperature 650 °C,
- Rod edge convective and axial t-infinity boundary condition for full length 2D-RZ simulations,

Table 16.2: Diffusion coefficients, $D = D_0 \exp(-Q/RT)$, and heats of transport for U-Pu-Zr where c is the zirconium atom fraction.

Phase	α	δ	β	γ
D_0 (m^2/s)	3.0×10^{-6}	3.0×10^{-6}	1.14×10^{-5}	$10^{-5.1-8.05c+0.13c^2}$
Q (kJ/mol)	170	150	180	$128 - 107c + 174c^2$
$Q^\star$	200	160	450	-200

- Fuel surface temperature boundary condition for 2-D simulations,
- Thermal conductivity and associated porosity modifiers,
- Phase-dependent (alpha, delta, beta and gamma) diffusion coefficients and heats of transport, with values and units given in Table 16.2, based on values from [179, 177, 178].

A sensitivity study was performed on these modeling parameters, with the exception of thermal conductivity and heats of transport, to assess the importance of each parameter. It was found that the parameters that control the radial location of phase transformation, those that directly affect temperature (system power, phase transition temperatures and the temperature boundary conditions) have the most significant effect, whereas parameters that deal with the rate of migration (diffusion coefficients) have a much less significant impact on the location of phase transitions. Not all cases are shown here, however two representative cases are shown that illustrate this impact. In the two cases shown, Figure 16.3 and 16.4, the alpha phase diffusion coefficient and power, respectively, both were adjusted by +/-20% in order to see the impact on the simulation. Clearly observed is a minimal impact by the diffusion coefficient adjustment but a significant impact in the power adjustment, greatly adjusting the Zirconium profile shape depending on higher or lower powers. The same trends as Figure 16.3 were observed for all phase diffusion coefficients, while the same trends as Figure 16.4 were observed for transition temperatures adjustments and boundary condition adjustments.

16.4 BISON implementation

While the previous sections described the theory behind the zirconium redistribution model, the following sections describe the implementation of the model into BISON. The redistribution relies on two material models, `PhaseUPuZr` and `ZrDiffusivityUPuZr`, to calculate the necessary parameters for diffusion, and a single kernel, `ZirconiumDiffusion`, to actually redistribute the zirconium within the mesh.

16.4.1 Phase Determination `[PhaseUPuZr]`

The diffusivity of zirconium in U-Pu-Zr fuel is heavily dependent on the current phase. This is true for both Fickian and Soret type diffusion. As such, it is essential to know where the current mesh point lies within the pseudo two-phase diagram (Figure 16.2) as a function of temperature

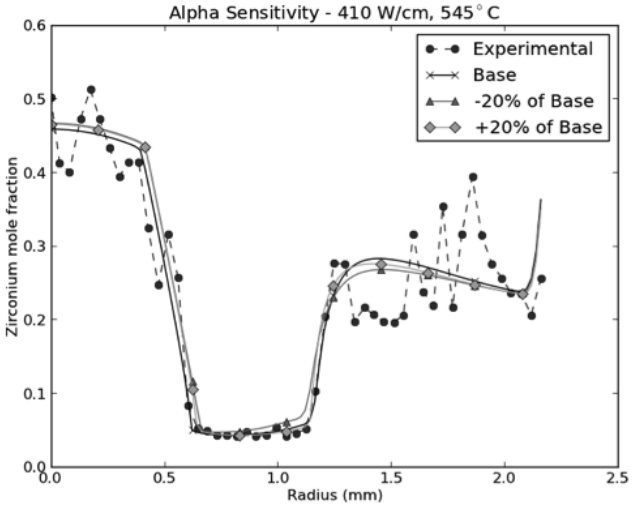

Figure 16.3: Zirconium distribution alpha phase diffusion coefficient sensitivity.

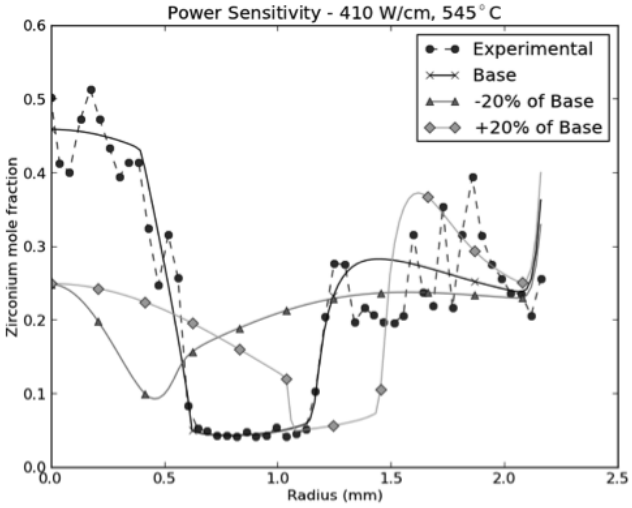

Figure 16.4: Zirconium distribution power sensitivity.

T and zirconium concentration x_{Zr}. This is achieved using Equation 16.12 to calculate the solvus lines, typically with the parameters in Table 16.1, however each parameter can be set at run-time. Once each solvus line is calculated, the point described by (T, x_{Zr}) will explicitly give the phase diagram region, either in the single phase regions [α, δ, β, γ] or the two-phase regions [$\alpha+\delta$, $\beta+\gamma$].

While determination of the phase region is important, it does not provide the necessary composition fractions of each single phase in the two-phase region. In addition, the smoothing of the diffusion coefficients D and S is necessary to ensure adequate convergence. As such, `PhaseUPuZr` explicitly tracks the fraction of each single phase type for any combination of (T, x_{Zr}), determining each phase's contribution in the 2-phase region using the lever-rule, and artificially smoothing the transitions between phases by using an artificial smoothing width.

Two types of smoothing are required. The first occurs when the zirconium concentration is held constant, and temperature increases (or decreases) across a phase-transition line described by the transition temperatures between points A and B (T_{AB}) and points C and D (T_{CD}) in the simplified phase diagram (Figure 16.2). A mixing width ε_T (typically 2 K) is utilized such that if the temperature falls within $\pm\varepsilon_T$ of a temperature transition $T_{AB,CD}$, the relative fraction of the upper and lower phases are smoothed across the transition region so that abrupt changes are avoided. Similar smoothing is required as temperature is held constant and x_{Zr} moves across solvus lines. Smoothing occurs across the region $\pm\varepsilon_x$ of the solvus line, with ε_x typically 0.02.

After the lever rule is applied to the two-phase region and all smoothing is calculated, `PhaseUPuZr` results in the fraction of each single phase region at any given point. This information can then be used to calculate any phase dependent properties.

16.4.2 Zirconium Diffusivities `[ZrDiffusivityUPuZr]`

Using the phase fractions calculated in `PhaseUPuZr`, `ZrDiffusivityUPuZr` calculates the Fickian and Soret diffusion coefficients using Equation 16.17 and 16.19. The artificial two-phase diffusivity parameter p is used to set the diffusivity in the two-phase regions, and is typically set to $p = 0.2$. A scalar factor $D_{0,scalar}$ is also included to tune the diffusivities within each phase. It should be noted that $D_{0,scalar}$ is multiplied against all diffusivity values, including the Soret calculation, except for the artificial two-phase regions. In these regions, the only scalar utilized is the p values.

16.4.3 Zirconium Diffusion `[ZirconiumDiffusion]`

After all the diffusivities are set, `ZirocniumDiffusion` is used to transport the zirconium across the mesh using Equation 16.15.

Bibliography

[1] R. L. Williamson, J. D. Hales, S. R. Novascone, M. R. Tonks, D. R. Gaston, C. J. Permann, D. Andrs, and R. C. Martineau. Multidimensional multiphysics simulation of nuclear fuel behavior. *J. Nucl. Mater.*, 423:149–163, 2012.

[2] J. D. Hales, R. L. Williamson, S. R. Novascone, D. M. Perez, B. W. Spencer, and G. Pastore. Multidimensional multiphysics simulation of TRISO particle fuel. *J. Nucl. Mater.*, 443:531–543, November 2013.

[3] Pavel Medvedev. Fuel performance modeling results for representative FCRD irradiation experiments: Projected deformation in the annular AFC-3A U-10Zr fuel pins and comparison to alternative designs. Technical Report INL/EXT-12-27183 Revision 1, Idaho National Laboratory, 2012.

[4] D. Gaston, C. Newman, G. Hansen, and D. Lebrun-Grandié. MOOSE: A parallel computational framework for coupled systems of nonlinear equations. *Nucl. Eng. Design*, 239:1768–1778, 2009.

[5] C. Newman, G. Hansen, and D. Gaston. Three dimensional coupled simulation of thermomechanics, heat, and oxygen diffusion in UO_2 nuclear fuel rods. *J. Nucl. Mater.*, 392:6–15, 2009.

[6] M. M. Rashid. Incremental kinematics for finite element applications. *Internat. J. Numer. Methods Engrg.*, 36:3937–3956, 1993.

[7] Sam Key. Fma-3d theoretical manual. Technical Report Ver 32, FMA Development, LLC, Great Falls, Montanta, 2011.

[8] Fionn Dunne and Nik Petrinic. *Introduction to Computational Plasticity*. Oxford University Press, Oxford, 2005.

[9] Special Metals Incoloy alloy MA956. www.specialmetals.com/documents/Incoloy

[10] Schwarzkopf Plansee PM 2000. http://www.matweb.com/search/datasheet.aspx?matguid=21e9ec9a0de24b47l

[11] Kanthal APMT Material Database. http://kanthal.com/en/products/material-datasheets/tube/kanthal-apmt/.

[12] Resistalloy International Fecralloy Electrical Resistance Steel. http://www.matweb.com/search/datasheet.aspx?MatGUID=c2427c6297594858bedac2a4e5981d2f.

[13] Z. T. Thompson, K. A. Terrani, and Y. Yamamoto. Elastic Modulus Measurement of ORNL ATF FeCrAl Alloys. Technical Report ORNL/TM-2015/632, Oak Ridge National Laboratory, October 2015.

[14] P. Seiler, M. Bäker, and J. Rösler. Variation of creep properties and interfacial roughness in thermal barrier coating systems. *Advanced Ceramic Coatings and Materials for Extreme Environments*, 32:129–136, 2011.

[15] S. R. J. Saunders, H. E. Evans, M. Li, D. D. Gohil, and S. Osgerby. Oxidation growth stresses in an alumina-forming ferritic steel measured by creep deflection. *Oxidation of Metals*, 48:189–200, 1997.

[16] K. A. Terrani, T. M. Karlsen, and Y. Yamamoto. Input correlations for irradiation creep of FeCrAl and SiC based on in–pile Halden test results. Technical Report ORNL/TM-2016/191, ORNL, May 2016.

[17] B.A. Pint, K.A. Terrani, Y. Yamamoto, and L.L. Snead. Material Selection for Accident Tolerant Fuel Cladding. *Metallurgical and Materials Transactions E*, 2E:190–196, 2015.

[18] Bo Jönsson, Qin Lu, and Dilip Chandrasekaran. Oxidation and Creep Limited Lifetime of Kanthal APMT, a Dispersion Strengthened FeCrAlMo Alloy Designed for Strength and Oxidation Resistance at High Temperatures. *Oxidation of Metals*, 79:29–39, 2013.

[19] Y. Yamamoto, B.A. Pint, K.A. Terrani, K.G. Field, Y. Yang, and L.L. Snead. Development and property evaluation of nuclear grade wrought FeCrAl fuel cladding for light water reactors. *Journal of Nuclear Materials*, 467:703–716, 2015.

[20] L. Leibowitz and R.A. Blomquist. Thermal conductivity and thermal expansion of stainless steels D9 and HT9. *International Journal of Thermophysics*, 9(5):873–883, 1988.

[21] N. Yamanouchi, M. Tamura, H. Hayakawa, and T. Kondo. Accumulation of engineering data for practical use of reduced activation ferritic steel: 8%Cr-2%W-0.2%V-0.04%Ta-Fe. *J. Nucl. Mater.*, 191–194:822–826, 1992.

[22] S. Sharafat, R. Amodeo, and N.M. Ghoniem. Materials data base and design equations for the ucla solid breeder blanket. Technical Report UCLA-ENG-8611, PPG-937, UCLA, 1986.

[23] Compiled by: IFR Property Evaluation Working Group. Metallic fuels handbook. Argonne National Laboratory, June 1988.

[24] A. Karahan and J. Buongiorno. A new code for predicting the thermo-mechanical and irradiation behavior of metallic fuels in sodium fast reactors. *J. Nucl. Mater.*, 396:283–293, 2010.

[25] C. Nam, W. Hwang, and D. Sohn. Statistical failure analysis of metallic U-10Zr/HT9 fast reactor fuel pin by considering the Weibull distribution and cumulative damage fraction. *Ann. Nucl. Energy*, 25(17):1441–1453, 1998.

[26] V. Tvergaard. Effect of grain boundary sliding on creep constrained diffusive cavitation. *J. Mech. Phys. Solids*, 33(5):447–469, 1985.

[27] CINDA Recommended Data Based on CINDAS Evaluation from Available Information. https://cindasdata.com/Applications/TPMD/, June 2014.

[28] G. W. Lehmang. Thermal Properties of Refractory Materials. Technical report, Wright Air Development Division, 1960.

[29] Nicrofer 3033 - alloy 33, Material Data Sheet No. 4041. ThyssenKrupp VDM, 2000.

[30] D. Petti, P. Martin, M. Phelip, and R. Ballinger. Development of improved models and designs for coated-particle gas reactor fuels. Technical Report INL/EXT-05-02615, December 2004.

[31] J. J. Powers and B. D. Wirth. A review of TRISO fuel performance models. *J. Nucl. Mater.*, 405:74–82, 2010.

[32] C. A. Lewinsohn, M. L. Hamilton, G. E. Youngblood, R. H. Jones, F. A. Garner, S. L. Hecht, and A. Kohyama. Irradiation-enhanced creep in SiC: data summary and planned experiments. *J. Nucl. Mater.*, 253:36–46, 1998.

[33] Kenneth C. Mills. *Recommended Values of Thermophysical Properties for Selected Commercial Alloys*. Woodhead Publishing, 2002.

[34] J. K. Fink. Thermophysical properties of uranium dioxide. *J. Nucl Materials*, 279(1):1–18, 2000.

[35] P. G. Lucuta, H. J. Matzke, and I. J. Hastings. A pragmatic approach to modelling thermal conductivity of irradiated UO_2 fuel: review and recommendations. *J. Nucl. Mater.*, 232:166–180, 1996.

[36] D. D. Lanning, C. E. Beyer, and K. J. Geelhood. Frapcon-3 updates, including mixed-oxide fuel properties. Technical Report NUREG/CR-6534, Vol. 4 PNNL-11513, 2005.

[37] A. Marion (NEI) letter dated June 13, 2006 to H. N. Berkow (USNRC/NRR). Safety Evaluation by the Office of Nuclear Reactor Regulation of Electric Power Research Institute (EPRI) Topical Report TR-1002865, Topical Report on Reactivity Initiated Accidents: Bases for RIA Fuel rod Failures and Core Coolability Criteria. http://pbadupws.nrc.gov/docs/ML0616/ML061650107.pdf, 2006.

[38] W. F. Lyon. Summary report: Gd thermal conductivity model updates. Technical Report ANA-P1400138-TN03 Rev. 2, Anatech Corp., 2015.

[39] C. M. Allison, G. A. Berna, R. Chambers, E. W. Coryell, K. L. Davis, D. L. Hagrman, D. T. Hagrman, N. L. Hampton, J. K. Hohorst, R. E. Mason, M. L. McComas, K. A. McNeil, R. L. Miller, C. S. Olsen, G. A. Reymann, and L. J. Siefken. SCDAP/RELAP5/MOD3.1 code manual, volume IV: MATPRO–A library of materials

properties for light-water-reactor accident analysis. Technical Report NUREG/CR-6150, EGG-2720, Idaho National Engineering Laboratory, 1993.

[40] K. Ohira and N. Itagaki. Thermal conductivity measurements of high burnup UO_2 pellet and a benchmark calculation of fuel center temperature. In *Proceedings of the American Nuclear Society Meeting on Light Water Reactor Fuel Performance*, page 541, Portland, Oregon, Mar 2 to Mar 6, 1997.

[41] J. Carbajo, L. Gradyon, S. Popov, and V. Ivanov. A review of the thermophysical properties of mox and uo2 fuels. *J. Nucl. Mater.*, 299:181–198, 2001.

[42] C. Duriez, J.-P. Alessandri, T. Gervais, and Y. Philipponneau. Thermal conductivity of hypostoichiometriclow pu content mixed oxide. *J. Nucl. Mater.*, 277:143–158, 2000.

[43] C. Ronchi, M. Sheindlin, M. Musella, and G.J. Hyland. Thermal conductivity of uranium dioxide up to 2900 k from simultaneous measurement of the heat capacity and thermal diffusivity. *Journal of Applied Physics*, 85:776–789, 1999.

[44] M. Amaya, J. Nakamura, F. Nagase, and T. Fuketa. Thermal conductivity evaluation of high burnup mixed-oxide (mox) fuel pellet. *J. Nucl. Mater.*, 414:303–308, 2011.

[45] M. Inoue, K. Maeda, K. Katsuyama, K. Tanaka, K. Mondo, and M. Hisada. Fuel-to-cladding gap evolution and its impact on thermal performance of high burnup fast reactor type uranium-plutonium oxide fuel pins. *J. Nucl. Mater.*, 326(1):59–73, 2004.

[46] Aydin Karahan. *Modeling of thermo-mechanical and irradiation behavior of metallic and oxide fuels for sodium fast reactors*. PhD thesis, Massachusetts Institute of Technology, June 2009.

[47] M. Kato, K. Maeda, T. Ozawa, M. Kashimura, and Y. Kihara. Physical properties and irradiation behavior analysis of Np- and Am-bearing MOX fuels. *Journal of Nuclear Science and Technology*, 48:646–653, 2011.

[48] Y. Rashid, R. Dunham, and R. Montgomery. Fuel analysis and licensing code: FALCON MOD01. Technical Report EPRI 1011308, Electric Power Research Institute, December 2004.

[49] Eds. M. A. Kramman, H. R. Freeburn. Escore–the epri steady-state core reload evaluator code: General description. Technical Report EPRI NP-5100, Electric Power Research Institute, February 1987.

[50] K. Lassmann and H. Blank. Modelling of fuel rod behavior and recent advances of the TRANSURANUS code. *Nucl. Engrg. Design*, 106:291–313, 1988.

[51] A. T. Mai, W. F. Lyon, R. O. Montgomery, and R. S. Dunham. An evaluation of the MATPRO fuel creep model using the FALCON fuel analysis code. *Trans. Am. Nucl. Soc.*, 102:888–889, 2010.

[52] Y. R. Rashid, H. T. Tang, and E. B. Johansson. Mathematical treatment of hot pressing of reactor fuel. *Nucl. Engrg. Design*, 29:1–6, 1974.

[53] Y. Guerin. Mechanical-behaviour of nuclear fuel under irradiation. *Annales de chimie - science des materiaux*, 10:405–414, 1985.

[54] C. Milet and C. Piconi. Fluage en pile de l'oxyde mixte uo2-puo2. *J. Nucl. Mater.*, 116:196–199, 1983.

[55] J. L. Routbort. Compressive creep of mixed oxide fuel pellets. *J. Nucl. Mater.*, 44:247–259, 1972.

[56] M. Kato, Y. Ikusawa, T. Sunaoshi, A. Nelson, and K. McClellan. Thermal expansion measurement of $(U,Pu)O_{2-x}$ in oxygen partial pressure-controlled atmosphere. *Journal of Nuclear Materials*, 469:223–227, 2016.

[57] V. Z. Jankus and R. W. Weeks. LIFE-II – A computer analysis of fast-reactor fuel-element behaviour as a function of reactor operating history. *Nuclear Engineering and Design*, 18:41–49, 1972.

[58] M. Oguma. Cracking and relocation behavior of nuclear-fuel pellets during rise to power. *Nuclear Engineering and Design*, 76(1):35–45, 1983.

[59] L.A. Walton and D.L. Husser. Fuel pellet fracture and relocation, 1983. IAEA Specialists Meeting on Water Reactor Fuel Element Performance Computer Modelling, Preston, UK.

[60] J.B. Ainscough, B.W. Oldfield, and J.O. Ware. Isothermal grain growth kinetics in sintered UO_2 pellets. *J. Nucl. Mater.*, 49:117–128, 1973.

[61] M.I. Mendelson. Average grain size in polycrystalline ceramics. *Journal of the American Ceramic Society*, 52:443–446, 1969.

[62] Yeon Soo Kim and G. L. Hofman. AAA Fuels Handbook. Technical report.

[63] M. C. Billone, Y. Y. Liu, E. E. Gruber, T. H. Hughes, and J. M. Kramer. Status of Fuel Element Modeling Codes for Metallic Fuels. In *Proceedings American Nuclear Society Internaionl Conference on Reliable Fuels for Liquid Metal Reactors*, Tucson, Arizona, September 7–11 1968.

[64] J Galloway, C Unal, N Carlson, D Porter, and S Hayes. Modeling constituent redistribution in U–Pu–Zr metallic fuel using the advanced fuel performance code BISON. *Nuclear Engineering and Design*, 286:1–17, May 2015.

[65] Dawn E Janney and Cynthia A Papesch. FCRD Transmutation Fuels Handbook 2015. Technical Report INL/EXT-15-36520, Idaho National Laboratory, September 2015.

[66] Y S Touloukian, R W Powell, C Y Ho, and P G Klemens. *Thermophysical Properties of Matter - The TPRC Data Series. Volume 2. Thermal Conductivity - Nonmetallic Solids*. New York, NY, January 1971.

[67] Yoichi Takahashi, Michio Yamawaki, and Kazutaka Yamamoto. Thermophysical properties of uranium-zirconium alloys. *Journal of Nuclear Materials*, 154(1):141–144, June 1988.

[68] T H Bauer. In-Pile Measurement of the Thermal Conductivity of Irradiated Metallic Fuel. *Nuclear Technology*, 110(3):1–15, 1995.

[69] Yeon Soo Kim, Tae Won Cho, and Dong-Seong Sohn. Thermal conductivities of actinides (U, Pu, Np, Cm, Am) and uranium-alloys (U-Zr, U-Pu-Zr and U-Pu-TRU-Zr). *Journal of Nuclear Materials*, 445(1-3):272–280, February 2014.

[70] C Matthews and C Unal. Unpublished work. 2015.

[71] H. Savage. The heat content and specific heat of some metallic fast-reacdtor fuels containing plutonium. *Journal of Nuclear Materials*, 25:583–594, 2006.

[72] T. R. G. Kutty, C. B. Basak, A. Kumar, and H. S. Kamath. Creep beahviour of δ-phase of U-Zr system by impression creep technique. *Journal of Nuclear Materials*, 408:90–95, 2010.

[73] T. Ogata and T. Yokoo. Devlopment and Validation of ALFUS: An Irradiation Behavior Analysis Code for Metallic Fast Reactor Fuels. *Journal of Nuclear Technology*, 128(1):113–123, 1999.

[74] Takanari Ogata, Motoyasu Kinoshita, Hiroaki Saito, and Takeshi Yokoo. Analytical study on deformation and fission gas behavior of metallic fast reactor fuel. *Journal of nuclear materials*, 230(2):129–139, 1996.

[75] R. S. Barnes. A Theory of Swelling and Gas Release for Reactor Materials. *Journal of Nuclear Materials*, 11:135–148, 1964.

[76] A. T. Churchman, R. S. Barnes, and A. H. Cottrell. Effects of Heat and Pressure on the Swelling of Irradiated Uranium. *Nuclear Energy*, 7:88–96, 1958.

[77] H A Saller, R F Dickerson, and W E Murr. Uranium Alloys for High-Temperature Application. Technical Report BMI-1098, Divison of Technical Information Extension, U.S. Atomic Energy Commission, June 1956.

[78] D. E. Burkes, C. A. Papesch, A. P. Maddison, T. Hartmann, and F. J. Rice. Thermophysical properties of DU-10 wt.*Journal of Nuclear Materials*, 403:160 – 166, 2010.

[79] Y. S. Kim, G. L. Hofman, J. S. Cheon, A. B. Robinson, and D. M. Wachs. Fission induced swelling and creep of U-Mo alloy fuel. *Journal of Nuclear Materials*, 437:37–46, 2013.

[80] J. T. White, A. T. Nelson, J. T. Dunwoody, D. D. Byler, D. J. Safarik, and K. J. McClellan. Thermophysical properties of U_3Si_2 to 1773K. *J. Nucl. Mater.*, 464:275–280, 2015.

[81] H. Shimizu. The properties and irradiation behavior of U_3Si_2. Technical Report NAA-SR-10621, Atomics International, 1965.

[82] J. E. Matos and J. L. Snelgrove. Research reactor core conversion guidebook-Vol 4: Fuels (Appendices I-K). Technical Report IAEA-TECDOC-643, 1992.

[83] C.Y. Ho, M.W. Ackerman, K.Y. Wu, S.G. Oh, and T.N. Havill. Thermal conductivity of ten selected binary alloy systems. *Journal of Physical and Chemical Reference Data*, 7:959, 1978.

[84] Yu. Yu. Tsiovkin, V.V. Dremov, E.S. Koneva, A.A. Povzner, A.N. Filanovich, and A.N. Petrova. Theory of the residual electrical resistivity of binary actinide alloys. *Journal of Physics of the Solid State*, 52:1–5, 2010.

[85] C.J. Glassbrenner and G.A. Slack. Thermal conductivity of silicon and germanium from 3k to the melting point. *Journal of Physical Review*, 134:A1059, 1964.

[86] J. T. White, A. T. Nelson, D. D. Byler, D. J. Safarik, J.T. Dunwoody, and K. J. McClellan. Thermophysical properties of U_3Si_5 to 1773K. *J. Nucl. Mater.*, 456:442–448, 2015.

[87] J.L Snelgrove M. R. Finlay, G. L. Hofman. Irradiation behaviour of uranium silicide compounds. *Journal of Nuclear Materials*, 325:118–128, 2004.

[88] G. L. Hofman and W. S. Ryu. Detailed Analysis of Uranium Silicide Dispersion Fuel Swelling. Technical Report CONF-8909141–10, Argonne National Laboratory, 1989.

[89] R. Matthews S. Ross, M.El Genk. Uranium Nitride Fuel Swelling Correlation). Technical Report UraniumNitrideSwelingCorrelation, 1989.

[90] N. E. Hoppe. Engineering model for zircaloy creep and growth. In *Proceedings of the ANS-ENS International Topical Meeting on LWR Fuel Performance*, pages 157–172, Avignon, France, April 21-24, 1991.

[91] T. A. Hayes and M. Kassner. Creep of zirconium and zirconium alloys. *Metallurgical and Materials Transactions A*, 37A:2389–2396, 2006.

[92] J.H. Moon, P.E. Cantonwine, K.R. Anderson, S. Karthikeyan, and M.J. Mills. Characterization and modeling of creep mechanisms in zircaloy-4. *J. Nucl. Mater.*, 353(3):177 – 189, 2006.

[93] M. Limbäck and T. Andersson. A model for analysis of the effect of final annealing on the in- and out-of-reactor creep behavior of zircaloy cladding. In *Zirconium in the Nuclear Industry: Eleventh International Symposium*, ASTM STP 1295, pages 448–468, 1996.

[94] Y. Matsuo. Thermal creep of zircaloy-4 cladding under internal pressure. *Journal of Nuclear Science and Technology*, 24(2):111–119, February 1987.

[95] J.P. Foster, H.K. Yueh, and R.J. Comstock. Zirlo^{TM} cladding improvement. *Journal of ASTM International*, 5(7), 2008.

[96] M. Quecedo, M. Lloret, J.M. Conde, C. Alejano, J.A. Gago, and F.J. Fernandez. Results of thermal creep test on highly irradiated zirlo^{TM}. *Nuclear Engineering and Technology*, 41(2):179–186, 2009.

[97] C.S. Seok, B. Marple, Y.J. Song, S. Gollapudi, I. Charit, and K.L. Murty. High temperature deformation characteristics of zirlo^{TM} tubing via ring-creep and burst tests. *Nuclear Engineering and Design*, 241:599–602, 2011.

[98] P. Van Uffelen, C. Győri, A. Schubert, J. van de Laar, Z. Hózer, and G. Spykman. Extending the application range of a fuel performance code from normal operating to design basis accident conditions. *J. Nucl. Mater.*, 383:137–143, 2008.

[99] H. J. Neitzel and H. Rosinger. The development of a burst criterion for zircaloy fuel cladding under loca conditions. Technical Report KfK 4343, Kernforschungszentrum Karlsruhe, Germany, 1980.

[100] F. J. Erbacher, H. J. Neitzel, H. Rosinger, H. Schmidt, and K. Wiehr. Burst criterion of Zircaloy fuel claddings in a loss-of-coolant accident. In *Zirconium in the Nuclear Industry, Fifth Conference, ASTM STP 754, D.G. Franklin Ed.*, pages 271–283. American Society for Testing and Materials, 1982.

[101] M. E. Markiewicz and F.J. Erbacher. Experiments on ballooning in pressurized and transiently heated Zircaloy-4 tubes. Technical Report KfK 4343, Kernforschungszentrum Karlsruhe, Germany, 1988.

[102] K.J. Geelhood et al. PNNL stess/strain correlation for Zircaloy. Technical Report PNNL-17700, Pacific Northwest National Laboratory.

[103] Y. R. Rashid, A. J. Zangari, and C. L. Lin. Modeling of PCI Under Steady State and Transient Operating Conditions. In *Proceedings of a technical committee meeting organized by the IAEA: Water Reactor Fuel Element Computer Modelling in Steady State, Transient, and Accident Conditions*, Preston, United Kingdom, September 18-22, 1988.

[104] A.R. Massih. Transformation kinetics of zirconium alloys under non-isothermal conditions. *J. Nucl. Mater.*, 384:330–335, 2009.

[105] A.R. Massih and L.O. Jernkvist. Transformation kinetics of alloys under non-isothermal conditions. *Modelling Simul. Mater. Sci. Eng.*, 17:055002 (15pp), 2009.

[106] A.R. Massih. Evaluation of loss-of-coolant accident simulation tests with the fuel rod analysis code FRAPTRAN-1.4. Technical Report TR11-008V1, Quantum Technologies AB, 2011.

[107] Adrien Couet, Arthur T. Motta, and Robert J. Comstock. Hydrogen pickup measurements in zirconium alloys: Relation to oxidation kinetics. *Journal of Nuclear Materials*, 451(13):1 – 13, 2014.

[108] Olivier Courty, Arthur T. Motta, and Jason D. Hales. Modeling and simulation of hydrogen behavior in Zircaloy-4 fuel cladding. *J. Nucl. Mater.*, 452:311–320, 2014.

[109] Andrew McMinn, Edward C Darby, and John S Schofield. The terminal solid solubility of hydrogen in zirconium alloys. *ASTM special technical publication*, 1354:173–195, 2000.

[110] BG Kammenzind, David G Franklin, H Richard Peters, and Walter J Duffin. Hydrogen pickup and redistribution in alpha-annealed Zircaloy-4. *ASTM Special Technical Publication*, 1295:338–369, 1996.

[111] G.P. Marino. Hydrogen supercharging in zircaloy. *Materials Science and Engineering*, 7(6):335 – 341, 1971.

[112] K Une and S Ishimoto. Dissolution and precipitation behavior of hydrides in Zircaloy-2 and high Fe Zircaloy. *Journal of Nuclear Materials*, 322(1):66–72, 2003.

[113] Olivier F. Courty, Arthur T. Motta, Christopher J. Piotrowski, and Jonathan D. Almer. Hydride precipitation kinetics in zircaloy-4 studied using synchrotron x-ray diffraction. *Journal of Nuclear Materials*, 461(0):180 – 185, 2015.

[114] Randall D Manteufel and Neil E Todreas. Effective thermal conductivity and edge conductance model for a spent-fuel assembly. *Nuclear technology*, 105(3):421–440, 1994.

[115] V. Di Marcello, A. Schubert, J. van de Laar, and P. Van Uffelen. The TRANSURANUS mechanical model for large strain analysis. *Nuclear Engineering and Design*, 276:19–29, 2014.

[116] G. K. Miller, D. A. Petti, J. T. Maki, and D. L. Knudsen. PARFUME theory and model basis report. Technical Report INL/EXT-08-14497, Idaho National Laboratory, 2009.

[117] G. Pastore, L. Luzzi, V. Di Marcello, and P. Van Uffelen. Physics-based modelling of fission gas swelling and release in UO_2 applied to integral fuel rod analysis. *Nuclear Engineering and Design*, 256:75–86, 2013.

[118] R.J. White and M.O. Tucker. A new fission-gas release model. *J. Nucl. Mater.*, 118:1–38, 1983.

[119] M.V. Speight. A calculation on the migration of fission gas in material exhibiting precipitation and re-solution of gas atoms under irradiation. *Nuclear Science and Engineering*, 37:180–185, 1969.

[120] P. Hermansonn and A.R. Massih. An effective method for calculation of diffusive flow in spherical grains. *Journal of Nuclear Materials*, 304:204–211, 2002.

[121] D. Pizzocri, C. Rabiti, L. Luzzi, T. Barani, P. Van Uffelen, and G. Pastore. PolyPole-1: An accurate numeical algorithm for intra-granular fission gas release. *Journal of Nuclear Materials*, 478:333–342, 2016.

[122] K. Lassmann, C.T. Walker, J. van de Laar, and F. Lindström. Modelling the high burnup UO_2 structure in LWR fuel. *J. Nucl. Mater.*, 226:1–8, 1995.

[123] S. Kashibe, K. Une, and K. Nogita. Formation and growth of intragranular fission gas bubbles in UO_2 fuels with burnup of 6-83 GWd/t. *J. Nucl. Mater.*, 206:22–34, 1969.

[124] T. Kogai. Modelling of fission gas release and gaseous swelling of light water reactor fuels. *J. Nucl. Mater.*, 244:131–140, 1997.

[125] A.R. Massih and K. Forsberg. Calculation of grain boundary gaseous swelling in UO_2. *J. Nucl. Mater.*, 377:406–408, 2008.

[126] J. Rest. The effect of irradiation-induced gas-atom re-solution on grain-boundary bubble growth. *J. Nucl. Mater.*, 321:305–312, 2003.

[127] R.J. White. The development of grain-face porosity in irradiated oxide fuel. *J. Nucl. Mater.*, 325:61–77, 2004.

[128] D.R. Olander and P. Van Uffelen. On the role of grain boundary diffusion in fission gas release. *J. Nucl. Mater.*, 288:137–147, 2001.

[129] M.S. Veshchunov. Modelling of grain face bubbles coalescence in irradiated UO_2 fuel. *J. Nucl. Mater.*, 374:44–53, 2008.

[130] M.V. Speight and W. Beere. Vacancy potential and void growth on grain boundaries. *Metal Science*, 9:190–191, 1975.

[131] E. Rothwell. The release of Kr^{85} from irradiated uranium dioxide on post-irradiation annealing. *Journal of Nuclear Materials*, 5:241–249, 1962.

[132] K. Une and S. Kashibe. Fission gas release during post irradiation annealing of BWR fuels. *Journal of Nuclear Science and Technology*, 27:1002–1016, 1990.

[133] E. Sartori, J. Killeen, and J. A. Turnbull. International Fuel Performance Experiments (IFPE) Database. OECD-NEA, 2010, available at http://www.oecd-nea.org/science/fuel/ifpelst.html.

[134] G. Ducros, Y . Pontillon, and P.P. Malgouyres. Synthesis of the VERCORS experimental program: separate-effect experiments on fission product release, in support of the PHEBUS-FP programme. *Annals of Nuclear Energy*, 61:75–87, 2013.

[135] G. Pastore, D. Pizzocri, S. R. Novascone, D. M. Perez, B. W. Spencer, R.L. Williamson, P. Van Uffelen, and L. Luzzi. Modelling of transient fission gas behaviour in oxide fuel and application to the BISON code. In *Enlarged Halden Programme Group Meeting, Røros, Norway, September 7–12*, 2014.

[136] B.J. Lewis. Fission product release from nuclear fuel by recoil and knockout. *J. Nucl. Mater.*, 148:28–42, 1987.

[137] Y.-H. Koo, B.-H. Lee, and D.-S. Sohn. Analysis of fission gas release and gaseous swelling in UO_2 fuel under the effect of external restraint. *J. Nucl. Mater.*, 280:86–98, 2000.

[138] D. R. Olander. *Fundamental aspects of nuclear reactor fuel elements*. Technical Information Center, Energy Research and Development Administration, 1976.

[139] K. Forsberg and A. R. Massih. Diffusion theory of fission gas migration in irradiated nuclear fuel UO_2. *J. Nucl Materials*, 135(2-3):140–148, 1985.

[140] J. A. Turnbull, R. White, and C. Wise. The diffusion coefficient for fission gas atoms in UO_2. Technical Report IAEA-TC-659/3.5, 1987.

[141] Alicia Denis and Rosa Piotrkowski. Simulation of isothermal fission gas release. *J. Nucl. Mater.*, 229:149–154, 1996.

[142] H. Wallin. Forsberg-Massih fission gas model in BISON: Calibration using the Risø3 fuel test AN2. Technical Report Anatech, San Diego, CA, 2012.

[143] C. Vitanza, E. Kolstad, and U. Graziani. Fission gas release from UO_2 pellet fuel at high burnup. In *Proceedings of the American Nuclear Society Meeting on Light Water Reactor Fuel Performance*, page 361, Portland, Oregon, Apr 29 to May 3, 1979.

[144] Paul van Uffelen. Modelling isothermal fission gas release. In *Technical and economic limits to fuel burnup extension*, number IAEA-TECDOC-1299, pages 17–30. International Atomic Energy Agency, 2002.

[145] K. Lassmann, C. O'Carroll, J. van de Laar, and C. T. Walker. The radial distribution of plutonium in high burnup UO_2 fuels. *J. Nucl. Materials*, 208:223–231, 1994.

[146] American national standard for decay heat power in light water reactors. Technical Report ANSI/ANS-5.1-1979, American Nuclear Society, 1979.

[147] A. M. Ross and R. L. Stoute. Heat transfer coefficient between UO_2 and Zircaloy-2. Technical Report AECL-1552, Atomic Energy of Canada Limited, 1962.

[148] D. D. Lanning and C. R. Hann. Review of methods applicable to the calculation of gap conductance in zircaloy-clad uo2 fuel rods. Technical Report BWNL-1894, UC-78B, 1975.

[149] K.-T. Kim. UO_2/Zry-4 chemical interaction layers for intact and leak PWR fuel rods. *Journal of Nuclear Materials*, 404:128–137, 2010.

[150] M. Heinstein and T. Laursen. An algorithm for the matrix-free solution of quasistatic frictional contact problems. *Int. J. Numer. Meth. Engrg.*, 44:1205–1226, 1999.

[151] N. E. Todreas and M. S. Kazimi. *Nuclear systems I: thermal hyraulic fundamentals*. Hemisphere Publishing Corporation, New York, N.Y., USA, 1990.

[152] L. S. Tong and J. Weisman. *Thermal analysis of pressurized water reactors*. American Nuclear Society, La Grange Park, Illinois, USA, 1996.

[153] L. S. Tong and Y. S. Tang. *Boiling heat transfer and two-phase flow*. Taylor and Francis, Washington, DC, USA, 1997.

[154] R L Dougall and W M Rohsenow. Film-boiling heat transfer from a horizontal surface. *Journal of Heat Transfer*, 83:351–358, 1961.

[155] M E Cunningham, C E Beyer, P G Medvedev, and G A Berna. Fraptran: A computer code for the transient analysis of oxide fuel rods. Technical Report NUREG/CR-6739 Vol.1, Pacific Northwest National Laboratory, 2001.

[156] F. F. Cadek, D. P. Dominicis, H. C. Yeh, and R. H. Leyse. Pwr flecht final report supplement. Technical Report WCAP-7931, Westinghouse, October 1972.

[157] IAPWS. Revised release on the IAPWS industrial formulation 1997 for the thermodynamic properties of water and steam. 2007.

[158] IAPWS. Revised release on the IAPWS formulation 1985 for the thermal conductivity of ordinary water substance. 2008.

[159] IAPWS. Release on the IAPWS formulation 2008 for the viscosity of ordinary water substance. 2008.

[160] IAPWS. IAPWS release on surface tension of ordinary water substance. 1994.

[161] J. K. Fink and L. Leibowitz. Thermodynamic and transport properties of sodium liquid and vapor. Technical Report ANL/Re-95/2, ANL Reactor Engineering Division, 1995.

[162] I. G. Ritchie. Waterside corrosion of zirconium alloys in nuclear power plants. Technical Report IAEA TECDOC 996, 1998.

[163] F. Garzarolli, W. Jung, H. Shoenfeld, A. M. Garde, G. W. Parray, and P.G. Smerd. Review of PWR fuel rod waterside corrosion behavior. Technical Report EPRI NP-2789 Project 1250 Final Report, 1982.

[164] F. Garzarolli and M. Garzarolli. PWR Zr alloy cladding water side corrosion. Technical Report ANT International, 2012.

[165] P. M. Gilmore, H. H. Klepfer, and J. M. Sorensen. EPRI PWR fuel cladding corrosion (PFCC) model volume 1: Theory and users manual. Technical Report TR-105387-V1, December 1995.

[166] B. Cheng, P. M. Gilmore, and H. H. Klepfer. PWR zircaloy fuel cladding corrosion performance, mechanisms, and modeling. In *Zirconium in the Nuclear Industry: Eleventh International Symposium*, pages 137–160. ASTM STP 1295, American Society for Testing and Materials, 1996, 1996.

[167] J. Ikeda and E. Kolstad. In-pile determination of thermal conductivity of oxide layer on LWR cladding. Technical Report NFIR III RPX-103-04, February, 1996.

[168] G. Schanz. Recommendations and supporting information on the choice of zirconium oxidation models in severe accident codes. Technical Report FZKA 6827, SAM-COLOSS-P043, 2003.

[169] S. Leistikow, G. Schanz, H. v. Berg, and A.E. Aly. Comprehensive presentation of extended Zircaloy-4/steam oxidation results 600-1600 C. In *CSNI/IAEA specialists meeting on water reactor fuel safety and fission product release in off-normal and accident conditions*, Riso Nat. Lab., Denmark, 1983.

[170] J. V. Cathcart, R. E. Pawel, R. A. McKee, R. E. Druschel, G. J. Yurek, J. J. Campbell, and S. H. Jury. Zirconium metal-water oxidation kinetics, IV. reaction rate studies. Technical Report ORNL/NUREG-17, 1977.

[171] J. T. Prater and E. L. Courtright. Zircaloy-4 oxidation at 1300 to 2400 C. Technical Report NUREG/CR-4889, PNL-6166, 1987.

[172] J. C. Griess, H. C. Savage, and J. L. English. Effect of heat flux on the corrosion of aluminum by water, part IV, tests relative to the advanced test reactor and correlation with previous results. Technical Report ORNL-3541, Oak Ridge National Laboratory, 1964.

[173] M. L. Griebenow, G. H. Hanson, M. J. Graber, Jr., and D. S. Field. ATR startup fuel-plate cladding corrosion test: Preliminary data and conclusions. In *American Nuclear Society 1971 Winter Meeting Transactions*, volume 14(3), pages 761–762, 1971.

[174] W. J. Carmack. Temperature and burnup correlated FCCI in U-10Zr metallic fuel. Technical Report INL/EXT-12-25550, Idaho National Laboratory, May 2012.

[175] T. Ogata, M. Akabori, and A. Itoh. Diffusion of cerium in uranium-zirconium solid solutions. *Materials Transactions*, 44(1):47–52, 2003.

[176] T. H. Bauer, G. R. Fenske, and J. M. Kramer. Cladding failure margins for metallic fuel in the integral fast reactor. Technical Report CONF-870812–22, Argonne National Laboratory, July 1987.

[177] Yeon Soo Kim, G L Hofman, S L Hayes, and Y H Sohn. Constituent redistribution in U–Pu–Zr fuel during irradiation. *Journal of Nuclear Materials*, 327(1):27–36, April 2004.

[178] Yeon Soo Kim, S L Hayes, G L Hofman, and A M Yacout. Modeling of constituent redistribution in U–Pu–Zr metallic fuel. *Journal of Nuclear Materials*, 359(1-2):17–28, December 2006.

[179] Masayoshi Ishida, Takanari Ogata, and Motoyasu Kinoshita. Constituent migration model for U-Pu-Zr metallic fast reactor fuel. *Nuclear Technology*, 104:37–51, 1993.

[180] G L Hofman, S L Hayes, and M C Petri. Temperature gradient driven constituent redistribution in U-Zr alloys. *Journal of Nuclear Materials*, 227(3):277–286, January 1996.

[181] R L Williamson, J D Hales, S R Novascone, M R Tonks, D R Gaston, C J Permann, D Andrs, and R C Martineau. Multidimensional multiphysics simulation of nuclear fuel behavior. *Journal of Nuclear Materials*, 423(1-3):149–163, April 2012.

[182] N Carlson. Final Report for Work Package LA0915090116: Fuel Performance Simulations. Technical Report LA-UR-09-07340, 2009.

[183] G L Hofman, L C Walters, and T H Bauer. Metallic fast reactor fuels. *Progress in Nuclear Energy*, 31(1-2):83–110, January 1997.

[184] Shewmon, P. C. The redistribution of a second phase during annealing in a temperature gradient. *Transactions of the Metallurgical Society of AIME*, 212, 1958.